PREDICTION OF A DARRIEUS TURBINE PERFORMANCE CONSIDERING DYNAMIC STALL

BY

MD. MANIRUZZMAN

A THESIS

PRESENTED TO THE

DEPARTMENT OF MECHANICAL ENGINEERING

IN PARTIAL FULFILMENT OF THE REQUIREMENTS

FOR THE DEGREE

OF

MASTER OF SCIENCE IN ENGINEERING (MECH.)

DEPARTMENT OF MECHANICAL ENGINEERING

BANGLADESH UNIVERSITY OF ENGINEERING AND TECHNOLOGY, DHAKA

DECEMBER, 1989

The thesis titled "**Prediction of a Darrieus Turbine Performance considering Dynamic Stall**" submitted by Md. Maniruzzaman, Roll No. 871414P, Registration No. 81368 of M.Sc. Engg. (Mech.) has been accepted as satisfactory in partial fulfilment of the Master of Science in Engineering (Mech.).

BOARD OF EXAMINERS

1. ....

Dr. A. C. Mandal
Professor
Dept. of Mech. Engg.
BUET

Chairman
(Supervisor)

2. ....

Dr. S. M. Nazrul Islam
Professor and Head
Dept. of Mech. Engg.
BUET

Member
(Ex-officio)

3. ....

Dr. Md. Quamrul Islam
Professor
Dept. of Mech. Engg.
BUET

Member

4. ....

Dr. M. Refayet Ullah
Associate Professor
Dept. of Naval Arch. & Marine Engg.
BUET

Member
(External)

ACKNOWLEDGEMENTS

With the sincerity, the author wishes to express his deep gratitude and indebtness to Dr. Amalesh Chandra Mandal, Professor, Department of Mechanical Engineeing , BUET for his valuable supervision, guidance and helpful suggestions in carrying out the research work. Dr. Mandal would always find time to discuss various topics and shed light on any problem and without his supervision, this work would not be completed in time.

The author is highly grateful to Professor S. M. Nazrul Islam, Head of the Department of Mechanical Engineering, BUET, not only for allowing me to use the computer facilities in the department but also for his encouragement in pursuing the Master's degree program.

Sincere thanks to all the colleagues specially to Dr. S. R. Hossain for the inspiration and valuable suggestions in many steps of the work.

The author also thanks Mr. M. A. Salam, draftsman of the Department of Mechanical Engineering, BUET for drafting various figures used in this thesis.

Finally, thanks to Mr. Abdul Jalil, Mr. Fakhrul Islam Hazra and Mr. H. M. Nasrullah for helping me in typing this thesis.

ABSTRACT

A theoretical investigation of the performance characteristics of a straight-bladed Darrieus wind turbine is performed. In this investigation, the phenomena of dynamic stall is introduced into the cascade theory which has been developed recently to predict performance of wind turbines.

The dynamic stall is a complex unsteady flow phenomena. It can produce lift and drag with peak values much higher than those produced due to static stall condition. Boeing-Vertol dynamic stall model is applied to determine aerodynamic lift to encounter the dynamic stalling effect while an empirical relation as a function of lift coefficient is introduced to find the drag. However in the analysis for prestall condition, the modified lift coefficient is used. These are determined approximately from an empirical relation which is obtained from the correlation of the the experimental results presented by N. D. Ham.

A reasonable number of existing overall and local experimental values are compared with the calculated values by the cascade theory including dynamic stall model.It is observed that the consideration of the dynamic stall phenomena improves the prediction of the local values.

CONTENTS

LIST OF FIGURES

LIST OF SYMBOL

A projected frontal area of turbine.

A_{st} strut projected area

AR aspect ratio $= \frac{H}{C}$

b_{st} strut width

C blade chord

c chord of blade within elemental $\delta\theta$

C_d blade drag coefficient

C_{dd} blade drag coefficient due to dynamic stall effect

C_{di} induced drag coefficient

C_{do} zero-lift drag coefficient / section drag coefficient for infinite aspect ratio

C_{doc} zero-lift-drag coefficient corrected for chord-radius ratio

C_{dor} reference zero-lift-drag coefficient

C_D turbine overall drag coefficient $= \frac{F_D}{\frac{1}{2}\rho A V_\infty^2}$

C_{DD} rotor drag coefficient $= \frac{F_D}{\frac{1}{2}\rho A V_a^2}$

C_l blade lift coefficient

C_{l_c} corrected lift coefficient for prestall condition

C_{l_d} blade lift coefficient due to dynamic stall effect

$C_{d,st}$ drag coefficient of strut profile

C_m blade pitching moment coefficient

C_n normal force coefficient

C_p turbine overall power coefficient $= \frac{P_e}{\frac{1}{2}\rho A V_\infty^3}$

$C_{p,st}$ power coefficient due to strut drag force

C_Q turbine overall torque coefficient $= \frac{Q}{\frac{1}{2}\rho A V_\infty^2 R}$

C_t tangential force coefficient

D blade drag coefficient

$\vec{e}_c$ unit vector along chordal direction

F force on blade airfoil

F_D turbine drag in streamwise direction

F_n normal force (in radial direction)

F_{net} net normal force (in radial direction)

F_{nid} force appearing in frictionless flow

F_{nv} force due to pressure loss

F_n^+ non-dimensional normal force $= C_n(\frac{W}{V}_\infty)^2$

F_{st} drag force on the strut

F_t tangential force

F_{ta} average tangential force

F_t^+ non-dimensional tangential force $= C_t(\frac{W}{V}_\infty)^2$

g acceleration due to gravity

H height of the turbine

$\vec{i}\,\vec{j}\,\vec{k}$ unit vectors, each is normal to the plane of the others

K factor to include dynamic stall in drag value

k factor to include real lift value

K_l an empirical constant

k_i exponent in the induced velocity relation

l length of vortex filament

L_{id} lift force appearing in frictionless flow

L_v lift force contributed by pressure loss

L blade lift force

$\dot{m}$ mass flow rate

M blade pitching moment

N number of blades

N_{st} number of strut

P static pressure

P_o overall power

$P_{o,t}$ strut power

P_∞ atmospheric pressure

q dynamic pressure $= \frac{1}{2}\rho W^2$

Q overall torque

Q_{st} strut torque

$\bar{Q}_{st}$ strut average torque

$\vec{r}$ unit vector

rpm turbine speed in revolution per minute

R turbine radius

Re local Reynolds number $= \frac{WC}{\nu}$

Re_r reference Reynolds number

Re_t turbine speed Reynolds number $= \frac{R\omega C}{\nu}$

Re_w wind speed Reynolds number $= \frac{V_\infty C}{\nu}$

$S_{\dot\alpha}$ sign of rate of change of angle of attack

t blade spacing $= \frac{2\pi R}{N}$

t_c maximum blade thickness as a fraction of chord

V local velocity

V_a induced velocity

V_e wake velocity in upstream side

V_n normal velocity component

V_p induced velocity at a point

V_w wake velocity in downstream side

V_Γ velocity contributed by circulation

V_∞ wind velocity

W relative flow velocity

W_{st} relative flow velocity component normal to strut

α angle of attack / angle of attack for finite wing

α_i induced angle of attack

α_l local angle of attack

α_m modified angle of attack for dynamic stall effect

α_{mod} modified angle of attack

α_o angle of attack for infinite wing

β angle between relative flow velocity direction and tangent to blade flight path at blade fixing point

γ an empirical constant

Γ circulation per unit length

Γ_B bound vortex

ΔP_{ov} total pressure loss term (total cascade loss)

ϵ $\frac{D}{L}$

θ azimuth angle

λ tip speed ratio $= \frac{R\omega}{V_\infty}$

ν kinematic viscosity

ρ fluid density

σ solidity $= \frac{NC}{R}$

τ correction factor for induced angle

ϕ_p angle between chordal and freestream velocity direction

ω angular velocity of turbine in rad/sec

SUBSCRIPTS

d downstream side

e trailing edge point

i leading edge point

m maximum value

u upstream side

x x-axis

y y-axis

1 cascade inlet

2 cascade outlet

CHAPTER 1

INTRODUCTION

Wind is a nonpolluting, replenishable source of energy, and though it is intermittent and relatively dilute in nature as compared to fossil fuels and nuclear fuels, it is constituted as a large, practically untapped energy resource. People are extracting energy from wind for the past few centuries. There are many possible ways of extracting useful energy from the wind. Windmill or wind turbine is one of the ways of extracting energy from wind. Recent energy crisis makes this technique of energy extraction more popular. Uptil now many types of wind turbine have been devised. The most common one is the horizontal axis turbine for which the axis of rotation is parallel to the surface of the earth. Another type is vertical axis turbine for which the axis of rotation is perpendicular to both the surface of the earth and the windstream direction.

The present work consists oftheoretical analysis of a vertical axis straight-bladed Darrieus wind turbine including dynamic phenomena. Over the last few years, there have been some advancement in the consideration of the dynamic phenomena which affects the aerodynamic forces originating on the blades of vertical axis turbine. However, none of the prediction methods consisting of existing dynamic stalling models can provide reasonable performance prediction especially for the local values which are important for the design of the wind turbine.

1.1 Resurrection of Wind Power as a Source of Energy.

There is an urgent need to find an alternative source of energy which must be nonpolluting and competitive, because of the higher price of energy derived from the conventional sources and systems. Also the extended public awareness of the potential impact of conventional energy systems on the environment have created an intensified demand for viable alternative energy sources. The use of wind power is one such alternative.

Preliminary studies have shown that the environmental impact of wind energy system is relatively small compared to conventional power system. Wind powered systems do not require the flooding of large land areas or the alteration of natural ecology, as hydroelectric systems do. Furthermore, they produce no waste-products or thermal or chemical effluents as fossil- fueled or nuclear-fueled systems do.

Power extracted from the wind is initially obtained in the form of rotary, translational or oscillatory mechanical motion. This mechanical motion can be used to pump fluids or can be converted to electricity, heat or other useful form of energy. In any case, wind energy is one of the most flexible and tractable of all available energy sources, since the mechanical energy derived directly from the wind can be readily and efficiently converted to other forms of energy. The efficiency of converting wind-driven mechanical energy to heat or electrical energy is much higher, for instance, than the efficiency of converting solar or fuel-derived heat energy to mechanical or electrical energy. Since the efficiencies that can be attained when converting heat to mechanical or electrical energy is limited by the relatively low Carnot cycle efficiencies, which, even under optimum conditions, usually do not exceed 30 to 35 %.

1.2 Aim of the Thesis.

Dynamic stall differs substantially from the familiar static stall encountered at constant or slowly varying angle of attack. The primary characteristics of dynamic stall are its occurence at an angle of attack greater than the stall angle. Uptil now, several experimental works have been done in this field, especially for helicopter applications [10], [20]. These studies showed that the loads of an airfoil oscillating harmonically in pitch are different from those of non-pitching airfoil at the same angle of attack. Load variations due to dynamic stall may exceed the fatigue life of the wind turbine. Hence to predict the performance of Darrieus wind turbine, dynamic stall should be encountered especially in the range of low and moderate tip speed ratios.

Currently existing aerodynamic models to determine the performance characteristics of Darrieus turbine can be divided into three categories : based on momentum theory, based on vortex model and on cascade principle. The momentum models, single, multiple and double-multiple streamtube may predict overall value of performance characteristics reasonably upto moderate and low tip speed ratios and at low solidities. At the higher tip speed ratio the momentum model exceeds the theoretical limit of induced velocity ratio. The vortex model may provide prediction for both induced velocity and instantaneous aerodynamic loads on the blades at higher tip speed ratios and for larger rotor solidities; in some cases, although they require a considerable amount of computer time and often create convergence problem. Cascade theory, which is comparatively new, give more or less realistic picture of the induced velocity at all tip speed ratios and solidities. However, in the prediction of local forces there appear some differences. For this reason dynamic stall effect is incorporated into the cascade model with a view to perform investigation in this concern.

Uptil now, several semiempirical methods have been developed for the dynamic stall to determine the basic aerodynamic characteristics. These methods are : Boeing-Vertol, United Aircraft Research Laboratory (UARL), Massachusetts Institute of Technology (MIT), SWECS dynamic theory, Lockheed and Sikorsky (time-delay method) [21],[27]. Among them, Boeing-Vertol method was selected as the basic dynamic stall model, because of its simplicity, ease of application and less computational time requirement.

1.3 Scope of the Thesis.

This thesis provides with an elaborate analysis regarding the theoretical investigation of the aerodynamic performance considering dynamic stall phenomena for the vertical axis straight-bladed Darrieus wind turbine. In the analysis, symmetrical blade sections are taken into account.

Chapter 1 provides Introduction regarding the concept of existing works concernig dynamic phenomena in brief. Chapter 2 gives the brief description of the historical background of the wind turbines.

The existing theories with short mathematical models are described in the chapter 3. The different prediction methods for the vertical-axis Darrieus wind turbines are analyzed.

The theory related to the present work is rather described elaborately in chapter 4. Expressions of lift-drag characteristics including dynamic stall are introduced in this chapter.

Chapter 5 presents the calculated results. The effects of various important parameters on the performance characteristics of Darrieus wind turbines are discussed. Comparisons of calculated and experimental results of straight-bladed Darrieus wind turbine are also given in this chapter.

Finally, in the chapter 6, general conclusions are drawn and few recommendations for the future works are made.

CHAPTER 2

HISTORICAL BACKGROUND

Only during the last decade a considerable number of research have been done on the performance prediction of Darrieus wind turbine. In this regard a number of analytical prediction methods have been developed. A brief description of some of them is given in this chapter. A brief history of development of wind turbine has also been provided in short.

2.1 Historical Background.

Among the sources of energy which man exploited to his advantage were the energy from wind and water. Two early uses of wind energy were the windmills and the sailships. The use of windmills date back to 17th century B.C. when the Babylonian emperor Hammurabi planned to use windmills to pump brine water. The duration from the ancient time upto the end of the 19th century may be categorized as the ancient development period while that from the end of 19th century upto date may be termed as the modern development period.

Historically, wind energy conversion systems can be considered as one of man's truly basic machines. Early documents refer to use of windmills, as depicted in Figure 2.1, in Persia in the middle of 7th century called Persian vertical-axis windmills which was used to grind grain. That kind of windmill had been working upto about 12th century, when simultaneously in France and England Dutch type of windmills were made whose purpose were to grind grain and pump water. These windmills were of horizontal-axis type. Sketches of a six sail windmill has also been found among the many sketches by Leonardo the Vinci (1452-1519). The first propeller type blade were used during this period. The earliest record of English windmills dates back 1191 which were two type-"Post-mill" and the "Towermill".

In the fourteenth century, the Dutch had given the lead in improving the design of windmills. These windmills were used extensively for draining the marshes and lakes of Rhine river delta.

Although modern development have begun with the development of horizontal-axis wind turbine, two quite different vertical axis type designs were developed during early part of the twentieth century. One of the designs known as the Savonius rotor which is constructed by Finnish Engineer S.J. Savonius in 1924 and he conceived the idea from the Flettner's rotor. The rotor was formed by a cylinder into two semicylindrical surfaces, moving these surfaces sideways along the cutting plane to form a rotor with cross-section in the form of the letter "S", placing a shaft in the centre of rotor and closing the end surfaces with circular end plates as shown in Figure 2.2, The other vertical windmill design patented in 1925 by George J.M. Darrieus of France consisted of two thin airfoils with one end mounted in the lower end of a vertical shaft and the other end mounted on the upper end of the same shaft, sketched in Figure 2.3. This kind of wind machine is called Darrieus wind turbine after the name of G.J.M. Darrieus. Another interesting wind machine that was built during that period was the Smith Putnam unit as shown in Figure 2.4. After a lengthy study in the 1930's Palmen Putnam had concluded that large machine was required to minimize the cost of electricity generated by the wind.

In Denmark, at the end of nineteenth century there were about 2500 industrial windmills in operation supplying a total of about 40,000 hp or 30 KW i.e. about 25% of the total power available to Danish industry at that time. The 200 KW Gedser mill, shown in Figure 2.5 was operated until 1908, after then it was shutdown because , by that time the cost of electricity generated by this wind-powered unit was about twice the equivalent cost of electricity generated by steam-powered unit, that were being operated in Denmark , After the energy crises of 1973, the 200 KW windmill was refurbished , and in 1977, it was put back into service, using funding partly supplied by the United states Department of Energy.

In 1931, the Russians built an advanced 100 KW wind turbine near Yalta on the Black Sea. The annual output of this machine was found to be about 280000 KWh per year. At one time in 1930's the Russians considered for building a larger system of 5 MW rated capacity but apparently this project was never implemented.

In England in the later 1940's and during 1950's a considerable amount of works was done on wind operated electricity generation unit. In the 1950's the Enfield cable Company built a wind powered generator designed by a French named Andreau as shown in Figure 2.7. In this design, the propeller blades were hollow and air enters the tower through some ports in the lower part of the tower, passed through an air turbine which turned the electric generator. The air went up through the rotor and went out the hollow tips of the blades, as it rotated.

The efficiency of this unit was found to be low compared with other more conventional wind power rotor. The main advantage of this system is that the power generating equipment is not supported aloft.

From 1958 to 1966, the French built and operated several large wind powered electric generators. These included three horizontal axis units each with three propeller type blades. A unit of this kind was operated intermittently near Paris from 1958 to 1963, (Figure 2.8) This unit was designed to generate 800 KW in winds having speed of 37 mph.

The Germans made a number of improvements in the design of wind powered generators including light weight constant speed rotors that were controlled by variable pitch propeller blades with swept diameter as large as 110 feet. The largest unit generated 100 KW. These units operated successfully for more than 4000 hours during the period from 1957 to 1958.

At the mid-nineteenth century, in the United States of America, more than six-million small multibladed windmill have been constructed and operated. These windmills having power output of less than 1 hp each in an average wind speed, used to pump water, generate electricity and perform similar functions. It is estimated that over 150,000 turbine are currently is in operation.

In U.S.A. water pumping windmills are used not only for pumping water for farm and rural households, but for watering livestock on ranges in remote areas. These type of machines commonly have metal fan-blades, 12 to 16 feet in diameter, mounted on a horizontal shaft, with a tailvane to keep rotor facing to the wind as shown in Figure 2.9. A 12-feet diameter rotor of this type develops about 2/3 hp in a 15 mph wind and can pump about 10 gallons of water per minute to a height of about 100 feet.

Small wind machine, used to generate electricity, usually have two or three propeller-type blades that are connected by a shaft and gear train to a d.c generator, they usually incorporate some type of energy storage system, often consisting of a bank of batteries. One of the classic designs of this type is the Jacobs Wind Electric Company unit with a three-blades propeller, 14 feet is swept diameter, which deliver about 1 KW in a wind of 14 mph.

CHAPTER 3

LITERATURE SURVEY

The wind turbine extracts energy from the air flow and converts it into mechanical energy which later may be converted into other convenient forms of energy such as electrical energy, energy for pumping water etc. The performance analysis of the turbine mostly based on steady flow and effect of turbulence on boundary layer is neglected.

Existing theories on performance prediction of Darrieus wind turbine can be categorized into three main groups: those based on momentum theory, those based on vortex model and those on cascade model. Later, these models are modified by incorporating various effects, such as flow-curvature effect, aspect ratio effect (for a straight-bladed wind turbine only), dynamic stall effect etc.

3.1 Single Streamtube Theory.

Single Stream tube theory is the most simple prediction model for the calculation of performance characteristics of a straight-bladed Darrieus wind turbine. In 1974, Dr. Templin [40] first proposed this theory for Darrieus turbine. In this model the whole turbine is assumed to be enclosed within a single stream tube. This theory mainly based on the concept of windmill actuator disc theory.

In the actuator disc theory, the induced velocity (rotor axial flow velocity) is assumed to be constant throughout the disc and is obtained by equating the streamwise drag with the rate of change in axial momentum. In the assumption of Dr. Templin, the actuator disc is considered as the surface of the imaginary body of revolution. It is assumed that the flow velocity is constant althrough the upstream and the downstream faces of the swept volume. This theory presented by Templin, is the first approach to permit numerical design calculations for a vertical-axis wind turbine.

The necessary assumptions needed for this theory are:

1. The forces on the rotor blade are computed on the basis of uniform velocity of the air on the rotor.
2. Axial velocity of the air has a constant value over althrough the rotor.

3.1.1 Drag Force Along Streamtube.

The momentum equation for the rotor has been taken to be

$$F_D = \dot{m}\,(V_\infty - V_w) \tag{3.1.1}$$

on the basis that the right handside of this equation represents the total increase of momentum and that this resultant pressure force on the whole fluid is zero. Here F_D is the streamwise drag force, V_∞ and V_w are respectively the freestream velocity and the wake velocity and $\dot{m}$ is the mass flow rate.

According to Glauert's Actuator Disc theory, the uniform flow velocity through the rotor can be expressed as,

$$V_a = \frac{V_\infty + V_w}{2} \tag{3.1.2}$$

Introducing $\dot{m} = A\rho V_a$ in equation (3.1.1)

$$F_D = A\,\rho\,V_a\,(V_\infty - V_w) \tag{3.1.3}$$

where A is the turbine projected area and ρ is the fluid density. From equations (3.1.2) and (3.1.3), the force F_D can be expressed as,

$$F_D = 2\,A\,\rho\,V_a\,(V_\infty - V_a) \tag{3.1.4}$$

Rotor drag coefficient is defined as,

$$C_{DD} = \frac{F_D}{\frac{1}{2}\,\rho A V_a^2} \tag{3.1.5}$$

From the equations (3.1.4) and (3.1.5), C_{DD} can be expressed as,

$$C_{DD} = 4\,\frac{(V_\infty - V_a)}{V_a} \tag{3.1.6}$$

As indicating in the Figure 3.2, the elemental drag force along the freestream velocity direction based on the aerodynamic forces on the elemental blade aerofoil is found as,

$$\delta F_D = \delta F_n\,Sin\theta\,Cos\phi - \delta F_t\,Cos\theta \tag{3.1.7}$$

where θ is the azimuth angle, ϕ is the angle of the blade with the normal of the equatorial plane, δF_n and δF_t are respectively the elemental blade forces.

3.1.2 Blade Elemental Angles and Velocities.

Air velocities relative to an airfoil element is illustrated in Figure 3.3. Considering the blade is moving with ω rad/sec in still air, the air velocity relative to the blade will be $R\omega$ and will act in the opposite direction, where R is the radius of the turbine. If V_a is the induced velocity and $R\omega$ be the tangential velocity, then the velocity in chordal direction can be written as,

$$V_c = R\omega + V_a Cos\theta \tag{3.1.8}$$

and the velocity in the normal direction to the blade flight path as,

$$V_n = V_a Sin\theta \tag{3.1.9}$$

Now the resultant flow velocity, W, relative to the airfoil becomes,

$$W^2 = V_c^2 + V_n^2 \tag{3.1.10}$$

Putting the values of V_c and V_n from equations (3.1.8) and (3.1.9) one obtains,

$$W^2 = (R\omega + V_a Cos\theta)^2 + (V_a Sin\theta)^2 \tag{3.1.11}$$

Equation (3.1.11) can be written as,

$$\frac{W}{V_a} = \sqrt{[\frac{\frac{R\omega}{V_\infty}}{\frac{V_a}{V_\infty}} + Cos\theta]^2 + Sin^2\theta} \tag{3.1.12}$$

where the term $\frac{R\omega}{V_\infty}$ is the tip speed ratio λ . The angle of attack as shown in Figure 3.3 can be obtained as,

$$tan\alpha = \frac{V_n}{V_c} = \frac{V_a Sin\theta}{R\omega + V_a Cos\theta} = \frac{sin\theta}{\frac{R\omega}{V_\infty} / \frac{V_a}{V_\infty} + Cos\theta} \tag{3.1.13}$$

Hence local angle of attack, α, can be written as,

$$\alpha = tan^{-1}[\frac{sin\theta}{\frac{R\omega}{V_\infty} / \frac{V_a}{V_\infty} + Cos\theta}] \tag{3.1.14}$$

3.1.3 Aerodynamic Forces.

Figure 3.4 illustrates the blade airfoil cross-section with the aerodynamic forces acting on it. The elemental tangential force δFt and the normal force δFn are respectively parallel and perpendicular to the airfoil chord line. The elemental tangential and normal forces are defined as,

$$\delta F_t = \frac{1}{2} C_t \, \rho \, W^2 c \, H \tag{3.1.15}$$

$$\delta F_n = \frac{1}{2} C_n \, \rho \, W^2 c \, H \tag{3.1.16}$$

where C_t and C_n are respectively the tangential and normal force coefficients while c is the blade chord which occurs within the elemental angle $\delta\theta$. H is the height of the turbine. The two dimensional lift and drag forces can be related to δF_t and δF_n using the following equations. Referring to the Figure 3.4

$$\delta F_t = \delta L \, Sin\theta - \delta D \, Cos\theta \tag{3.1.17}$$

$$\delta F_n = \delta L \, Cos\theta + \delta D \, Sin\theta \tag{3.1.18}$$

where elemental lift force δL and the elemental drag force δD can be defined as,

$$\delta L = \frac{1}{2} C_l \, \rho \, W^2 c \, H \tag{3.1.19}$$

$$\delta D = \frac{1}{2} C_d \, \rho \, W^2 c \, H \tag{3.1.20}$$

where C_l and C_d are respectively the lift and drag coefficients. Now from equations

(3.1.15) to (3.1.20) one may obtain,

$$C_n = C_l \, Cos\theta + C_d \, Sin\theta \tag{3.1.21}$$

$$C_t = C_l \, Sin\theta + C_d \, Cos\theta \tag{3.1.22}$$

3.1.4 Velocity Ratio and Power Coefficient.

Putting the values of δF_t (3.1.15) and δF_n (3.1.16) in equation(3.1.7), the elemental streamwise drag force can be written as,

$$\delta F_D = \frac{1}{2} \rho c W^2 (C_n Sin\theta - C_t Cos\theta) H \tag{3.1.23}$$

To introduce the assumption of infinite number of blades distribution, replacing c by $NC\delta\theta/2\pi$, N being the number of blades, dynamic pressure $q = \frac{1}{2}\rho W^2$, one may obtain overall drag force in integration form from equation (3.1.23) as follows.

$$F_D = \frac{NCH}{2\pi} \int_0^{2\pi} q (C_n Sin\theta - C_t Cos\theta) \, d\theta \tag{3.1.24}$$

Now from the equation (3.1.5) and (3.1.24), the drag coefficient C_{DD} may be written as,

$$C_{DD} = \frac{NC}{4\pi R} \int_0^{2\pi} \left(\frac{W}{V_a}\right)^2 (C_n Sin\theta - C_t Cos\theta) \, d\theta \tag{3.1.25}$$

From the equation (3.1.6), the velocity ratio $\frac{R\omega}{V_\infty}$ based on the ambient wind speed may be expressed as,

$$\frac{R\omega}{V_\infty} = \frac{R\omega}{V_a} \left(\frac{1}{1 + C_{DD}/4}\right) \tag{3.1.26}$$

Now the rotor drag C_{DD} can be calculated from equation (3.1.25) for a given turbine geometry, rotational speed ω and specified rotor velocity ratio $\frac{R\omega}{V_a}$. The velocity ratio $\frac{R\omega}{V_a}$ based on the ambient wind speed can be obtained from the equation

(3.1.26). Thus this method requires no iterative process. The elemental torque can be written as,

$$\delta Q = \delta F_t R \tag{3.1.27}$$

Substituting equation (3.1.15) and replacing c by $NC\delta\theta/2\pi$ for an assumption of infinite number of blades distribution, one obtains the expression of overall torque, Q, in the integration form,

$$Q = \frac{NC}{2\pi}.RH \int_0^{2\pi} C_t\, q\, d\theta \tag{3.1.28}$$

The overall power P_o is,

$$P_o = Q\omega = \frac{NC\omega}{2\pi}.RH. \int_0^{2\pi} C_t\, q\, d\theta \tag{3.1.29}$$

According to Glauert, the expression for the maximum power (ideal power) is,

$$P_{max} = \frac{16}{27} \cdot \frac{1}{2} V_\infty^3 A \tag{3.1.30}$$

Templin defines the power coefficient as,

$$C_p = \frac{P_o}{P_{max}} \tag{3.1.31}$$

3.1.5 Modification of Single Streamtube Theory.

Single streamtube model affords a great deal of simplicity and can predict the overall performance of a lightly loaded wind turbine but according to the investigation, it always predicts higher power than the experimental results. This model can not predict accurately the wind velocity variations along the rotor. This variations gradually increases with the increase of blade solidity and the tip speed ratio.

R.B. Noll and N.D. Ham [28] have presented a analytical model based on single streamtube theory for the performance prediction of a vertical-axis straight-bladed Darrieus turbine which are cyclically pitched. They added the effect of strut drag, turbulent wake state and dynamic stall to their analytical model.

3.2 Multiple Streamtube Theory.

Multiple streamtube theory proposed by Wilson and Lissaman[44] is the improved prediction methods for the calculation of performance characteristics of a Darrieus turbine. In this theory, the swept volume of the turbine is divided into a series of streamtube. These adjacent tubes are aerodynamically independent. This theory gives rise to a velocity distribution through the rotor in horizontal direction.

3.2.1 Basic Assumptions.

The necessary assumption needed for multiple streamtube theory are,

1. To determine the induced velocity, the flow is assumed to be inviscid and incompressible. As a result the only force acts on the blade element is the lift force and its component along the streamtube is equated to the force contributed by the rate of change of momentum along the streamtube.

2. The blades are infinite in number causing the swept surface to be continuous at all times but in such a way that the solidity remains finite.

3. Each streamtube is considered to be independent with no interference of adjacent tubes, so that momentum theory is applied to each of the tube separately.

4. The streamtubes are considered to be parallel with each other, so that induced velocity remains constant along each of the streamtube.

5. The flow is assumed to be steady, one dimensional frictionless and incompressible.

3.2.2 Axial Momentum Theory.

The streamwise forces along the streamtube are calculated using the axial momentum theory. Figure 3.5 shows an elemental streamtube for a straight-bladed Darrieus turbine. The cross-sectional area δA of the elemental streamtube can be obtained as,

$$\delta A = H\, R\, Sin\theta\, \delta\theta \tag{3.2.1}$$

The flow around the airfoil blade element is retarded in two stages. Once before and once after its passage through the blade elements on the either side of the streamtube (Figure 3.6).The elemental force along the streamtube is given by,

$$\delta F_D = \delta \dot{m}\,(V_\infty - V_w) \tag{3.2.2}$$

where $\delta \dot{m}$ is the mass flow rate through the streamtube. Replacing $\delta \dot{m}$ by $\rho V_a \delta A$, the elemental drag force becomes,

$$\delta F_D = \rho\, V_a (V_\infty - V_w)\, \delta A \tag{3.2.3}$$

Applying Bernoulli's equation in the upstream and the downstream side respectively one obtains,

$$P_\infty + \frac{1}{2}\rho V_\infty^2 = P_u + \frac{1}{2}\rho V_a^2 \tag{3.2.4}$$

$$P_\infty + \frac{1}{2}\rho V_w^2 = P_d + \frac{1}{2}\rho V_a^2 \tag{3.2.5}$$

where P_u and P_d are respectively the static pressure at the upstream end of a streamtube as it enters the swept volume and that at the downstream end of a stream tube as it leaves the swept volume. P_∞ is the atmospheric pressure. Now subtracting the above two equations,

$$P_u - P_d = \frac{1}{2}(V_\infty^2 - V_w^2) \tag{3.2.6}$$

The elemental drag force along the stream tube is

$$\delta F_d = (P_u - P_d)\,\delta A \tag{3.2.7}$$

Substituting the equation (3.2.6) into the equation (3.2.7), one may obtain,

$$\delta F_d = \frac{1}{2}(V_\infty^2 - V_w^2)\,\delta A \tag{3.2.8}$$

Now from equation (3.2.3) and (3.2.8)

$$\rho V_a(V_\infty - V_w)\,\delta A = \frac{1}{2}\rho(V_\infty^2 - V_w^2)\,\delta A \tag{3.2.9}$$

The above equation finally becomes,

$$V_w = 2V_a - V_\infty \tag{3.2.10}$$

According to the assumptions of the theory, the induced flow velocity can not be greater than half of the freestream velocity. Otherwise, the wake velocity will either be zero or negative. In the real flow field this does not appear. The wake region is turbulent, as a result there occurs mixing of the wake with the high energy fluid layers outside the wake region.

From the equations (3.2.3) and (3.2.10), the elemental drag force becomes,

$$\delta F_D = 2\rho V_a(V_\infty - V_a)\,\delta A \tag{3.2.11}$$

Introducing the value of δA and a non-dimensional parameter $h = H/R$, the above equation becomes,

$$\delta F_D = 2R^2 \rho\, Sin\theta\, V_a(V_\infty - V_a) h\, \delta\theta \tag{3.2.12}$$

3.2.3 Blade Element Force Along Streamtube.

Wilson and Lissaman [42] consider a theoretical lift coefficient in their calculation, which is given by,

$$C_l = 2\pi\, Sin\alpha \tag{3.2.13}$$

To take into account the real lift coefficient, it may be expressed as,

$$C_l = 2\,\pi\, k\, Sin\alpha \tag{3.2.14}$$

The value of C_l is taken from the airfoil data corresponding to the local angle of attack while the value of the factor k is found by an iterative process.

For an inviscid and incompressible fluid, the elemental lift force, from the Kutta-Joukowski relations is given by,

$$\delta L = \rho W H\, \delta\Gamma \tag{3.2.15}$$

where $\delta\Gamma$ is the elemental circulation for unit length of the blade and W is the relative flow velocity. The elemental lift force, according to the equation (3.1.19) is,

$$\delta L = \frac{1}{2} C_l\, \rho\, c\, W^2\, H \tag{3.2.16}$$

From the equations (3.2.15) and (3.2.16) the expression of the elemental circulation is found as,

$$\delta\Gamma = \frac{1}{2}\, c\, C_l\, W \tag{3.2.17}$$

Introducing the equation (3.2.14) for the lift coefficient C_l one obtains,

$$\delta\Gamma = \pi\, k\, c\, W\, Sin\alpha \tag{3.2.18}$$

The above equation can be expressed in vector form as,

$$\delta\vec{\Gamma} = \pi K c\, W\, Sin\alpha\, \vec{e}_\Gamma \tag{3.2.19}$$

where $\vec{e}_\Gamma$ is the unit vector in the direction of $\delta\Gamma$

The above equation may also be written as,

$$\delta\vec{\Gamma} = \pi K c\, \vec{W} \times \vec{e}_c \tag{3.2.20}$$

where $\vec{e}_c$ is the unit vector in the chordal direction, For an inviscid and incompressible fluid the elemental force on the blade element can be expressed in vector form as,

$$\delta\vec{F} = \rho H\, \vec{W} \times \delta\vec{\Gamma} \tag{3.2.21}$$

Now referring to the Figure 3.7, the expression of the relative flow velocity W and unit vector $\vec{e}_c$ becomes,

$$\vec{W} = V_n\,\vec{i} + V_c\,\vec{j} = V_a\, Sin\theta\,\vec{i} + (R\omega + V_a\, Cos\theta)\,\vec{j} \tag{3.2.22}$$

and

$$\vec{e}_c = \vec{j} \tag{3.2.23}$$

where the unit vectors $\vec{i}$ and $\vec{j}$ are considered respectively along the normal direction to the blade chord and the tangential velocity direction. The values of V_c and V_n are taken from the equations (3.1.8) and (3.1.9) respectively. Inserting the values of $\vec{W}$ and $\vec{e}_c$ in the equation (3.2.20) one obtains,

$$\delta\vec{\Gamma} = \pi k c\left[V_a\, Sin\theta\,\vec{i} + (R\omega + V_a\, Cos\theta)\,\vec{j}\right] \times \vec{j} \tag{3.2.24}$$

Considering the unit vector $\vec{k}$ perpendicular to the plane of the unit vectors $\vec{i},\vec{k}$; since $\vec{i} \times \vec{j} = \vec{k}$ and $\vec{j} \times \vec{j}=0$, the above equation becomes

$$\delta\vec{\Gamma} = \pi kc\, V_a\, Sin\theta\, \vec{k} \tag{3.2.25}$$

Introducing the values of $\vec{W}$ (3.2.14) and $\delta\vec{\Gamma}$ (3.2.25) in the equation (3.2.21) one may obtain,

$$\delta\vec{F} = \pi kc \left[V_a Sin\theta\, \vec{i} + (R\omega + V_a Cos\theta)\, \vec{j}\right] H \times (V_a Sin\theta\, \vec{k}) \tag{3.2.26}$$

After vector multiplication, the elemental force $\delta\vec{F}$ becomes

$$\delta\vec{F} = \rho\pi kcH \left[(R\omega V_a Sin\theta + V_a^2 Sin\theta\, Cos\theta)\, \vec{i} - V_a^2 Sin^2\theta\, \vec{j}\right] \tag{3.2.27}$$

The equation (3.2.27) can be write in the following form,

$$\delta\vec{F} = \rho\pi kcH(F_1\, \vec{i} + F_2\, \vec{j}) \tag{3.2.28}$$

where $F_1 = R\omega V_a Sin\theta + V_a^2 Sin\theta\, Cos\theta$ and $F_2 = -V_a^2 Sin^2\theta$

Now referring to the Figure 3.8, the elemental force component on the blade element along the streamtube is,

$$\delta F_D = \rho\pi kcH(F_1 Sin\theta + F_2 Cos\theta) \tag{3.2.29}$$

Equation (3.2.29) may be obtain in the following form after introducing the values of F_1 and F_2 ,

$$\delta F_D = \rho\pi kc\, R\omega H V_a Sin^2_\theta \tag{3.2.30}$$

Now introducing a non-dimensional parameter $h = \frac{H}{R}$ and replacing c by $\dfrac{NC\delta\theta}{2\pi}$ for an assumption of infinite number of blades distribution, δF_D may be expressed as,

$$\delta F_D = \frac{1}{2} kNCR^2 h\omega V_a Sin^2\theta\, \delta\theta \tag{3.2.31}$$

Now multiplying the equation (3.2.31) by 2 for two blade elements in one streamtube, one finds,

$$\delta F_D = \rho kNCR^2 h\omega V_a Sin^2\theta\, \delta\theta \tag{3.2.32}$$

3.2.4 Induced Velocity Ratio, Aerodynamic Forces and Power Coefficient.

To find the induced velocity ratio, the relative flow velocity W, the local angle of attack α and the local Reynolds number Re are necessary. The relative flow velocity W and angle of attack α may be obtained from the equations (3.1.11) and (3.1.13), which are given below,

$$\frac{W}{V_a} = \sqrt{\left[\left(\frac{R\omega}{V_\infty} / \frac{V_a}{V_\infty}\right) + Cos\theta\right]^2 + Sin^2\theta} \tag{3.2.33}$$

$$\alpha = tan^{-1}\left[\frac{Sin\theta}{\frac{R\omega}{V_\infty} / \frac{V_a}{V_\infty} + Cos\theta}\right] \tag{3.2.34}$$

The local Reynolds number Re for the constant wind speed condition is expressed in the form,

$$Re = \frac{WC}{\nu} = \frac{W}{V_a} \cdot \frac{V_a}{V_\infty} \cdot \frac{V_\infty C}{\nu} = \frac{W}{V_a} \cdot \frac{V_a}{V_\infty} . Re_w \tag{3.2.35}$$

and that for the constant turbine speed condition is expressed in the form,

$$Re = \frac{WC}{\nu} = \frac{W}{V_a} \cdot \frac{V_a}{V_\infty} \cdot \left(\frac{R\omega C}{\nu}\right) / \left(\frac{R\omega}{V_\infty}\right) = \frac{W}{V_a} \cdot \frac{V_a}{V_\infty} \cdot \frac{Re_t}{\lambda} \tag{3.2.36}$$

where $Re_w(= V_\infty C/\nu)$ is the wind speed Reynolds number and $Re_t(= R\omega C/\nu)$ is the turbine speed Reynolds number.

Now from the equations (3.2.12) and (3.2.32), one may obtain the expression of the induced velocity ratio (rotor axial flow velocity) as,

$$\frac{V_a}{V_\infty} = 1 - \frac{k}{2}.\frac{NC}{R}.\frac{R\omega}{V_\infty}.Sin\theta \tag{3.2.37}$$

The value of the induced velocity ratio is obtained by an iterative process. For known values of tip speed ratio $\lambda\,(= R\omega/V_\infty)$, solidity ratio $\delta\,(= NC/R)$, azimuth angle θ, the starting value of the induced velocity ratio is chosen as 1.0 or as that calculated for the prior streamtube. Now the relative flow velocity W and the local angle of attack α are respectively calculated from equation (3.1.11) and (3.1.13). Then the local Reynolds number Re is calculated either from the equation (3.2.35) for constant wind speed condition or from the equation (3.2.36) for constant turbine speed condition. With the known values of Re and α, the value of the lift coefficient is taken from the airfoil data and the factor k is calculated from the equation (3.2.14). Now the new value of the induced velocity ratio is calculated by using the equation (3.2.37). This process is continued until the induced velocity ratio is obtained with the desired accuracy.

The elemental blade pitching moment is defined by,

$$\delta M = \frac{1}{2}C_m \rho W^2 cHC \tag{3.2.38}$$

The non-dimensional normal force F_n^+ and the non-dimensional tangential force F_t^+ are defined in the following way,

$$F_n^+ = \frac{\delta F_n}{\frac{1}{2}\rho c H V_\infty^2} \tag{3.2.39}$$

$$F_t^+ = \frac{\delta F_t}{\frac{1}{2}\rho c H V_\infty^2} \tag{3.2.40}$$

Introducing the values of δF_n (3.1.14) and δF_t (3.1.15) in the above equations (3.2.39) and (3.2.40) respectively, one obtains,

$$F_n^+ = C_n \frac{W^2}{V_\infty^2} \tag{3.2.41}$$

$$F_t^+ = C_t \frac{W^2}{V_\infty^2} \tag{3.2.42}$$

Referring to the Figure 3.9, the elemental streamwise drag force is,

$$\delta F_D = 2(\delta F_n Sin\theta - \delta F_t Cos\theta) \tag{3.2.43}$$

Introducing the value of δF_n (3.1.14) and δF_t (3.1.15) respectively in the above equation (3.2.43), one finds,

$$\delta F_D = \rho C W^2 (C_n Sin\theta - C_t Cos\theta) H \tag{3.2.44}$$

Replacing c by $NC\delta\theta/2\pi$ for an assumption of infinite number of blades distribution and introducing a non-dimensional parameter $h = H/R$, the above equation (3.2.44) can be written as,

$$\delta F_D = \frac{NC}{2\pi R} . \rho W^2 R^2 \left(C_n Sin\theta - C_t Cos\theta\right) h \delta\theta \tag{3.2.45}$$

Coefficient of overall elemental turbine drag (streamwise force) is defined as,

$$\delta C_D = \frac{\delta F_D}{\frac{1}{2}\rho A V_\infty^2} \tag{3.2.46}$$

where $A(= 2RH)$ being the projected frontal area of the swept volume. Now the expression of the turbine overall elemental drag coefficient can be obtained as,

$$\delta C_D = \frac{NC}{\pi R} . \frac{R^2}{A} . h . \left(\frac{W}{V_\infty}\right)^2 \left(C_n Sin\theta - C_t Cos\theta\right) \delta\theta \tag{3.2.47}$$

Integrating the equation (3.2.47), the turbine overall drag coefficient can be obtained as,

$$C_D = \frac{NC}{2\pi R}\int_0^{\pi} \frac{W^2}{V_\infty}\left(C_n Sin\theta - C_t Cos\theta\right) d\theta \qquad (3.2.48)$$

The blade elemental torque of the turbine is found as,

$$\delta Q = \delta F_t R + \delta M \qquad (3.2.49)$$

From the equations (3.1.15) (3.2.38) and (3.2.49) one obtains,

$$\delta Q = \frac{1}{2}\rho c W^2 (RC_t + CC_m)H \qquad (3.2.50)$$

Inserting the non-dimensional parameter is $h = H/R$ and replacing c by $NC\delta\theta/2\pi$ for an assumption of infinite number of blades distribution, δQ may be expressed as,

$$\delta Q = \frac{NC}{4\pi R}\rho R^3 W^2 \left(C_t + \frac{C}{R}C_m\right) h\delta\theta \qquad (3.2.51)$$

The overall elemental torque coefficient is defined as,

$$\delta C_Q = \frac{\delta Q}{\frac{1}{2}\rho A V_\infty^2 R} \qquad (3.2.52)$$

From the equation (3.2.51) and (3.2.52), the expression of δC_Q is obtained as,

$$\delta C_Q = \frac{NC}{2\pi R}.\frac{R^2}{A}.\frac{W^2}{V_a}\left(C_t + \frac{C}{R}C_m\right)\frac{V_a^2}{V_\infty^2}.h\delta\theta \qquad (3.2.53)$$

After integration, the turbine overall torque coefficient is expressed as,

$$C_Q = \frac{NC}{4\pi R}\int_0^{2\pi} \frac{W^2}{V_\infty}\left(C_t + \frac{C}{R}C_m\right)\frac{V_a^2}{V_\infty^2} d\theta \qquad (3.2.54)$$

The overall power coefficient C_p (may also be called as the aerodynamic efficiency) is defined as the ratio of the power P_o produced by the turbine to the total power available in the air passing through the same swept volume of the turbine and is given by,

$$C_p = \frac{P_o}{\frac{1}{2}\rho a V_\infty^3} \tag{3.2.55}$$

Introducing the value of overall power $P_o = Q\omega$, one obtains,

$$C_p = \frac{Q\omega}{\frac{1}{2}\rho A V_\infty^3} = \frac{Q}{\frac{1}{2}\rho A V_\infty^2 R}.\frac{R\omega}{V_\infty} = C_Q.\lambda \tag{3.2.56}$$

Inserting the value of C_Q from the equation (3.2.54), the overall power coefficient C_p may be found at any particular tip speed ratio λ . The power coefficient is calculated by the numerical integration method applying Simpson's rule.

3.2.5 Modifications of Multiple Streamtube theory.

Wilson et al considered the theoretical lift for their calculation. Atmospheric wind shear can be included in the multiple streamtube model. This model is still inadequate for flow field description. Wilson's model can be applied only for a fast running lightly loaded wind turbine.

Strickland [34] also presents a multiple streamtube model for a vertical axis Darrieus turbine. In his model, for the calculation of induced velocity, he equates the blade element forces (induced airfoil drag) to the change in the momentum along each streamtube. The basic difference between Wilson's and Strickland's model is that Wilson used the lift force (theoretical)only in the calculation of induced velocity while Strickland added the effect of drag force as well for the similar calculation. But this model doesn't include the effect of local Reynolds number on the lift drag characteristics. This model gives better picture of the overall performance of Darrieus turbine only when the rotor is lightly loaded. It displays improvement over the single streamtube methods.

Shankar [33] presents streamtube models with both uniform and nonuniform velocity distribution. In his uniform velocity distribution model, he assumes a constant axial-flow velocity in the vertical and horizontal directions of the rotor (curved- bladed) frontal area and both in the upwind and downwind sides of the rotor. Shankar's nonuniform velocity distribution model is actually the multiple streamtube model where the axial flow velocity varies both in the vertical and horizontal directions but in each streamtube it remains constant throughout the upwind and downwind sides. In the calculation of Shankar, he applied the lift-drag characteristics independent of Reynold's number like that of Strickland.

Sharpe [34] presents an elaborate description of a multiple streamtube model. Although his model is similar to that of Strickland[36], he includes the effect of Reynolds number in the calculation. Furthermore he uses analytical expression for the Troposkien shape.

Read and Sharpe [30] proposed an improved version of multiple-streamtube model for vertical axis Darrieus turbines. In their model, instead of parallel stream-tube concept, they proposed the idea of expanding streamtube. This model is strictly applicable to low solidity, lightly loaded wind turbines with large aspect ratio. It can predict the instantaneous aerodynamic blade forces and induced velocities better than that by the conventional multiple streamtube model. But prediction of overall power coefficients can not be made with reasonable accuracy. It usually gives lower power than that obtained by experiment.

An elaborate study of the flow curvature effect on the performance prediction of a straight-bladed Darrieus turbines have carried out by Migliore and Wolfe [23]. In their method, they consider a curvilinear flow field which consist of concentric streamlines pattern on the turbine blade airfoil (geometric airfoils). With the aid of conformal mapping techniques, the actual (geometric) airfoil in the curved flow is transformed to an equivalent (virtual) airfoil in a rectilinear flow with change in camber and incidence angle. By this approach, local velocities and angles of attack are preserved, so that the virtual airfoil should exhibit the aerodynamic behavior of the geometric airfoil in orbit. They have observed strong influence of flow curvature on the performance characteristics of a Darrieus turbine especially at high chord-radius ratio. They also noted that under most circumstances flow curvature effect has a detrimental effect on the blade aerodynamic efficiency. However, when properly considered, virtual aerodynamics may be used advantageously to enhance turbine performance. In addition they describe the effect of centrifugal forces on the flow pattern of the blade airfoils of the turbine.

3.3 Vortex Theory.

Larsen [16] first presents a vortex theory for the performance prediction of a cyclogiro windmill. His model is a two-dimensional one but if the vortex trailing from the rotor blade tips are considered it may not be said strictly two dimensional. However, in his model angle of attack is assumed small, as a result stall effect is neglected.

Strickland, Webster and Nguyen [39] have presented a vortex model for curved bladed Darrieus turbine. It is simply the extension of the previous vortex model. This model is a three- dimensional one and aerodynamic stall is incorporated into the model. The general analytical approach requires that the rotor blades be divided into a number of segments along their span. The production, convection and interaction of vortex systems springing from the individual blade elements are modeled and used to predict the "induced velocity" or "perturbation velocity" at various points in the flow field. The induced or perturbation velocity at a point is simply the velocity which is superimpose on the undisturbed wind stream by the wind machine. Having obtained the induced velocities, the lift and drag of the blade segments can be obtained using airfoil section data.

A simple representation of the vortex system associated with a blade element is shown in the Figure 3.10. The airfoil blade element is replaced by a "bound" vortex filament sometimes called "substitution" vortex filament or a lifting line. the strengths of the bound vortex and each trailing tip vortex are equal as a consequence of the Helmhotz theorems of vorticity. According to the Figure 3.10, the strengths of the shed vortex systems have changed on several occasions. On each of these occasions, a spanwise vortex is shed whose strengths is equal to the change in the bound vortex strength as depicted by Kelvin's theorem.

The fluid velocity at any point in the flow field is the sum of the undisturbed wind stream velocity and the velocity induced by all of the vortex filaments in the flow field. The velocity induced at a point in the flow field by a single vortex filament can be obtained from the Biot- Savart law, which relates the induced velocity to the filament strength. Referring to the case shown in the Figure 3.11, for a straight vortex filament of strength Γ and length l, the induce velocity $\vec{V}_p$ at a point p not on the filament is given by,

$$\vec{V}_p = \vec{e}\,\frac{\Gamma}{4\pi d}\left(Cos\theta_1 + Cos\theta_2\right) \tag{3.3.1}$$

where d is the minimum distance of the point p from the vortex filament, $\vec{e}$ is the unit vector in the direction if $\vec{r} \times \vec{l}$. $\vec{r}$ is also the unit vector. It should be noted that if point p should happen to tie on the vortex filament, equation (3.3.1) yields indeterminate results, since e cannot be defined and the magnitude of V_p is infinite. The velocity induced by a straight vortex filament on itself is, in fact, equal to zero.

In order to allow closure of the vortex model, a relationship between bound vortex strength and the velocity induced at a blade segment must be obtained . A relationship between the lift L per unit span on a blade segment and the bound vortex strength Γ_B is given by the Kutta-Joukowski law. The lift can also be formulated in terms of the airfoil section lift coefficient C_l . Equating ship between the bound vortex strength and the induced velocity at a particular blade segment.

$$\Gamma_B = \frac{1}{2} C_l \, C \, W \tag{3.3.2}$$

It should be noted that the effects of aerodynamic stall are automatically introduced in to the equation (3.3.2) through the section lift coefficient. After determining the induced velocity distribution, it becomes straight-forward to obtain the performance characteristics of a Darrieus rotor.

3.4 Cascade Theory.

A cascade theory for the performance prediction of a vertical-axis Darrieus turbine has been presented by A.C. Mandal [18] in his Ph.D. thesis. This theory predicts reasonably good performance for a high solidity as well as low solidity Darrieus turbine. The calculated values of the local forces are comparable with those calculated by the quasisteady vortex model presented by Strickland [39]. For the prediction of overall performance of a high solidity straight-bladed Darrieus wind turbine and local forces of both low and high solidity turbines at the high tip speed ratio, application of cascade theory gives more reliable results in comparison to those by the multiple streamtube theory with flow curvature effect.

This theory does not make any convergence problem even for a high solidity turbine and at high tip-speed ratio. In this model unlike in the case of momentum theory, the iterated ratio may go below 0.50. Applying cascade theory the wake velocities can be predicted very reasonably even for a high solidity turbine and at high tip speed ratio while the momentum theory can not do so.

CHAPTER 4

AERODYNAMIC THEORY

In the cascade theory [25], the blade airfoils of a turbine are assumed to be positioned in a plane surface (termed as cascade) with the blade interspace equal to the turbine circumferencial distance divided by the number of blades. In this model the relationship between the wake velocity and the freestream velocity is established by using the Bernoulli's equation while the induced velocity is related to the wake velocity through a particular assumed analytical expression.

4.1 Basic Assumptions.

In order to simplify the analysis with cascade theory for the determination of the performance characteristics of a Darrieus wind turbine the following assumptions are made:

1. The blades on the cylindrical surface (cylinder with height H) are assumed to be developed into a plane surface. This configuration is known as the rectilinear cascade.

2. As the turbine blade rotates in a circular path,the flow velocity on the blade continuously varies; as a result at any instant each of the turbine blades faces flow conditions different from those on others. In the present analysis one of the blades is considered as the reference blade and at any instant power is calculated with supposition that each of the blades sees the same flow and produces the

same power as that of the reference blade . This process is continued at every station with the reference blade for one complete revolution of the turbine . Later the average power is obtained.

3. The wake velocity for the upstream side is supposed to act in the axial direction and behaves as the freestream velocity on the downstream which is positioned behind the upstream blade. The pressure in the wake region of the upstream side is assumed to be equal to the atmospheric pressure.

4. During finding the wake velocity the flow is assumed to be steady, one-dimensional and incompressible.

4.2 Blade Element Angles and Velocities.

In the present analysis the flow velocities in the upstream and the downstream sides of the turbine are not constant (Figure 4.1), it may be observed that the flow is considered to occur in the axial direction, The expressions of the chordal velocity component V_{cu}, the normal velocity component V_{nu} for the upstream side are respectively obtained following the equation (3.8) and (3.9) in the section 3.2.1.

$$V_{cu} = R\omega + V_{au} Cos\theta \tag{4.1}$$

$$V_{nu} = V_{au} Sin\theta \tag{4.2}$$

Referring to the Figure 4.1, the angle of attack α_{ou} for the upstream side may be expressed as,

$$\alpha_{ou} = tan^{-1}\left(\frac{V_{nu}}{V_{cu}}\right) \tag{4.3}$$

Introducing the value of V_{nu} and V_{cu} and non-dimensionalizing,

$$\alpha_{ou} = tan^{-1}\left[\frac{Sin\theta}{\left(\frac{R\omega}{V_\infty}\right) / \left(\frac{V_{au}}{V_\infty}\right) + Cos\theta}\right] \tag{4.4}$$

The relative flow velocity W_{ou} for the upstream side is obtained as (Figure 4.2).

$$W_{ou} = \sqrt{V_{cu}^2 + V_{nu}^2} \tag{4.5}$$

After inserting the values of V_{cu} (4.1) and V_{nu} (4.2) and nondimensionalizing the equation (4.5) becomes,

$$\begin{aligned} \frac{W_{ou}}{V_\infty} &= \frac{W_{ou}}{V_{au}} \cdot \frac{V_{au}}{V_\infty} \\ &= \frac{V_{au}}{V_\infty}\sqrt{\left[\frac{R\omega}{V_\infty} / \frac{V_{au}}{V_\infty} + cos\theta\right]^2 + Sin^2\theta} \end{aligned} \tag{4.6}$$

Following the same procedure , similar expressions are obtained for the downstream side. Hence to determine the angle of attack α_{ou} and the relative flow velocity W_{od} for the downstream side subscript u is replaced by d in equations (4.4) and (4.6).

After determination of the local relative flow velocity and the angle of attack,the straight- bladed Darrieus turbine is developed into the cascade configuration which is shown in the Figure 4.3. If the blade represented by (1) at an azimuth angle θ is considered as the reference blade, the flow conditions on the other blades represented by (2) and (3), are assumed to be same to that of the reference blade. This process is continued for one complete revolution of the reference blade with a step $\delta\theta$.

In the following analysis, the general mathematical expression are derived for the upstream and the downstream sides by omitting the subscripts u and d. These general expressions may be applied for both the upstream and downstream sides by subscripting the variable parameters (dependent of sides of turbine) with u (upstream) and d (downstream).

Figure 4.4 shows the velocity diagram on the reference blade element of the cascade configuration for a straight-bladed Darrieus turbine . To perform the analysis a control surface is chosen as shown in this figure, This control surface consists of two parallel lines to the cascade front and two identical streamlines having interspace t. This figure also shows velocities in reference to the blade element in the cascade. Referring to the Figure 4.3, the expressions of these velocities are obtained as,

$$\frac{W_y}{V_\infty} = \frac{W_o}{V_\infty} Cos\alpha_o \tag{4.7}$$

$$\frac{W_x}{V_\infty} = \frac{W_o}{V_\infty} Sin\alpha_o \tag{4.8}$$

$$\frac{W_1^2}{V_\infty^2} = \frac{W_x^2}{V_\infty^2} + \frac{(W_y - V_\Gamma)^2}{V_\infty^2} \tag{4.9}$$

$$\frac{W_2^2}{V_\infty^2} = \frac{W_x^2}{V_\infty^2} + \frac{(W_y + V_\Gamma)^2}{V_\infty^2} \tag{4.10}$$

where

$$V_\Gamma = \frac{\Gamma H}{2t} = \frac{N\Gamma H}{4\pi R} \tag{4.11}$$

W_x and W_y are the components of the velocity W_o in the x and y directions respectively where x is chosen along perpendicular direction and y is chosen along the parallel direction of the cascade front (Figure 4.3). W_1 and W_2 are the relative flow velocities respectively at the cascade inlet and outlet. Blade airfoil upstream side is termed as cascade inlet and downstream is termed as cascade outlet. V_Γ is the velocity contribution by circulation ΓH. t $(= 2\pi R/N)$ is the blade spacing. The angles of attack at the cascade inlet α_1 and outlet α_2 are obtained as,

$$\alpha_1 = tan^{-1}\left[\frac{\frac{W_x}{V_\infty}}{\frac{W_y + V_\Gamma}{V_\infty}}\right] \tag{4.12}$$

$$\alpha_2 = tan^{-1}\left[\frac{\frac{W_x}{V_\infty}}{\frac{W_y + V_\Gamma}{V_\infty}}\right] \tag{4.13}$$

4.3 Aerodynamic Forces.

Along the bounding streamlines, shown in Figure 4.4, the pressure forces are canceled. Viscous forces can be neglected outside of the boundary layers. There exists only the momentum flux through the straight lines parallel to the cascade front. So the force in the tangential direction due to the rate of change of momentum,

$$F_t = \dot{m}(W_2 Cos\alpha_2 - W_1 Cos\alpha_1) \tag{4.14}$$

Applying the continuity equation the mass flow rate $\dot{m}$ can be found as,

$$\dot{m} = \rho H t W_1 Sin\alpha_1 = \rho H t W_2 Sin\alpha_2 = \rho H t W_x \tag{4.15}$$

From the equation (4.14) and (4.15), the tangential force F_t becomes,

$$F_t = \rho H t(W_2^2 Sin\alpha_2 Cos\alpha_2 - W_1^2 Sin\alpha_1 Cos\alpha_1) \tag{4.16}$$

The force in the normal direction to the cascade may be obtained as,

$$F_n = \dot{m}(W_1 Sin\alpha_1 - W_2 Sin\alpha_2) + Ht(P_1 - P_2) \tag{4.17}$$

where P_1 and P_2 are respectively the pressure at the cascade inlet and outlet. Introducing the value of $\dot{m}$ (4.15), equation (4.17) can be written as,

$$F_n = \rho H t(W_1^2 Sin^2\alpha_1 - W_2^2 Sin^2\alpha_2) + Ht(P_1 - P_2) \tag{4.18}$$

Considering the total cascade loss by a total pressure loss term ΔP_{ov} and using Bernoulli's equation between the cascade inlet and outlet, one obtains,

$$\frac{P_1}{\rho g} + \frac{W_1^2}{2g} = \frac{P_2}{\rho g} + \frac{W_2^2}{2g} + \frac{\Delta P_{ov}}{\rho g} \tag{4.19}$$

Rearranging,

$$(P_1 - P_2) = 2\rho(W_2^2 - W_1^2) + \Delta P_{ov} \tag{4.20}$$

Now introducing value of $(P_1 - P_2)$ in the equation (4.8) and writing $W_1 Sin\alpha_1 = W_2 Sin\alpha_2$ (for the present configuration), the normal force becomes,

$$F_n = \frac{\rho H t}{2}(W_2^2 - W_1^2) + H t \Delta P_{ov} \tag{4.21}$$

The expression of the normal force coefficient C_n, the tangential force coefficient C_t, the non-dimensional normal force F_n^+ and the non-dimensional tangential force F_t^+ in the cascade theory are respectively obtained following the equations (3.21), (3.22), (3.72) and (3.73). These are given below (since α_o is identical to α given by the equations (3.21) and (3.22) while W_o is identical to W given by the equations (3.72) and (3.73), α and W are replaced by α_o and W_o respectively).

$$C_n = C_l Cos\alpha_o + C_d Sin\alpha_o \tag{4.22}$$

$$C_t = C_l Sin\alpha_o - C_d Cos\alpha_o \tag{4.23}$$

$$F_n^+ = C_n \frac{W_o^2}{V_\infty^2} \tag{4.24}$$

$$F_t^+ = C_t \frac{W_o^2}{V_\infty^2} \tag{4.25}$$

4.4 Velocity Contributed by Circulation and Total Power Loss Term.

The circulation about the blade profile is defined as,

$$\Gamma = \oint_s \vec{W} d\vec{s} \tag{4.26}$$

The circulation along the streamlines is canceled by virtue of the opposite directions of s, while the contribution along the parallel direction of the cascade front is retained. As a result the circulation becomes,

$$\Gamma = t(W_2 Cos\alpha_2 - W_1 Cos\alpha_1) \tag{4.27}$$

From the equations (4.14), (4.15) and (4.16) one obtains,

$$F_t = W_x \Gamma H \tag{4.28}$$

Referring to the Figure 4.5, the lift force can be written as,

$$L = L_{id} + L_v \tag{4.29}$$

where, L_{id} and L_v are respectively the lift force appearing in frictionless flow and the lift force due to pressure loss.

According to the Figure 4.5, L_{id} and L_v may be expressed as,

$$L_{id} = \frac{F_t}{Sin\alpha_o} \tag{4.3}$$

$$L_v = D\,Cot\alpha_o \tag{4.31}$$

where D is the drag force on the blade airfoil. The equations (4.29), (4.30) and (4.31) yield,

$$L = \frac{F_t}{Sin\alpha_o} + D\,Cot\alpha_o \tag{4.32}$$

Dividing both sides of the equation (4.32) by L, introducing $\varepsilon = \frac{D}{L}$ and arranging,

$$\frac{F_t}{LSin\alpha_o} = (1 - \varepsilon Cot\alpha_o) \tag{4.33}$$

Rearranging,

$$L = \frac{F_t}{Sin\alpha_o(1 - \varepsilon Cot\alpha_o)} \tag{4.34}$$

Introducing the value of F_t from the equation (4.28), the lift force L becomes,

$$L = \frac{\rho W_x H}{Sin\alpha_o} \cdot \frac{\Gamma}{(1 - \varepsilon Cot\alpha_o)} \tag{4.35}$$

Referring to the Figure 4.4, one may write $W_x = W_o Sin\alpha_o$, so the lift force L can be expressed as,

$$L = \rho H W_o \frac{\Gamma}{(1 - \varepsilon Cot\alpha_o)} \tag{4.36}$$

The lift force is defined as,

$$L = \frac{1}{2} C_l \rho W_o^2 C H \tag{4.37}$$

From the equations (4.36) and (4.37) the expression of the circulation is obtained as,

$$\Gamma = \frac{1}{2} C_l C W_o (1 - \varepsilon Cot\alpha_o) \tag{4.38}$$

Now the expression of V_Γ from the equations (4.11) and (4.38) are obtained as,

$$V_\Gamma = \frac{1}{8\pi} . C_l . \frac{NC}{R} . W_o (1 - \varepsilon Cot\alpha_o) H \tag{4.39}$$

In the non-dimensional form, the equation (4.39) becomes,

$$\frac{V_\Gamma}{V_\infty} = \frac{1}{8\pi} . C_l . \frac{NC}{R} . \frac{W_o}{V_\infty} (1 - \varepsilon Cot\alpha_o) H \tag{4.40}$$

Now an expression of the pressure loss term P_{ov} will be derived. From the Figure 4.5, the normal force can be obtained as,

$$F_n = F_{nid} + F_{nv} \tag{4.41}$$

where F_{nid} is the force appearing in the frictionless flow and F_{nv} is the force due to the pressure loss. Referring to the Figure 4.5, F_{nv} may be expressed as,

$$F_{nv} = \frac{D}{Sin\alpha_o} \tag{4.42}$$

The force F_{nv} may also be expressed as,

$$F_{nv} = Ht\Delta P_{ov} \tag{4.43}$$

From the equations (4.42) and (4.43) one obtains,

$$\Delta P_{ov} = \frac{D}{tHSin\alpha_o} \tag{4.44}$$

The drag force D is defined as,

$$D = \frac{1}{2}C_d\rho W_o^2 CH \tag{4.45}$$

Now from the equations (4.44) and (4.45), one obtains,

$$P_{ov} = \frac{\rho}{2}.\frac{C_d}{Sin\alpha_o}.\frac{C}{t}W_o^2 \tag{4.46}$$

where

$$\frac{C}{t} = \frac{NC}{2\pi R} = \frac{1}{2\pi}.\frac{NC}{R} \tag{4.47}$$

In non-dimensionalized form,

$$\frac{\Delta P_{ov}}{\rho V_\infty^2} = \frac{1}{4\pi}.\frac{C_d}{Sin\alpha_o}.\frac{NC}{R}.\frac{W_o^2}{V_\infty^2} \tag{4.48}$$

4.5 Velocity Ratios and Rotor Power Coefficients.

The wake velocities for the upstream and downstream sides of the turbine are obtained by applying Bernoulli's equation with absolute velocity and that with relative flow velocity.

Applying Bernoulli's equation with absolute velocity in front and behind the cascade one obtains for the upstream side,

$$\frac{V_\infty^2}{2g} + \frac{P_\infty}{\rho g} = \frac{V_{au}^2}{2g} + \frac{P_{1u}}{\rho g} \tag{4.49}$$

$$\frac{V_e^2}{2g} + \frac{P_\infty}{\rho g} = \frac{V_{au}^2}{2g} + \frac{P_{2u}}{\rho g} \tag{4.50}$$

where V_{au} and V_e are respectively the induced velocity and the wake velocity for the upstream side. P_{1u} and P_{2u} are the static pressures respectively at the cascade inlet and outlet for the upstream side. In the wake region of the upstream side with the velocity V_e, the pressure is assumed to be equal to the atmospheric pressure (Figure 4.1). Subtracting the above equations (4.49) and (4.50),

$$\frac{V_\infty^2}{2g} - \frac{V_e^2}{2g} = \frac{P_{1u}}{g} - \frac{P_{2u}}{g} \tag{4.51}$$

After rearranging,

$$(P_{1u} - P_{2u}) = \frac{1}{2}\rho(V_o^2 - V_e^2) \tag{4.52}$$

Now subtracting the variable parameters in the equation (4.20) by u for the upstream side and balancing with the equation (4.52) one obtains,

$$\frac{1}{2}\rho(V_o^2 - V_e^2) = \frac{1}{2}(W_{2u}^2 - W_{1u}^2) + \Delta P_{ov} \tag{4.53}$$

Again the subscripting the variable parameters in the equation (4.48) by u for the upstream side. introducing in the equation (4.53) and dividing throughout by $\frac{1}{2}\rho$

one may find,

$$V_o^2 - V_e^2 = (W_{2u}^2 - W_{1u}^2) + \frac{1}{2}\pi.\frac{NC}{R}.\frac{C_{du}}{Sin\alpha_{ou}}.W_{ou}^2 \tag{4.54}$$

From the equation (4.54), the expression of the wake velocity ratio in non-dimensionalized form for upstream side can be written as,

$$V_e = \sqrt{1 - \left(\frac{W_{2u}^2}{V_\infty^2} - \frac{W_{1u}^2}{V_\infty^2}\right) - \frac{1}{2}\pi\frac{NC}{R}\frac{C_{du}}{Sin\alpha_{ou}}.\frac{W_{ou}^2}{V_{ou}^2}} \tag{4.55}$$

Similarly the expression of the wake velocity ratio in non- dimensionalized form for the downstream side can be found as,

$$V_w = \sqrt{1 - \left(\frac{W_{2d}^2}{V_e^2} - \frac{W_{1u}^2}{V_e^2}\right) - \frac{1}{2}\pi\frac{NC}{R}\frac{C_{dd}}{Sin\alpha_{od}}.\frac{W_{od}^2}{V_e^2}} \tag{4.56}$$

The wake velocity ratio for the downstream side may be related as,

$$\frac{V_w}{V_\infty} = \frac{V_w}{V_e}.\frac{V_e}{V_\infty} \tag{4.57}$$

In this model, for the upstream side a relationship between the wake velocity and the induced velocity is given as,

$$\frac{V_{au}}{V_\infty} = \left(\frac{V_e}{V_\infty}\right)^{k_i} \tag{4.58}$$

and for the downstream side as,

$$\frac{V_{ad}}{V_e} = \left(\frac{V_w}{V_e}\right)^{k_i} \tag{4.58}$$

The value of the exponent k_i is found from the a fit of experimental results. The induced velocity ratio for the downstream side may also be written in the form,

$$\frac{V_{ad}}{V_\infty} = \frac{V_{ad}}{V_e}.\frac{V_e}{V_\infty} = \frac{V_e}{V_\infty}.\left(\frac{V_w}{V_e}\right)^{k_i} \tag{4.60}$$

Induced velocity ratio depends on many parameters such as, solidity, tip speed ratio, azimuth angle, Reynolds number, aspect ratio, blade pitching and airfoil profile. In the iterative process, the effect of every parameter except solidity is taken care of through the airfoil characteristics which control circulation. Thus the exponent k_i becomes the function of solidity only. The expression of the exponent is obtained as,

$$k_i = (.425 + .332\sigma) \tag{4.61}$$

where σ is solidity of a Darrieus wind turbine.

The expressions, for the tangential force F_t and the normal force F_n, may be used for the upstream and the downstream sides by subscripting the variable parameters with u (upstream) and d (downstream). The equations (4.16) and (4.21) are expressed in the following forms inserting $t = 2\pi\frac{R}{N}$.

$$F_t(\theta) = \frac{2\pi}{N}.HR(W_2^2 Sin\alpha_2 Cos\alpha_2 - W_1^2 Sin\alpha_1 Cos\alpha_1) \tag{4.62}$$

$$F_n(\theta) = \frac{\pi}{N}.HR(W_2^2 - W_1^2) + \frac{2\pi}{N}.HR\Delta P_{ov} \tag{4.63}$$

Since the tangential and the normal forces represented by the equations (4.62) and (4.63) are for any azimuthal position,so from now on they are considered as a function of azimuth angle θ.

The average tangential force on each blade is expressed as,

$$F_{t_a} = \frac{1}{2\pi}\int_0^{2\pi} F_t(\theta)d\theta \tag{4.64}$$

The total torque for the number of blades N is expressed as,

$$Q = NF_{t_a}R \tag{4.65}$$

From the equations (4.62), (4.64) and (4.65) one obtains,

$$Q = \rho H R^2 \int_0^{2\pi} F_t(\theta) d\theta \tag{4.66}$$

The turbine torque coefficient is defined by,

$$C_Q = \frac{Q}{\frac{1}{2}\rho A V_\infty^2 R} \tag{4.67}$$

Introducing the value of Q from the equation (4.66), inserting $A = 2RH$, one may obtain the expression of the turbine overall torque coefficient as,

$$C_Q = \int_0^{2\pi} \left(\frac{W_2^2}{V_\infty^2} Sin\alpha_2 Cos\alpha_2 - \frac{W_1^2}{V_\infty^2} Sin\alpha_1 Cos\alpha_1 \right) d\theta \tag{4.68}$$

The turbine overall power coefficient is given by the equation

$$C_p = \lambda . C_Q \tag{4.69}$$

The numerical calculation to obtain the overall power coefficient is carried out following the procedure given in the appendix - A.

4.6 Development of Dynamic Stall.

The dynamic stall is a complex unsteady flow phenomena, which refers to the stalling behavior of an airfoil section when the angle of attack changes rapidly with time. Several experimental works have been conducted in this field, especially for helicopter applications [10],[20]. These studies showed that the loads of an airfoil oscillating harmonically in pitch are different from those of a nonpitching airfoil at the same angle of attack.

In the case of the Darrieus wind turbine, as the turbine blade rotates, the local angle of attack changes continuously with time. At low tip speed ratio the angle of attack exceeds the stalling angle in most of the stations, thus the dynamic stalling effect is needed to be encountered in the analysis. To include the effect of dynamic stall in the analysis, Boeing-Vertol method [12] is applied to determine the lift characteristics.

In the method of Boeing-Vertol, the blade angle is modified. the modified angle of attack α_m is determined from following the relation,

$$\alpha_m = \alpha - \gamma K_l \left(\left| \frac{C\dot{\alpha}}{2W_o} \right| \right) S_{\dot{\alpha}} \tag{4.70}$$

where α is the effective blade angle of attack, γ and K_l are empirical constants, $\dot{\alpha}$ represents the instantaneous rate of change of α, $S_{\dot{\alpha}}$ is the sign of $\dot{\alpha}$ and W_o is the relative flow velocity.

This modified angle of attack is used to calculate lift force coefficient due to the dynamic stalling effect in the following manner,

$$C_{ld} = \left(\frac{\alpha}{\alpha_m} \right) C_l(\alpha_m) \tag{4.71}$$

where $C_l(\alpha_m)$ is the lift value chosen corresponding to the modified angle of attack α_m and the value is taken from the two- dimensional lift characteristics with static stall conditions.

For low Mach numbers and for airfoil thickness to chord radius ratios greater than 0.1, the value of γ is

$$\gamma = 1.4 - 6(0.06 - t_c) \tag{4.72}$$

where t_c is the maximum airfoil thickness ratio. The K_l value changes with the sign of the effective angle of attack, and this is determined from,

$$K_l = 0.75 + 0.25.S_{\dot{\alpha}} \tag{4.73}$$

This formulation is applied when the angle of attack , α is greater than the static stall angle or when the angle of attack is decreasing after having been above the stall angle. The Boeing-Vertol stall model is turned off when the angle of attack is below the stall angle and increasing.

For the prestall condition the lift characteristics are also corrected. These are determined approximately from an empirical relation which is obtained from the correlation of the results presented by N.D. Ham [14]. This empirical relation for corrected lift may be expressed in the form,

$$C_{l_c} = C_l(1 + .03\alpha) \tag{4.74}$$

In the analysis, to consider the effect of drag characteristics due to the dynamic stall, an empirical relation is introduced which can be written in the form,

$$C_{dd} = \frac{C_{ld}}{C_l(\alpha)}.C_d(\alpha).(K) \tag{4.75}$$

where K if a factor. K is chosen as 1 in this expression.

Experimental values for drag characteristics with dynamic stall effect is not available. However, the calculated drag values obtained from the equation (4.75) becomes closer to the calculated values presented by Cardona [2].

In the reference [27], for the SWECS model, in order to consider the dynamic stall effect, the drag was modified and it was considered as the function of lift and angle of attack. However that failed to provide reasonable correlations while used in the present analysis.

CHAPTER 5

RESULTS AND DISCUSSIONS

In this chapter the calculated results are presented. the effects of Reynolds number, solidity, zero-lift-drag coefficient, aspect ratio etc. on the performance of Darrieus wind turbines are discussed. The calculated results by cascade theory considering dynamic stall are compared with the experimental results and the calculated values by the other existing methods. Most of the experimental results are available from the wind tunnel test data and few are available from the prototype turbine test data.

In the present analysis, two types of airfoils are considered. These are NACA 0012 and NACA 0015. Two dimensional aerodynamic lift-drag characteristics are taken from the reference [18], which are shown in graphical form in Appendix-E. However, to consider dynamic stall, modified values are used in the analysis.

5.1 Calculated Results.

5.1.1 Effect of Dynamic Stall on Lift-Drag Characteristics.

Figures 5.1 to 5.3 depict the effect of dynamic stall on lift-drag characteristics of airfoil blade section. From Figure 5.1, it is observed that a large difference exists between the static lift characteristics and the experimental data presented by N.D.Ham et al [14]. However it is revealed from this figure that the calculated lift characteristics including dynamic stall effect are closer to the experimental lift values.

Figure 5.2 shows the variation of the static lift and the calculated dynamic lift characteristics while Figure 5.3 shows the variation of the static drag and the calculated dynamic drag characteristics. It can be seen from the figure that there occur remarkable variation of both lift and drag after the stalling angle. It occurs due to completely different flow phenomena in the case of dynamic stalling condition. In this regard U.B. Mehta [22] has provided few analytical informations concerning the flow phenomena with dynamic stalling effect. They have found different flow characteristics for the dynamic stalling condition.

According to them, as the airfoil angle of attack, α exceeds the static stall angle, a separation bubble forms near the leading edge (Figure 5.4a). The flow tends to reattach aft of the bubble and a second bubble occurs near the trailing edge. As the angle of attack increases, the leading edge bubble grows in strength and the aft bubble now has two centers (Figure 5.4b). The suction pressure at these bubbles or vortices increases. In Figure 5.4c, the leading edge vortex gains in strength and is moving aft as the trailing edge suction pressure increases. In Figure 5.4d to 5.4f, the leading edge vortex breaks free of the surface and moves aft as it gains in strength. The increased pressure suction associated with this vortex also moves aft. Meanwhile, the aft vortex has been swept off the trailing edge (Figure 5.4d). The rearward movement of the vortices produces an increased vertical load on the airfoil and rearward shift of the center of pressure.

In Figure 5.1, the comparison of the dynamic lift and the experimental dynamic values are made and reasonable correlation was found.

The dynamic drag characteristics could not be correlated with the experimental values because of its nonavailability. However, in the region of the dynamic stalling the calculated values provided by Cardona [2] gives a closer correlation.

Introducing the present expression of lift-drag characteristics to consider dynamic stalling effect, the calculated local values of tangential and normal forces give reasonable correlation with the experimental values which also justify the validity of the expressions for dynamic lift and drag.

5.1.2 Effect of Solidity.

In Figures 5.5, 5.6 and 5.7, the effects of varying solidity are shown on overall power, torque and drag coefficients calculated by cascade theory considering dynamic stall. Aspect ratio, height-diameter ratio, number of blades, blade chord and wind speed are kept constant. Only the solidity is varied. Since wind speed and the blade chord are kept constant, wind speed Reynolds number becomes fixed. Solidity changes with the change in radius. To include all full-scale Darrieus turbine, solidity is varied from 0.10 to 1.20. Figure 5.5 shows that with increase in solidity peak power coefficient increases, and becomes maximum at $\sigma = 0.30$. Further increase in solidity results in fall of peak power coefficient. However, lowering the solidity results in flattening out of the performance curve. At higher solidity, peak power drops adequately, with sharp change in power near the peak, and operating range shifts towards the low tip speed ratio. Though peak power drops at higher solidity, Figure 5.6 shows that the torque at low tip speed ratio increases which is better from the point of view of self-starting. The pattern of the torque variation with the angle of attack is similar to that of the power coefficient variation with the angle of attack, which is desirable. Figure 5.7 shows that overall drag coefficient increases with increase in solidity. From structural point of view, a low solidity turbine is better because of its lower overall drag force.

5.1.3 Effect of Blade Airfoil Profile.

Figure 5.8 shows a comparison of overall power coefficients for two symmetrical airfoils NACA 0012 and NACA 0015. The performance curves show that NACA 0012 airfoils gives improved results in negligible amount at higher tip speed ratios while NACA 0015 airfoils shows improved results at lower tip speed ratios. But the maximum power coefficients for both airfoils are nearly same. Since stalling has significant effect at lower tip speed ratios, the performance curves show that NACA 0015 has a favorable stall characteristics. For this reason, in most cases a symmetrical NACA 0015 is recommended for the Darrieus turbine. At higher tip speed ratios, NACA 0015 airfoil gives lower power coefficients. This is due to higher blade airfoil drag coefficients in comparison to those by the blade airfoil NACA 0012.

5.1.4 Effect of Reynolds number.

In Figure 5.9, the effects of Reynolds number at constant wind speed on the overall power coefficients are shown. The analysis has been performed at fixed solidity, height- diameter ratio and number of blades. This Figure reveals that Reynolds Number has a prominent influence on the performance of the Darrieus turbine. With the increase in Reynolds number power coefficient increases. This happens due to higher lift and lower drag with increasing Reynolds number, which makes the tangential force higher.

5.1.5 Effect of Aspect Ratio.

The effect of varying aspect ratio on the power coefficient, while keeping solidity, blade chord, number of blades, wind speed constant, is shown in Figure 5.10. It can be noted that, turbine with low aspect ratio gives reduced performance. This occurs due to reduced lift/drag ratio for finite aspect ratio consideration. At infinite aspect ratio, the power coefficient is about 35% greater than the maximum value at the aspect ratio of 0.5.

5.1.6 Effect of Zero-Lift-Drag Coefficient.

Figure 5.11 presents the effects of zero-lift-drag coefficient on overall power coefficient. The wind speed, solidity, blade chord, number of blades, height-diameter ratio are kept constant. Thus wind speed Reynolds number becomes constant. The Figure shows that, with the increase in zero-lift- drag coefficient, maximum power coefficient decreases. Hence, this parameter should be as small as possible. Zero-lift-drag coefficient is function of Reynolds number as well as chord- radius ratio. With the increase in Reynolds number, the zero- lift-drag coefficient decreases. Therefore, a large wind turbine, whose blade Reynolds number is large, produces higher power coefficient.

5.1.7 Effect of Drag due to Blade Supporting Struts.

The effect of blade supporting strut drag on overall power coefficient is shown in Figure 5.12. The turbine, used in the analysis, has six struts for supporting the three blades. Strut drag coefficient depends on strut shape. Figure 5.12 shows that strut drag coefficient i.e. strut shape, has a remarkable effect on the turbine performance. Loss in power due to strut is proportional to the cube of the tip speed ratio. Hence for the same strut drag coefficient, as the tip speed ratio increase, reduction of power coefficient gradually increases. Also with increase in strut drag coefficient, maximum power coefficient drops. Hence it can be concluded that to reduce power loss due to supporting strut, its cross-section should be of airfoil shape whose drag coefficient is relatively small.

5.1.8 Effect of Tip Speed Ratio.

Figure 5.13 to 5.17 give the comparisons of induced velocity ratio, local angle of attack, Reynolds number, local non- dimensional tangential and normal forces, calculated by cascade theory with dynamic stall, at three different tip speed ratios. With the rise of tip speed ratio, more and more air passes outside the turbine blade, hence the induced velocity begin to drop with tip speed ratio which is shown in Figure 5.13. Figure 5.14 shows that at low tip speed ratio, at most of the stations local angle of attack goes above the stall angle. With further rise in tip speed ratio, local angle of attack falls resulting in fewer or no stations above stall. In this regard, it can be said that dynamic stall has profound influence at low tip speed ratio. Decrease in local angle of attack with increase in tip speed ratio can be explained following the Figure 5.13. As tip speed ratio increases, keeping the tangential velocity constant, induced velocity decreases, so does the angle of attack.

For a particular turbine, local Reynolds number is the function of local relative velocity which is the vector sum of the tangential velocity and the induced velocity. At constant turbine speed, tangential velocity is fixed, the wind velocity varies with tip speed ratio. At low tip speed ratio, induced velocities are higher than those at high tip speed ratio (Figure 5.13). At higher tip speed ratio, Reynolds number is mainly dominated by tangential velocity. Since this quantity is fixed, there is relatively small variation of local Reynolds number with azimuth angle, as shown in Figure 5.15, whereas at low tip speed ratio this variation is relatively higher because of higher influence of induced velocity in comparison to that at high tip speed ratio.

At very low tip speed ratio,at most of the stations, the local angles of attack go far beyond above the stall angle (Figure 5.14). At higher angle of attack, due to dynamic stall, lift/drag ratio decreases, resulting in lower local tangential force. But with increase in tip speed ratio, reversal of these effects occur. So that tangential force increases with rise in tip speed ratio. But at higher tip speed ratio, because of lower local angle of attack, tangential force decreases, which is shown in Figure 5.16. Similarly Figure 5.17 showing the non- dimensional normal force distributions at different tip speed ratios can be explained.

5.1.9 Comparative Result of Cascade Theory with and without Dynamic Stall.

Calculated values of local angles of attack, Reynolds number, induced velocity ratios, local non-dimensional tangential and normal forces by cascade theory with and without dynamic stall are compared in Figure 5.18 to 5.22 respectively. The results plotted in these figures are given for a two bladed rotor with a c/R of 0.0715 at tip speed ratios of 1.5 and 3.0 respectively. No significant differences as observed in the values of local angles of attack and Reynolds number distribution obtained with and without consideration of dynamic stall (Figure 5.18 and 5.19). But in the case of induced velocity ratio, remarkable variations occur, as shown in Figure 5.20. Introducing dynamic stall model induced velocity ratio drops. In the region of dynamic stalling, the lift and drag values increase remarkebly which is the reason of lowering the induced velocity, due to the addition of dynamic stalling.

Comparative curves of non-dimensional tangential and normal forces, in the Figure 5.21 and 5.22, show that there are prominent difference of forces calculated with and without stall consideration. Incorporating dynamic stalling effect, both lift and drag values rise. Tangential force coefficient is strongly affected by lift compared to that by drag. Tangential force coefficient increases due to higher lift and it results in higher value of tangential forces. Variaton of the non-dimensiol normal forces can be explained in the similar way.

5.2 Comparisons of Calculated and Experimental Results.

Comparisons are made for overall power coefficients, local blade forces and wake velocities. However it may be mentioned that experimental data available at the present moment for the straight-bladed wind turbine are not sufficient.

5.2.1 West Virginia University Prototype.

Figure 5.23 shows the comparison of the calculated values with and without dynamic stall and the experimental data. These data are presented by Migliore et al [24] for the outdoor test model of West Virginia University. It is observed from the figure that at a higher tip speed ratio side, calculated values with and without dynamic stall,an closer and give reasonable correlation with the experimental data At high tip speed ratio, dynamic stall have no influence, because no stations are in the stalling region. In the low tip speed ratio side correlation is not good. Calculated value with and without stalling effect differ in small amount in the lower tip speed ratio range. Minor rising tendency of the values with dynamic stall is due to higher lift value in this case of constant turbine speed condition.

5.2.2 Virje Universitiet Brussel (VUB) Turbines.

In Figures 5.24 and 5.25, comparisons of the calculated values and experimental data [5] of VUB wind tunnel test model are shown. The Figure 5.26 shows the comparison of the calculated values and the field test data of 6-m diameter turbine. The model test was conducted at constant wind speed while the prototype was tested at variable wind speeds. For the prototype turbine, in the theoretical calculations of power coefficients wind speed Reynolds number is chosen as 510000 based on average wind velocity. Figures 5.24 and 5.25 show that for the wind tunnel test model correlations are reasonable for both methods. At low tip speed ratio range no experimental data are available. At low tip speed ratio side, power coefficients because lower with dynamic stall than those without dynamic stall. For dynamic stall, lift values increase and also does the tangential force coefficient. But relative flow velicity decrease more than that without dynamic stall for constant wind speed condition and the combined effects reduce the overall power coefficients. For the prototype turbine very few experimental data are available at the present moment and these are given in the low tip speed ratio range. From the Figure 5.26 it is observed that the agreement between the calculated and experimental results is quite good .

5.2.3 Reading University Prototype.

The comparisons of the calculated and experimental data of Reading University prototype is shown in Figure 5.27 and 5.28. The experimental data, one for high solidity and other for low solidity turbine are presented by Musgrove et al [19] [26]. the turbine speeds are varied from 3 m/sec to 7 m/sec. So in the present theoretical analysis, the mean wind speed Reynolds numbers of 86000 and 1380000 are chosen for the low and the high solidity turbines respectively. Very few experimental data are available for these turbines and also these data are scattered. It is seen from these figures that the correlations are quite reasonable.

For a high solidity turbine, at any tip speed ratio before that corresponding to the peak power coefficient, the number of stations in the stalling region is relatively higher in comparison to that for a low solidity turbine. For that reason, this effect is higher for a high solidity turbine.

5.2.4 Sherbrooke University Turbine.

Figures 5.29 to 5.32 give the comparisons of calculated values and the experimental data from Sherbrooke University at two different tip speed ratios 1.5 and 3.0 respectively. The available calculated values of instantaneous forces by double multiple streamtube method with dynamic stall effect [29] are also plotted for comparison. Since the lift-drag characteristics of airfoil NACA 0018 are not available, so for the present calculations lift-drag characteristics of airfoil NACA 0015 are used. It is seen from these figures that the calculated values considering dynamic stall give comparatively better correlation in each of the cases. For the non-dimensional normal forces as the Figures 5.30 and 5.31 reveal, the correlation near the maximum peak value become excellent which is very important from the design point of view since the normal force coefficient effects the design of turbine significantly.

Considering the dynamic stall effect, both lift and drag coefficients increase. But the effects of lift on tangential force coefficient is more prominent than that by drag. As a result, non-dimensional tangential frces increase. On the other hand, normal force coefficient is influenced by the lift as well as by the drag. For this reason non-dimensional normal forces rise.

5.2.5 Sandia Tow Tank Model.

Calculated local blade forces are compared with the experimental results of Sandia tow tank models [38],[39] and [40] in Figures 5.33 to 5.36. The comparisons are made at two different tip speed ratios, 2.5 and 5.0 respectively. The Figures 5.33 and 5.34 show that at low tip speed ratio, the calculated values of instantaneous forces with dynamic stall consideration are improved in comparison to those without dynamic stall consideration and closer to the experimental values. The correlation can be explained in the similar way as in section 5.2.4. Results of non-dimensional tangential and normal forces at a tip speed ratio of 5.0 are shown in Figures 5.35 and 5.36 respectively. At this tip speed ratio, other dynamic effects, such as added mass, unsteady wake circulation have profoud effects and dynamic stalling has minor effect. However the Figures show inprovements in the values of local force coefficients calculated with dynamic stalling . This is due to slightly higher lift values in the prestall region which are obtained from the correlation with the experimental data presented by N.D. Ham [14]

In Figures 5.35 and 5.36 calculated values of forces by quesisteady models are also plotted. The force coefficients calculated with dynamic stall show better agreement with the experimental values than those by vortex model.

Experimental water tank data of wake velocities at one rotor diameter downstream for a straight-bladed Darrieus wind turbine with blade airfoil NACA 0012 are presented by Sandia Laboratories in the reference [38]. The comparisons of the calculated and the experimental wake velocities are shown in Figures 5.37 to 5.40. The available calculated values of wake velocities by dynamic vortex theory and multiple streamtube with curvature effect [38] are also considered for comparison.

The correlation with the calculated data including dynamic stalling effect is reasonable. However, available experimental wake velocities data are at a distance of one rotor diameter. Experimental data of wake velocities at higher distance is also necessary for comparison and it is expecting that the correlation would improve with data at higher distance.

CHAPTER 6

CONCLUSIONS AND RECOMMENDATIONS

In this chapter general conclusions are drawn regarding performance characteristics by cascade model including dynamic stalling effect. Few recommendations are also given for the future works.

6.1 Conclusions.

1. Including the effect of dynamic stall in the cascade theory, the overall values (mean) are changed negligibly at the higher tip speed ratios while they are changed in small amount at the lower tip speed ratios in most of the cases.

2. At low tip speed ratio range there occur remarkable change of the local values such as tangential force coefficients and normal force coefficients.

3. The correlation of the calculated and the experimental results shows that the calculated local values including dynamic stall effect, become relatively closer to the experimental values in comparison to those by the other existing models.

4. Maximum peak force coefficient is very important in the stress analysis of Darrieus turbine blade. The present analysis shows a good correlation in the value of maximum peak normal force coefficient with the experimental results, although in most of the cases, the correlation is not good in the downstream side of the rotor and this is not important from the design point of view.

5. Sufficient experimental data for wake at downstream side at various distances are not available. These are necessary to make correlation with the present calculated values. It is expected that the correlation of wake velocity would improve.

6. Sufficient experimental data are not available to check the expressions of lift-drag characteristics including dynamic stalling effect at the present moment. These are necessary to make further comparison.

7. The cascade theory with dynamic stalling give very reasonable performance prediction compared to that by dynamic vortex model which takes tremendous computation time and often creates convergence problem.

6.2 Recommendations.

1. In the analysis blade pitching moment has not been considered. Though at high tip speed ratio the effect of pitching moment may be neglected, at low tip speed ratio it is necessary to take into account its effect in the analysis.

2. Dynamic effects other than dynamic stall, such as added mass effect, unsteady wake circulation have not been considered. Added mass effect and unsteady wake circulation are important at the higher tip speed ratio range. Introducing these effects, improvement of local forces at higher tip speed ratio may occur.

3. Sufficient experimental blade force data may be obtained on wind tunnel test model as well as full-scale rotors and comparisons with the present calculated values may be made.

4. Additional wake velocity data behind the turbine (either model or prototype) may be determined experimentally.

5. Effect of wind shear is important when the turbine is placed near the ground and this effect has not been considered in the present analysis. So it can be taken into account.

6. In the present analysis, the turbine blades are of symmetric airfoil shape. The analysis may be repeated with the blades of cambered shaped airfoil to see the effect on the turbine performance.

REFERENCES

[1] BLACKWELL, B.F. and SHELDAHL, R.E., "Selected Wind Tunnel Test Results for the Darrieus Wind Turbine", Journal of Energy, Vol.1, No.6, Nov.-Dec. 1977, pp. 382-386.

[2] CARDONA, J.L., "Flow Curvature and Dynamic Stall Simulated with an Aerodynamic Free-Vortex Model for VAWT", Wind Engineering, Vol.8, No.3, 1984, pp. 135-143.

[3] CLANCY, L.J., "Aerodynamics", A Pitman International Text, 2nd Edition, 1978.

[4] CURRIE, I.G., "Fundamental Mechanics of Fluids", McGraw Hill, 1974.

[5] DECLEYRE, W., AERSCHOT, D.V. and HIRSCH, CH., "The Effects of Reynolds Number on the Performance Characteristics of Darrieus Windmills with Troposkien and Straight-Blades", Proceedings of the International Colloquium on Wind Energy, Brighton, August 1981, pp. 243-248.

[6] DOMMASCH, D.O., "Airplane Aerodynamics", Pitman Aeronautical Publications, 3rd Edition, 1961.

[7] DURAND, W.F., "Aerodynamic Theory", Peter Smith, 1976.

[8] ELDRIDGE, F.R., "Wind Machines", Von Nostrand Reinhold Company, New York, 1980.

[9] EPPLER, R. , "Turbulent Airfoil for General Aviation", Journal of Aircraft, Vol.15, Feb. 1978, pp. 39-99.

[10] ERICSSON, L.E. and REDING, J.P., "Engineering Analysis of Dynamic Stall", Proceeding of the ASME Winter Annual Meeting, San Francisco, Calif., Dec. 1978, pp. 117-123.

[11] GOLDING, E.W., "The Generation of Electricity by Wind Power", E. & F.N. Spon Ltd., London, 1955.

[12] GORMONT, R.E., "A Mathematical Model of Unsteady Aerodynamics and Radial Flow for Application to Helicopter Rotors", U.S. Army Air Mobility R & D Laboratory, Vertol Division, Philadelphia, Pa., Report on Boeing-Vertol Contract DAAJOV-71-C-0045, May 1973.

[13] HAM, N.D., "Aerodynamic Loading on a Two-dimensional Airfoil During Dynamic Stall", Journal of the AIAA, Vol 6, No.10, October 1969.

[14] HAM, N.D., AND GARELICK, M.S., "Dynamic Stall Considerations in Helicopter Rotor", Journal of the American Helicopter Society, Vol.13, No.2, April 1968.

[15] HUNT, V.D., "Wind Power", Van Nostrand Reinhold Company, New York, 1981.

[16] LARSEN, H.C., "Summary of a Vortex Theory for the Cyclogiro", Proceedings of the Second U.S. National Conferences on Wind Engineering research, Colorado State University, June 1975, pp. V-8-1-3.

[17] LYSEN, E.H., "Introduction to Wind Energy", SWD Publication, Netherlands, May 1983.

[18] MANDAL, A.C., "Aerodynamics and Design Analysis of Vertical Axis Darrieus Wind Turbines", Ph.D. Thesis, Jan. 1986

[19] MAYS, I.D., MUSGROVE, P.J., "Performance of the Variable Geometry Vertical Axis Wind Turbine at High and Low Solidities", Proceedings of the 1st Wind Energy Association Workshop, April 1979, pp. 48-56.

[20] Mc CROSKEY, J.W. and PUCCI, L.S., "Viscous-Inviscid Interaction on Oscillating Airfoils in Subsonic Flow", AIAA Journal, Vol.20, Feb. 1982, pp. 167-174.

[21] Mc CROSKEY, W.J., "Prediction of Unsteady Separated Flow on Oscillating Airfoils", AGARD Lecture Series on Three-Dimensional and Unsteady Separated Flow at High Reynolds Number (VKI,Belgium), AGARD LS-94, Paper 12, February 1978.

[22] MEHTA, U.B., "Dynamic stall on an Oscillating Airfoil", Proceedings AGARD Fluid Dynamics Panel Symposium on Unsteady Aerodynamics, AGARD CPP-227, September 1977.

[23] MIGLIORE, P.G. and WOLFE, W.P., "The Effects of Flow Curvature on the Aerodynamics of Darrieus Wind Turbines", Department of Aerospace Engineering, WVU, Morgantown, July 1980.

[24] MIGLORE, P.G., WOLFE, W.P. and FANUCCI, J.B., "Flow Curvature Effects on Darrieus Turbine Blade Aerodynamics", Journal of Energy, Vol. 4, No. 2, March-April 1980, pp. 49-55.

[25] MILNE THOMSON, L.M., "Theoretical Aerodynamics", Dover Publications Inc., New York, 4th Edition, 1973.

[26] MUSGROVE, P.J. and MAYS, I.D., "Development of the Variable Geometry Vertical Axis Windmill", Proceedings of the Second International Symposium on Wind Energy Systems, Amsterdam, October 3-6, 1978, pp. e4-39-60.

[27] NOLL, R.B. and HAM, N.D., "Effects of Dynamic Stall on SWECS", Proceedings of the Fifth Biannual Wind Energy conference and Workshop, Washington, D.C., Oct. 5-7, 1981, pp. 295-306.

[28] NOLL, R.B. and HAM, N.D., "Analytical Evaluation of the Aerodynamic Performance of a High-Reliability Vertical- Axis Wind Turbine", Proceeding of AWEA National Conference, 1980.

[29] PARASCHIVOIU, I., "Predicted and Experimental Aerodynamic Forces on the Darrieus Rotor", Journal of Energy, Vol.7, No.6, Nov.-Dec. 1983, pp. 610-615.

[30] READ, S. and SHARPE, D.J., "An Extended Multiple Streamtube Theory for Vertical Axis Wind Turbines", Proceedings of the Second British Wind Energy Association Workshop, Cranfield, April 1980.

[31] REUTER, R.C.JR., SHELDAHL, R.E., "Sandia Vertical Axis Wind Turbine project", Sandia Laboratories Report, SAND76-0581, April-June 1976.

[32] SCHOLZ, N., "Aerodynamics of Cascades", Translated and Revised by Dr.-Ing. Armin Klein from the Original German "Aerodynamic Der Schaufelgitter", AGARD, 1977.

[33] SHANKAR, P.N., "On the Aerodynamic Performance of a Class of Vertical Shaft Windmills", Proceedings of the Royal Society of London, Series A, Vol.349, 1976, pp. 35-51

[34] SHARPE, D.J., "A Theoretical and Experimental Study of the Darrieus Vertical Axis Wind Turbine", School of Mechanical, Aeronautical & Production Engineering, Kingston Polytechnic, Research Report, October 1977.

[35] SHARPE, D.J., "A Vortex Flow Model for the Vertical Axis Wind Turbine", Proceedings of the 1st British Wind Energy Association Workshop, April 1979, pp. 125-133.

[36] STRICKLAND, J.H., "The Darrieus Turbine : A performance Prediction Model using Multiple Streamtubes", Sandial Laboratories Report, San 75-0431, Octber 1975.

[37] STRICKLAND, J.H. and GOLDMAN, A.L., "Preliminary Work Concerning the Near Wake Structure of the Darrieus Turbine", AIAA/SERI Wind Energy Conference, Colorado, April 9-11, 1980, pp. 123-129.

[38] STRICKLAND, J.H., SMITH, T., and SUN, K., "A Vortex Model of the Darrieus Turbine: An Analytical and Experimental Study", Sandia Laboratories Report, SAND81-7017, June 1981.

[39] STRICKLAND, J.H., WEBSTER, B.T. and NGUYEN, T., "A Vortex Model of the Darrieus Turbine: An Analytical and Experimental Study", Journal of Fluids Engineering, Vol.101, No.4, Dec 1979, pp. 500-505.

[40] TEMPLIN, R.J., "Aerodynamic Performance Theory for the NRC Vertical-Axis Wind Turbine", National Research Council of Canada, Report LTR-LA-160, June 1974.

[41] VITTECOQ, P. and LANEVILIE, A., "Etude en Soufflerie d'un rotor du type Darrieus", Mechanical Engineering Department, University of Sherbrooke, Canada, Report MEC-82-2, Aug. 1982.

[42] WALTERS, R.E., FANUCCI, J.B., HILL, P.W. and MIGLIORE, P. G., "Vertical Axis Wind Turbine Development", Dept. of Aerospace Engineering, WVU, Morgantown, July 1979.

[43] WILLMER, A.C., "Low Reynolds Number Tests on the NACA 0015 Section", Proceeding of the 1st British Energy Association Workshop, April 1979, pp. 109-116.

[44] WILSON, R.E. and LISSAMAN, P.B.S., "Applied Aerodynamics of Wind Power Machines", Oregon State University, May 1974.

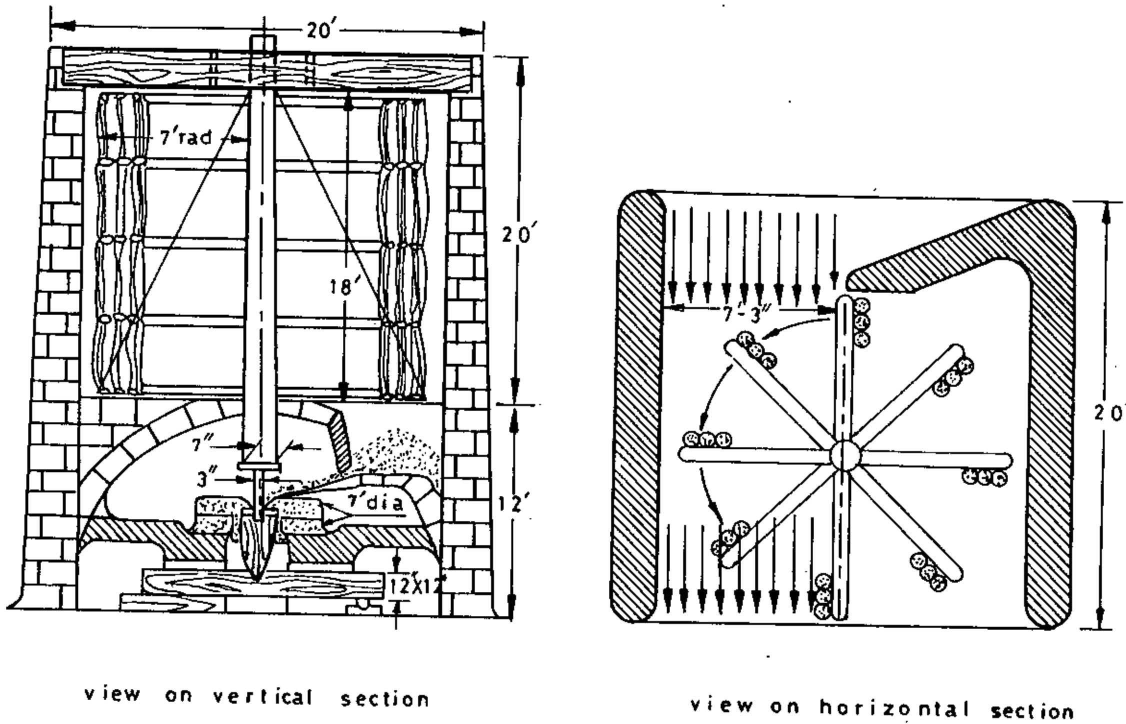

Figure 2.1: Persian winmill of Vertical axis type.

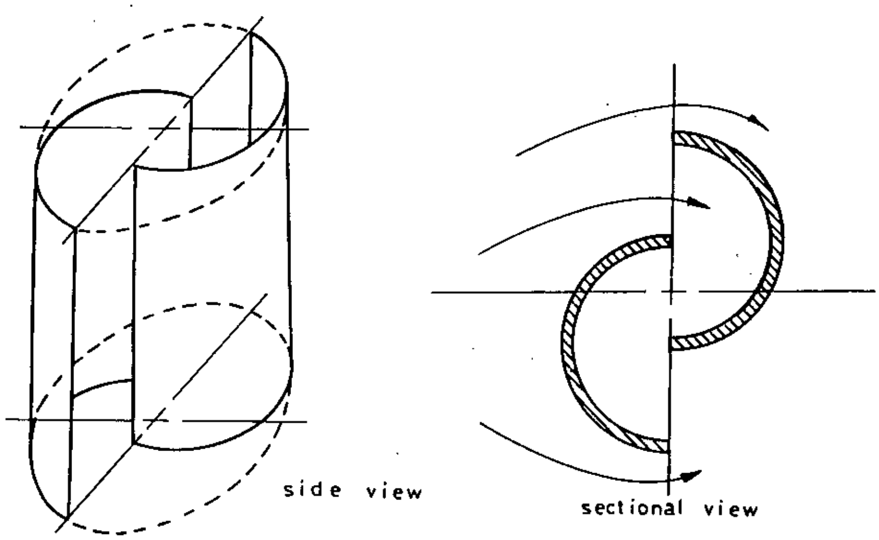

Figure 2.2: Savonius rotor

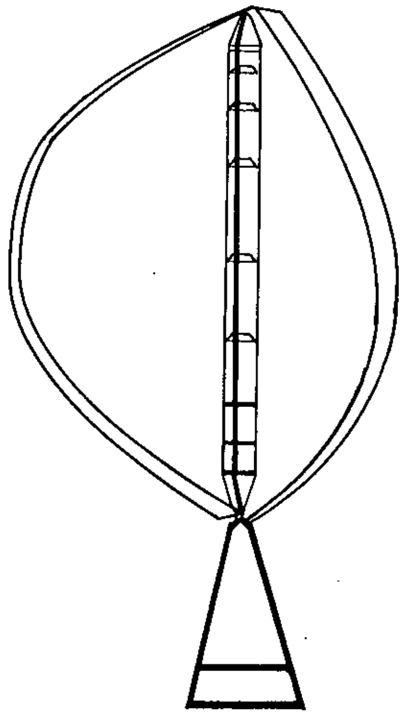

Figure 2.3 : Darrieus Turbine.

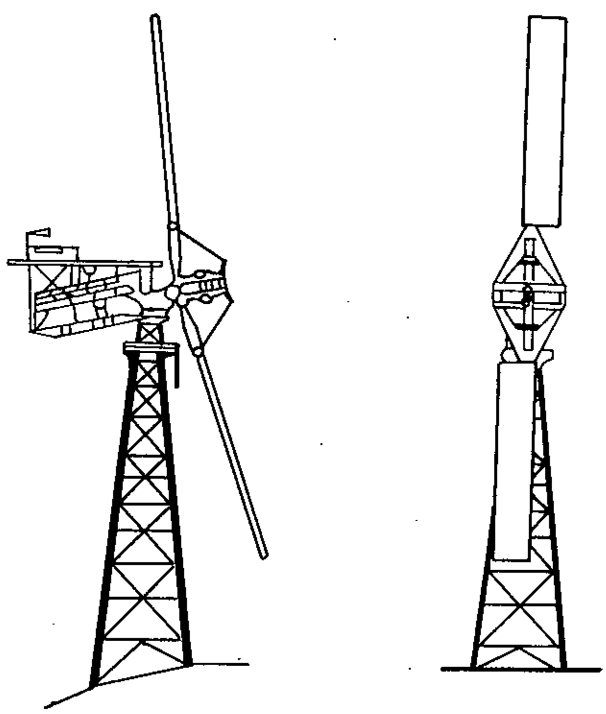

Figure 2.4 : Smith-Putnam Wind Turbine

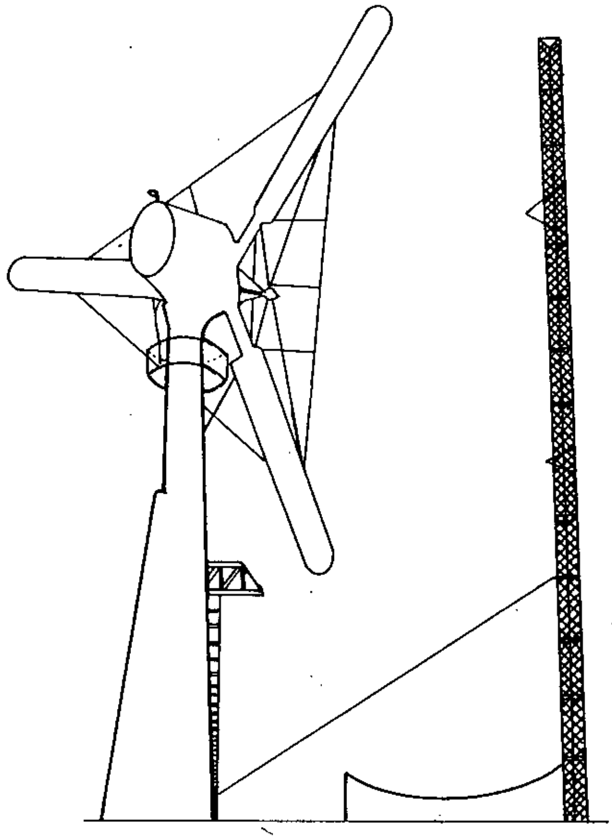

Figure 2.5: Restored Danish Gedser Wind Turbine.

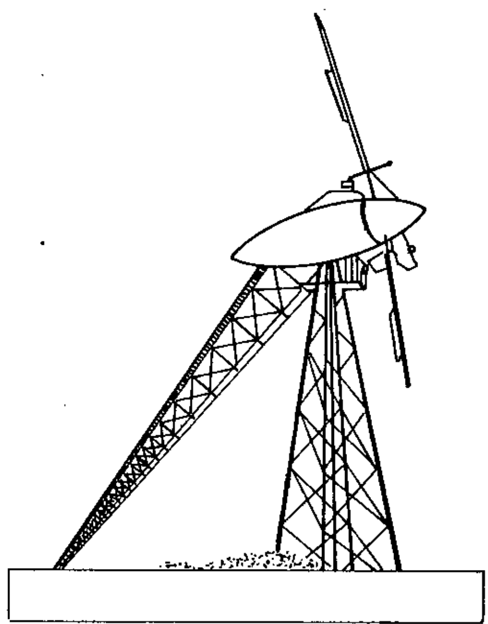

Figure 2.6: Russian Wind Turbine

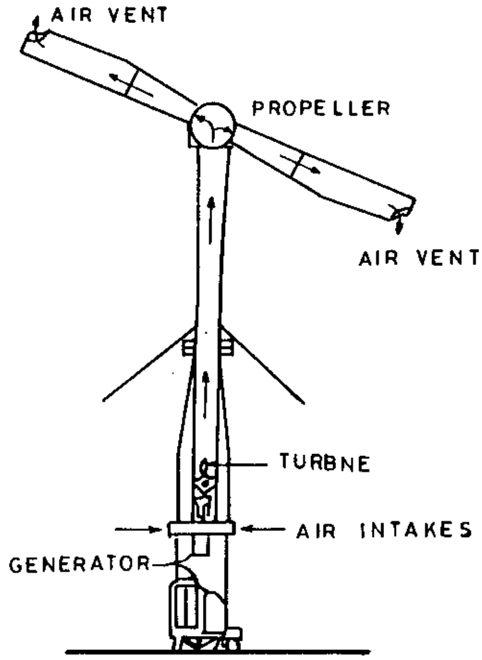

Figure 2.7 : Enfield Andreau Ducted Rotor.

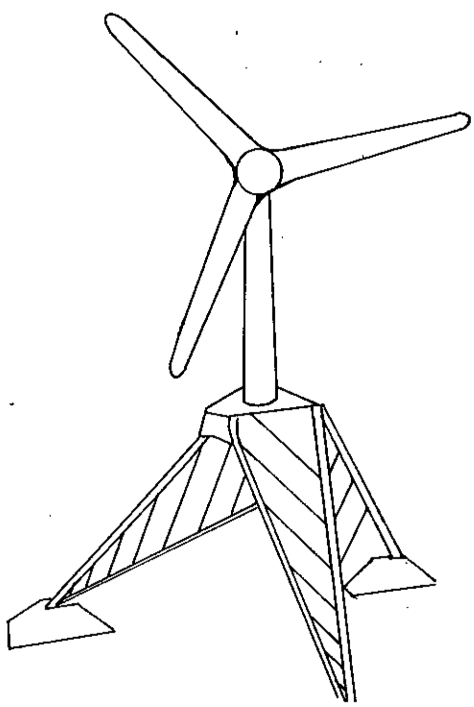

Figure 2.8 : French Wind Turbine Located Near Paris,France.

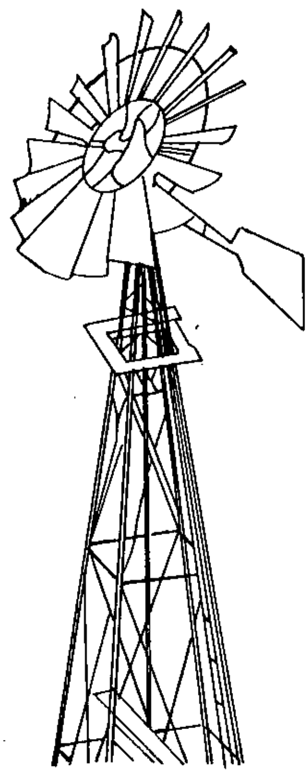

Figure 2.9: Horizontal axis wind turbine for pumping water.

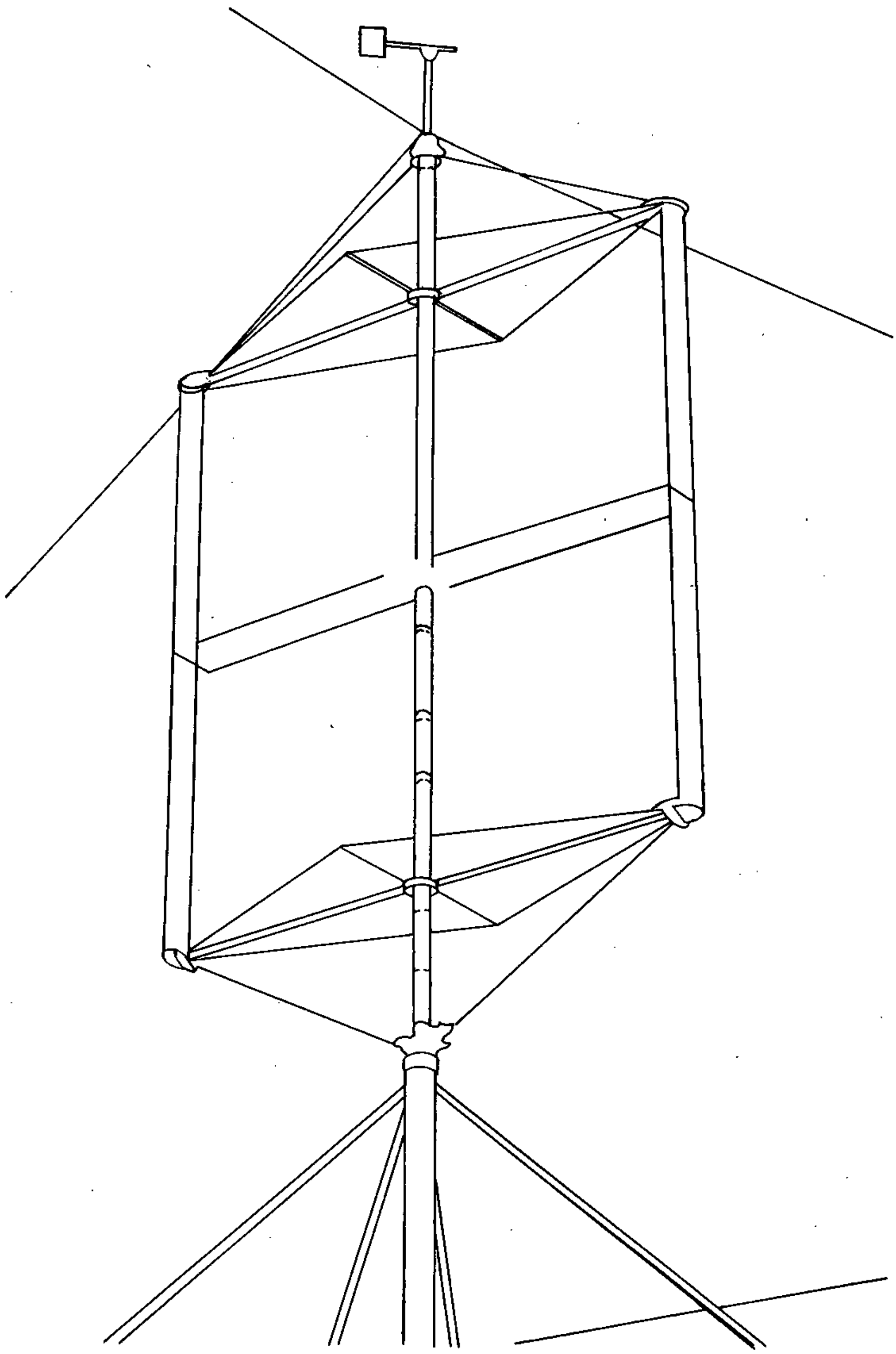

Figure 2.10: Straight bladed Darrieus wind turbine.

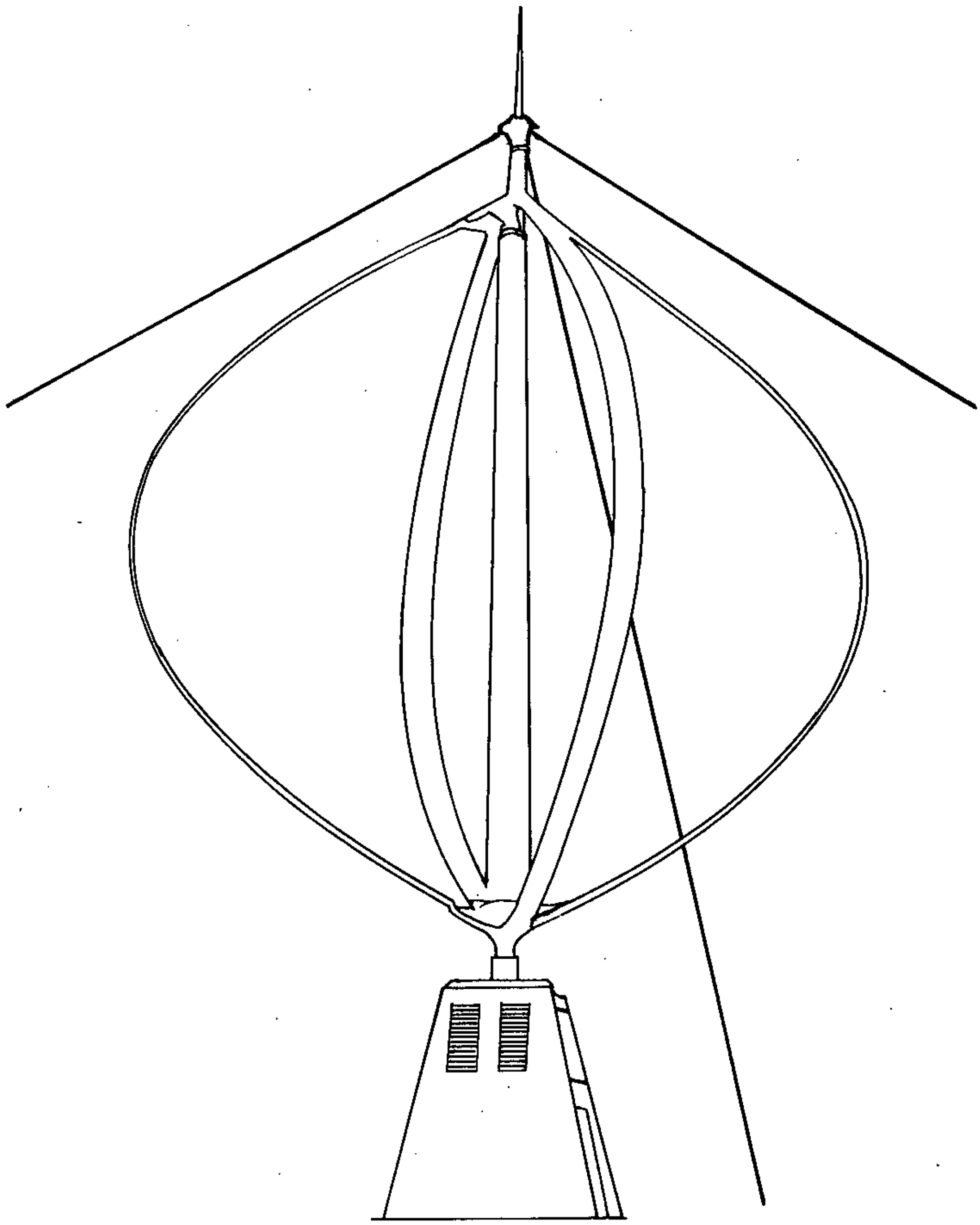

Figure 2.11 : Curved bladed Darrieus wind turbine.

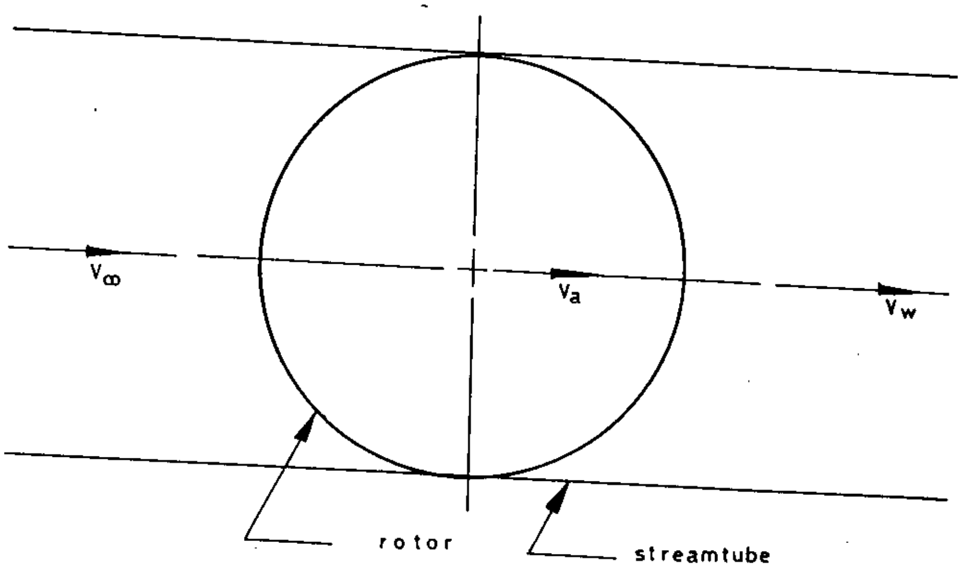

Figure 3.1 : Streamtube consisting of the rotor showing the axial flow velocities.

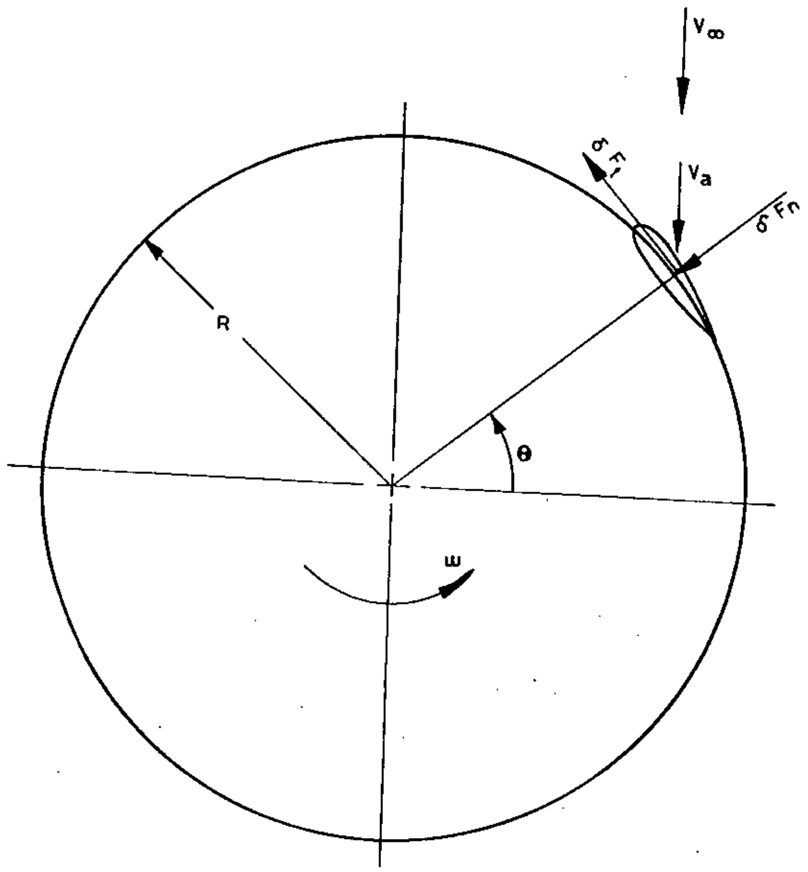

Figure 3.2 : Aerodynamic forces on a blade element of a Darrieus Rotor.

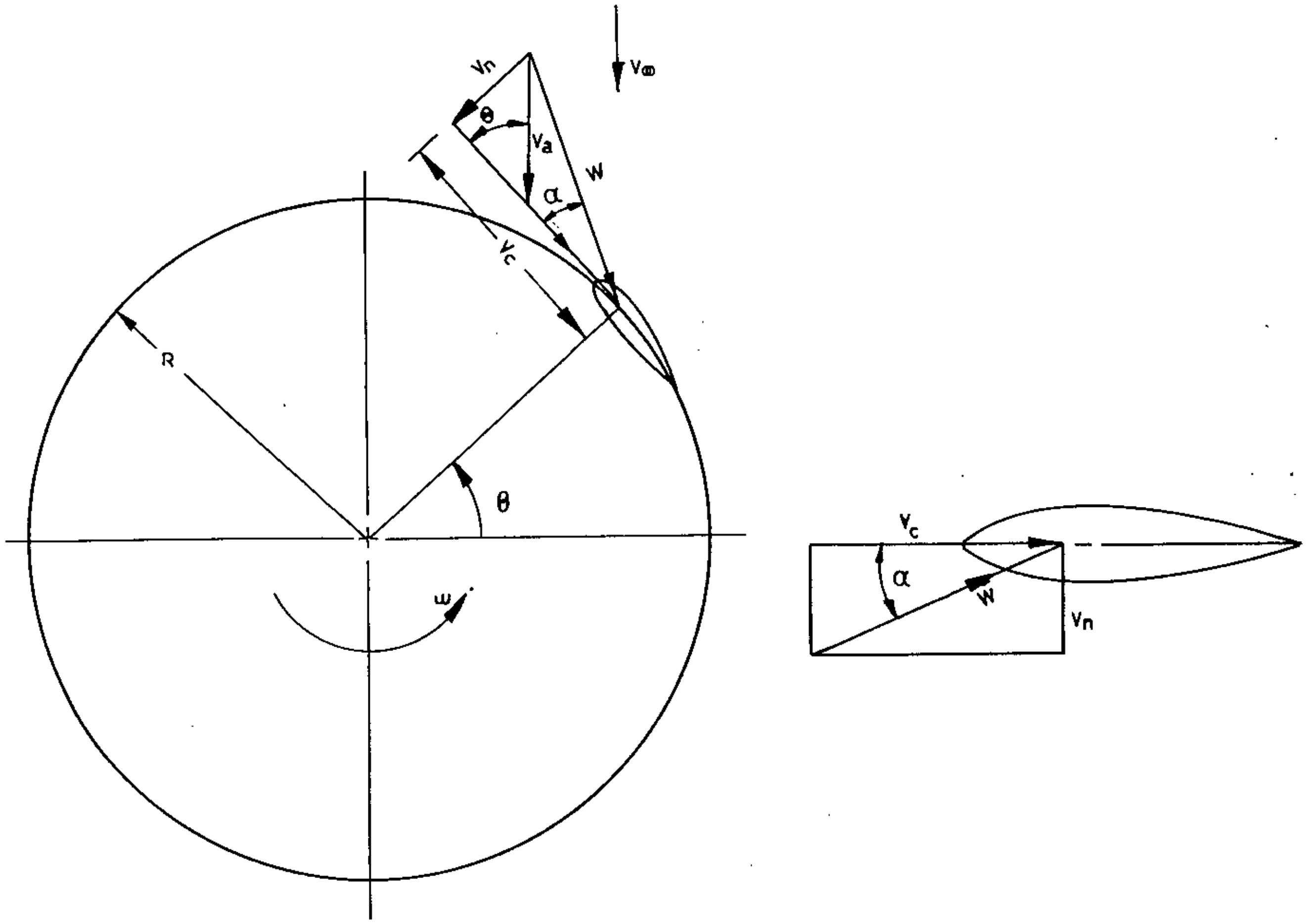

Figure 3.3 : Velocity diagram on the blade element of a straight-bladed Darrieus wind turbine.

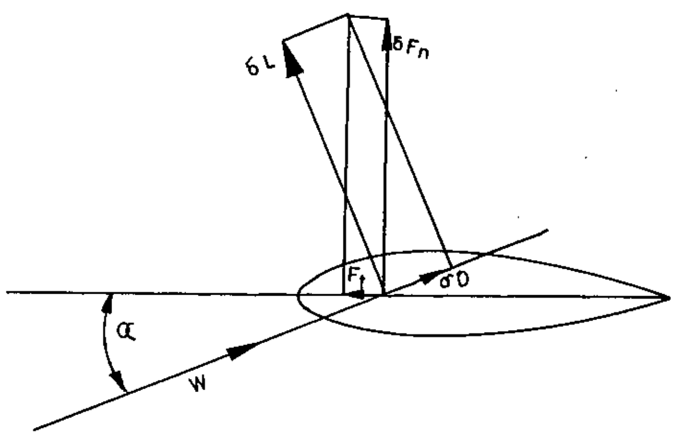

Figure 3.4 : Aerodynamic forces acting on an airfoil.

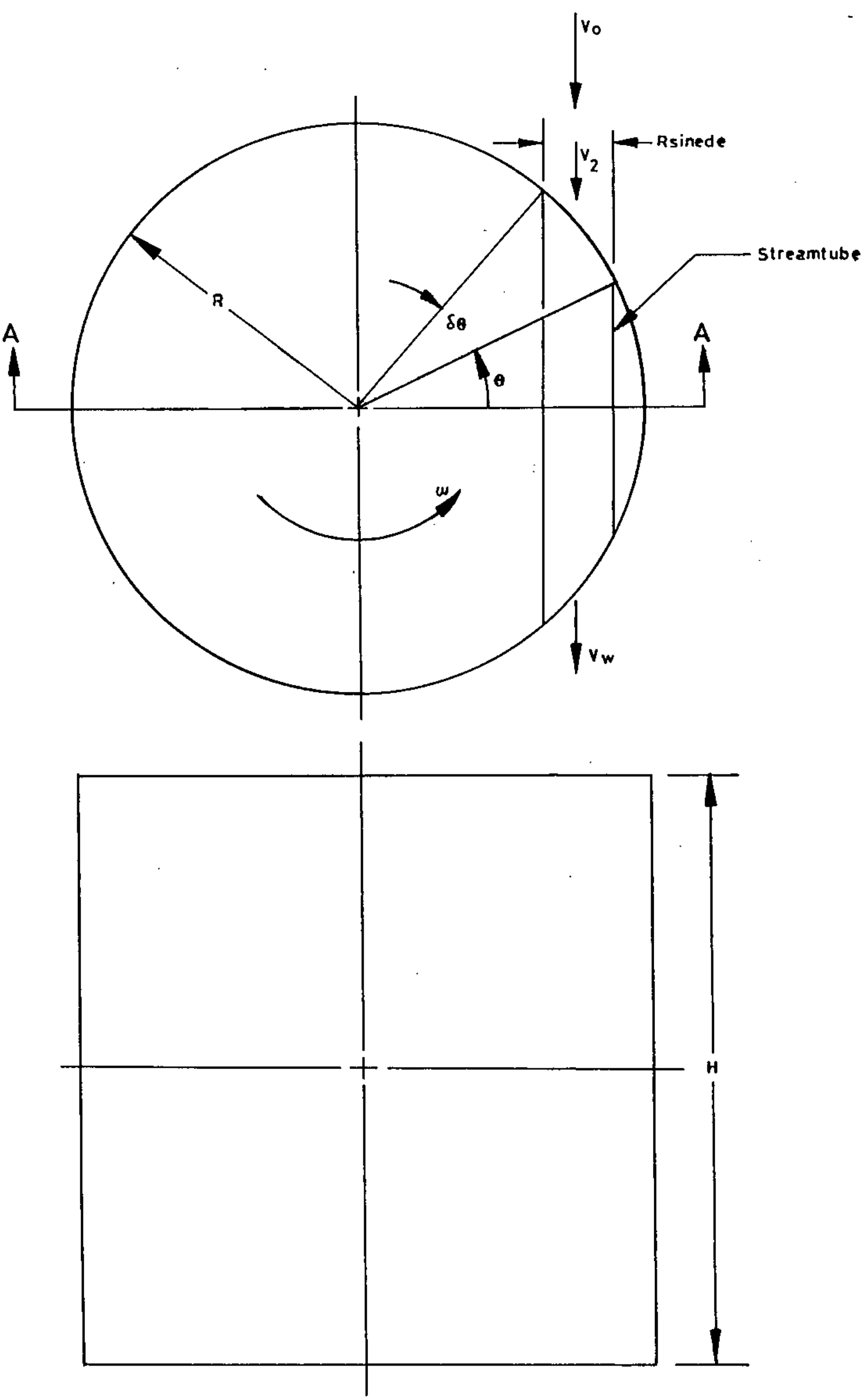

View on section A-A

Figure 3.5 : Cross-sectional area of an elemental streamtube of a straight-bladed Darrieus wind turbine.

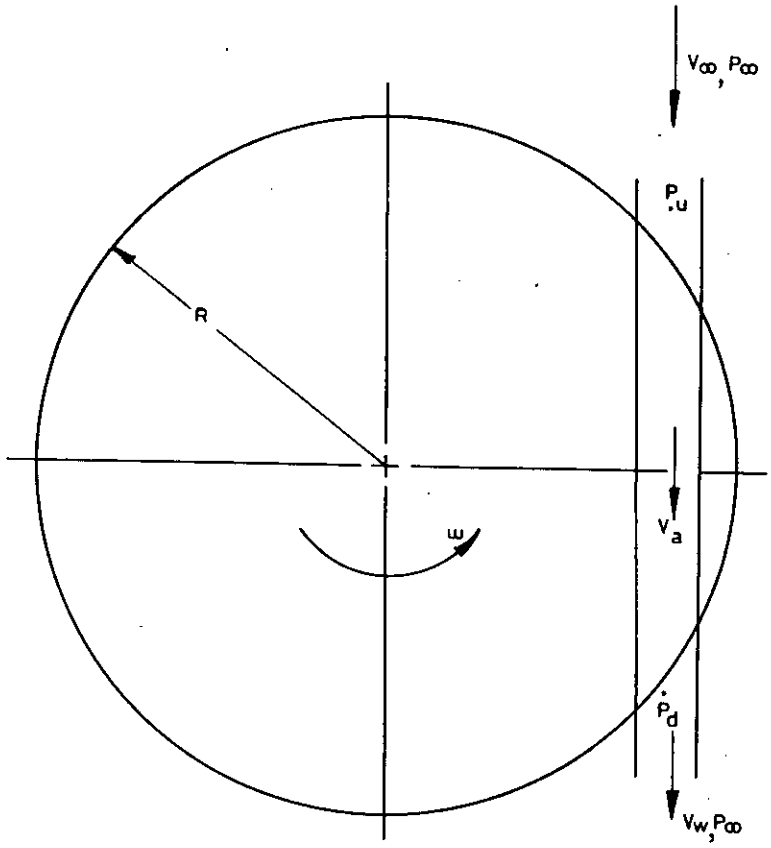

Figure 3.6: Pressures and velocities along the streamtube.

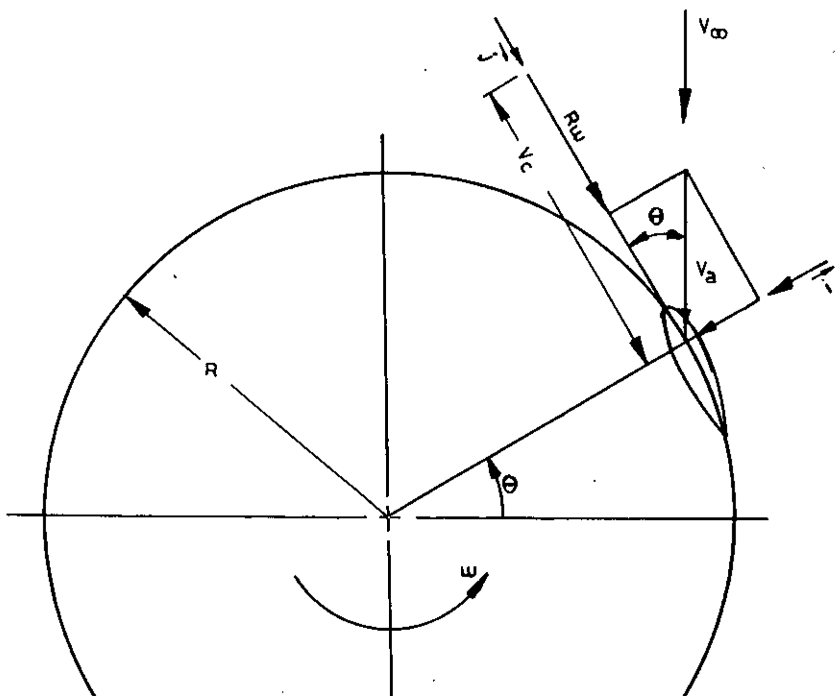

Figure 3.7: Velocity diagram on the blade element of a straight-bladed Darrieus wind turbin.

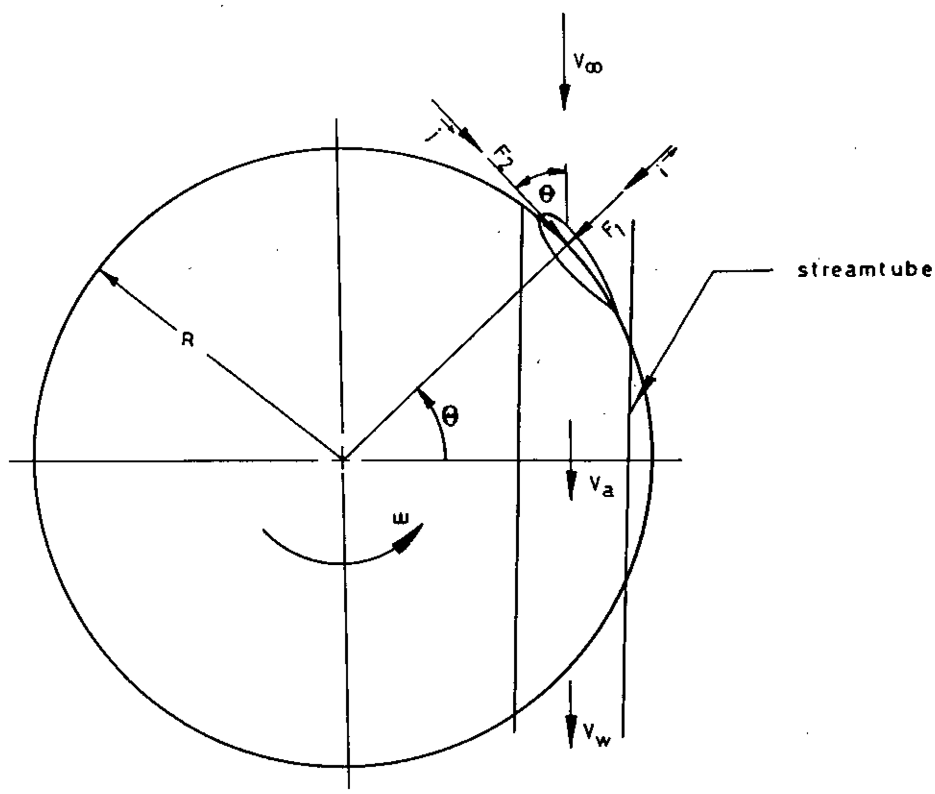

Figure 3.8: Force diagram on the blade element of a straight-bladed Darrieus wind turbine.

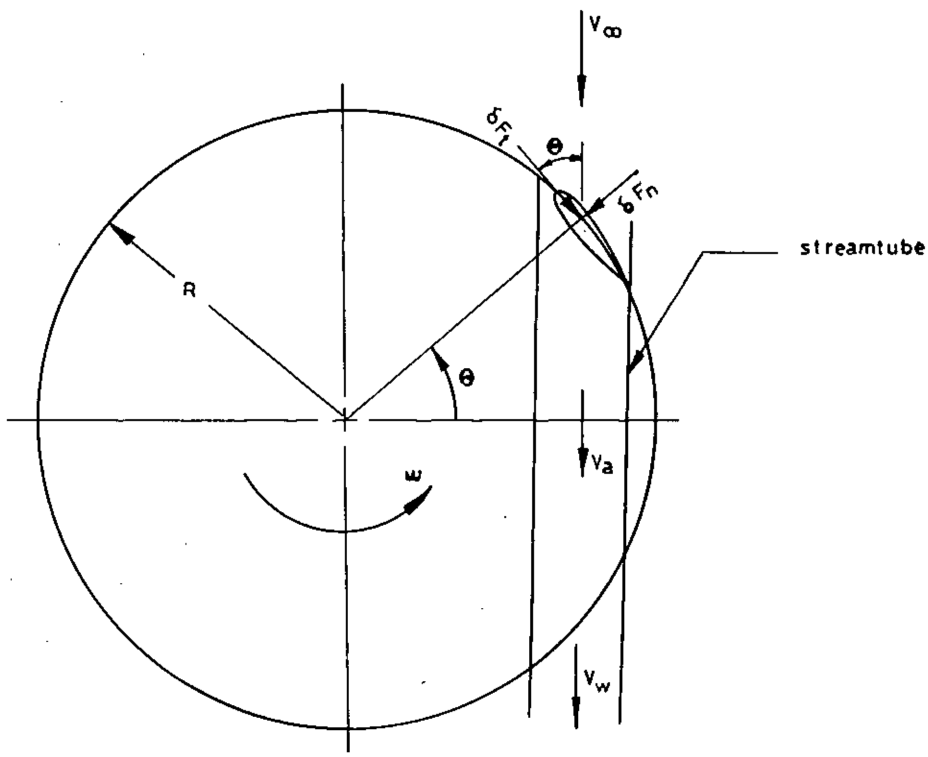

Figure 3.9: Elemental blade forces of a straight blade Darrieus rotor.

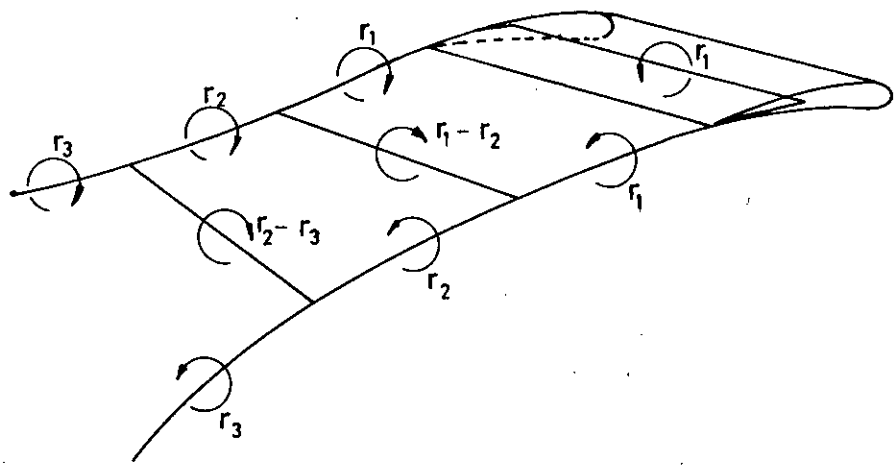

Figure 3.10 : Vortex system for a single blade element.

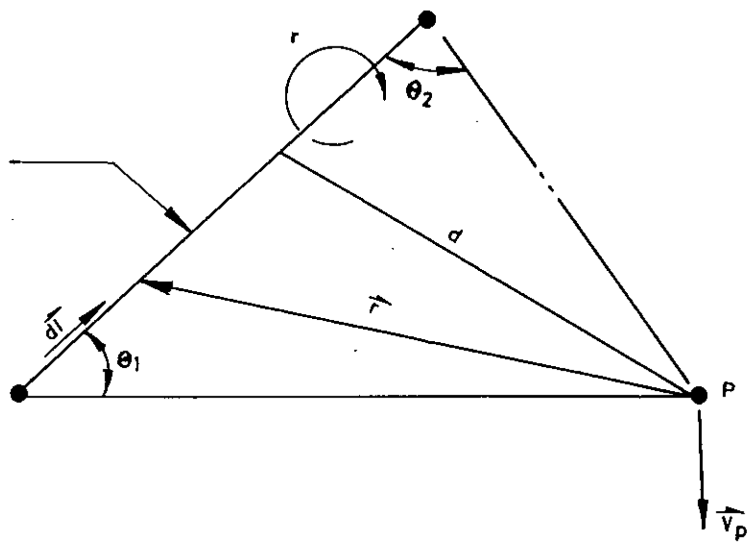

Figure 3.11 : Velocity induced at a point by vortex filament.

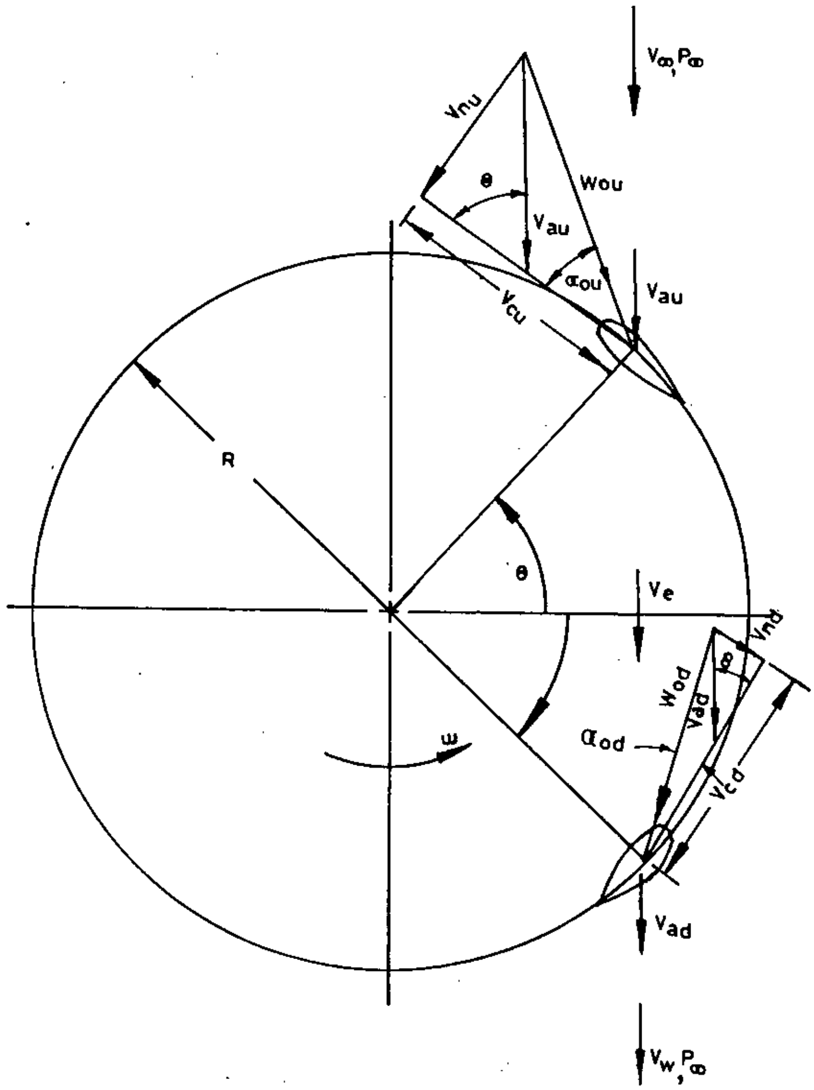

Figure. 4.1 : Horizontal section of a straight – bladed Darrieus wind turbine with flow velocities.

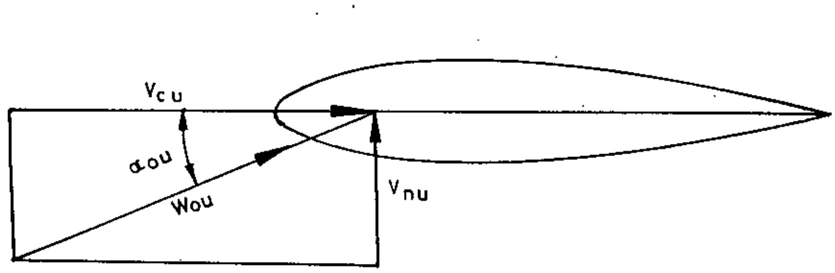

Figure 4.2 : Relative flow velocities on a blade airfoil.

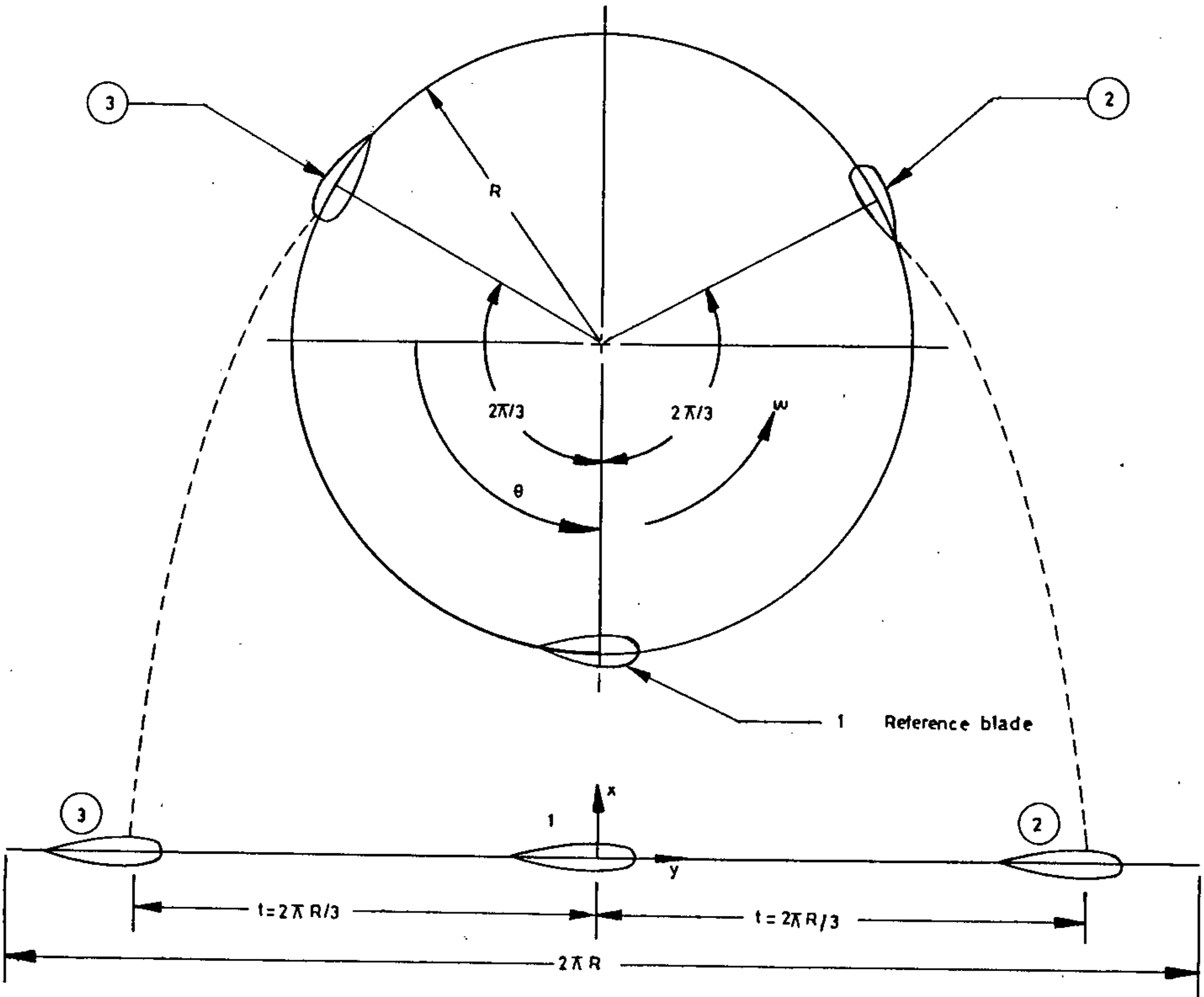

Figure 4.3 : Development of blade elements into cascade configuration.

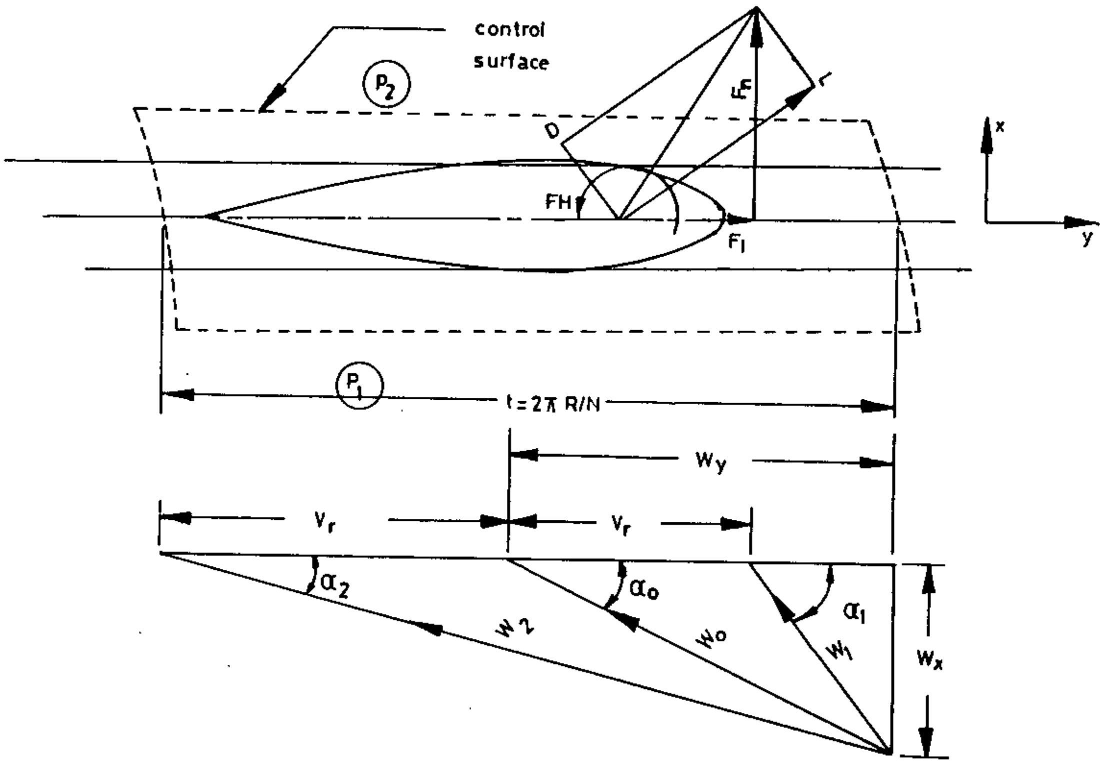

Figure 4.4 : Velocity diagram on the blade section.

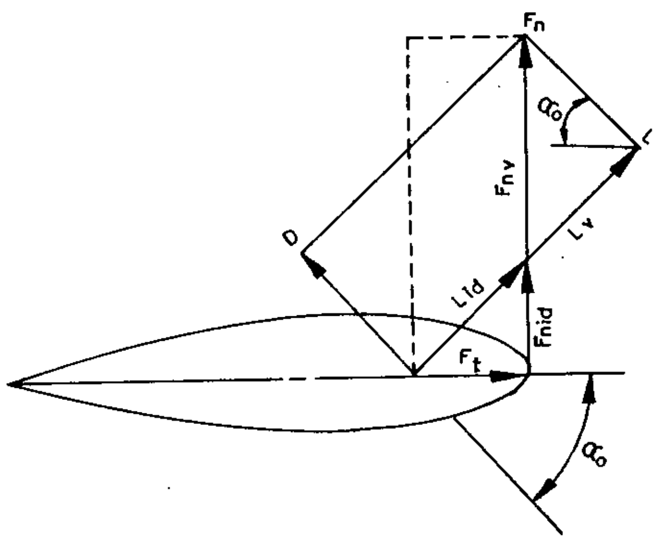

Figure 4.5 : Force diagram on the blade section.

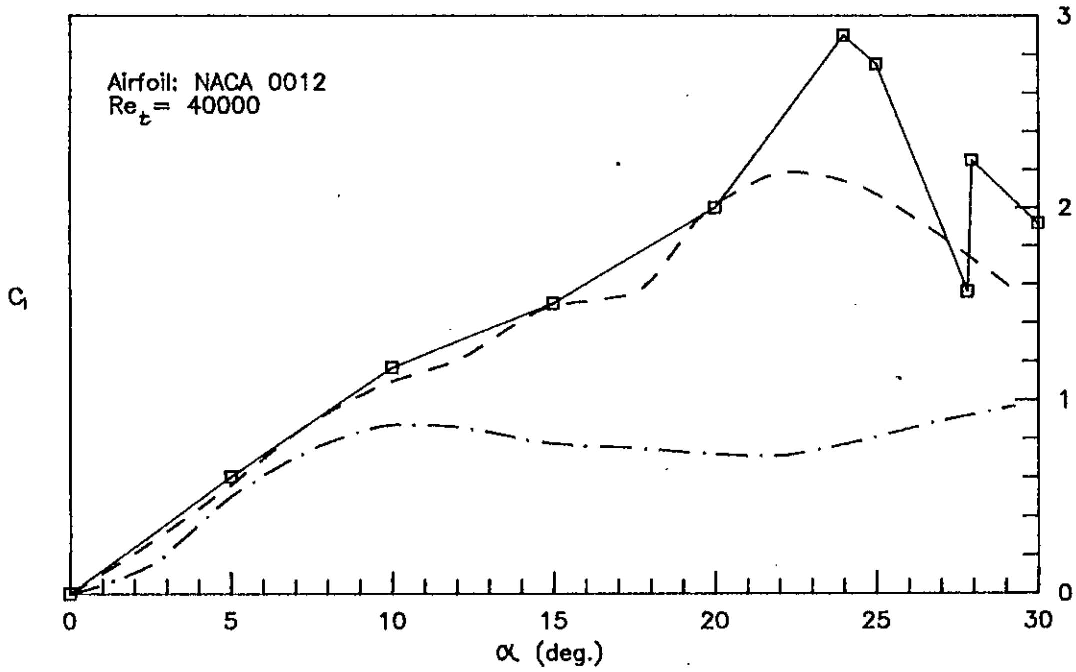

Figure 5.1: Comparisons of the Airfoil Lift Characteristics

—·—·— static lift
– – – – – dynamic lift
–□–□–□– experimental lift

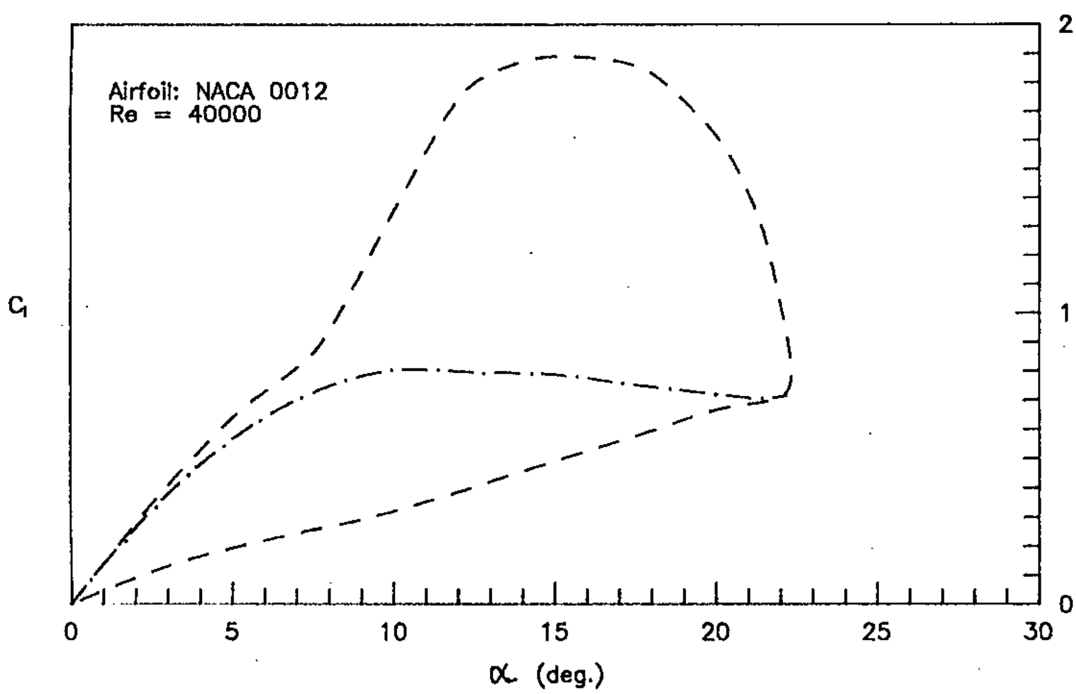

Figure 5.2: Variation of Lift Characteristics for Static and dynamic stall Condition.

—·—·— static lift – – – dynamic lift (present)

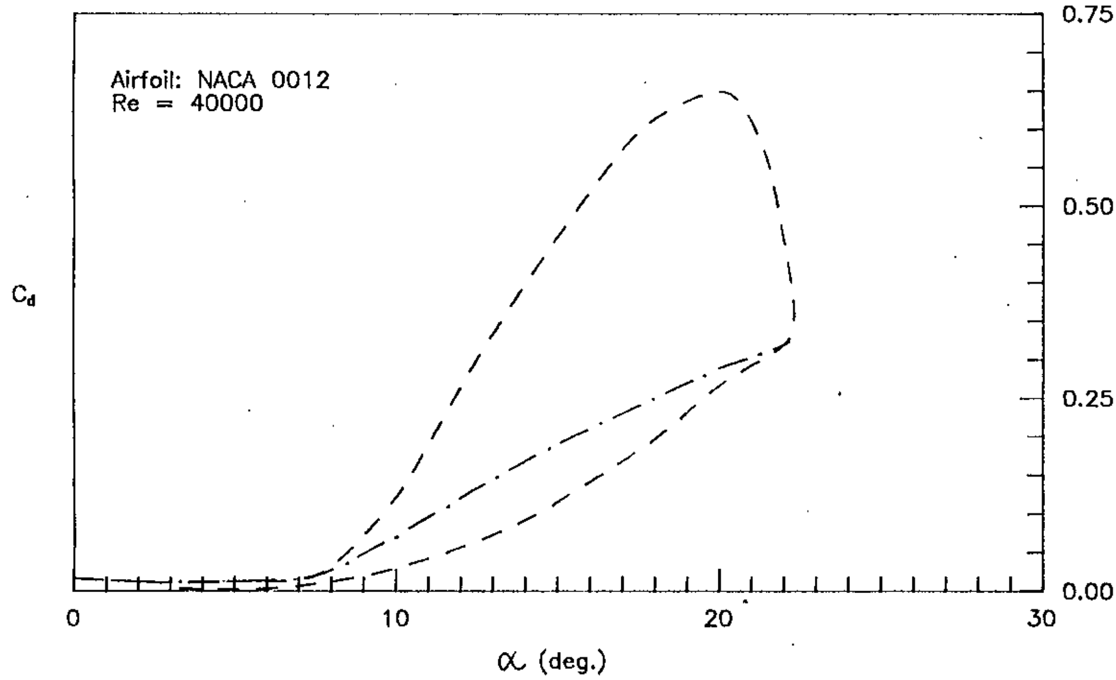

Figure 5.3: Variation of Drag Characteristics for Static and dynamic stall Condition.

—·—·— static drag   – – – dynamic drag (present)

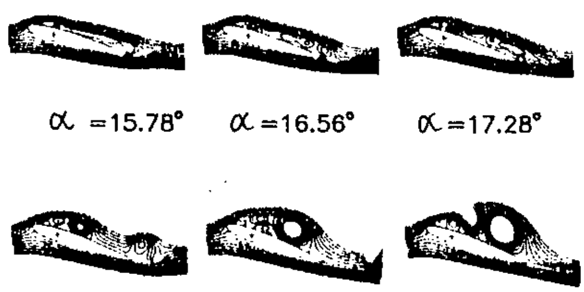

α =15.78° α =16.56° α =17.28°

α =18.97° α =19.99° α =19.44°

Figure 5.4: Dynamic Stall Flow Characteristics.

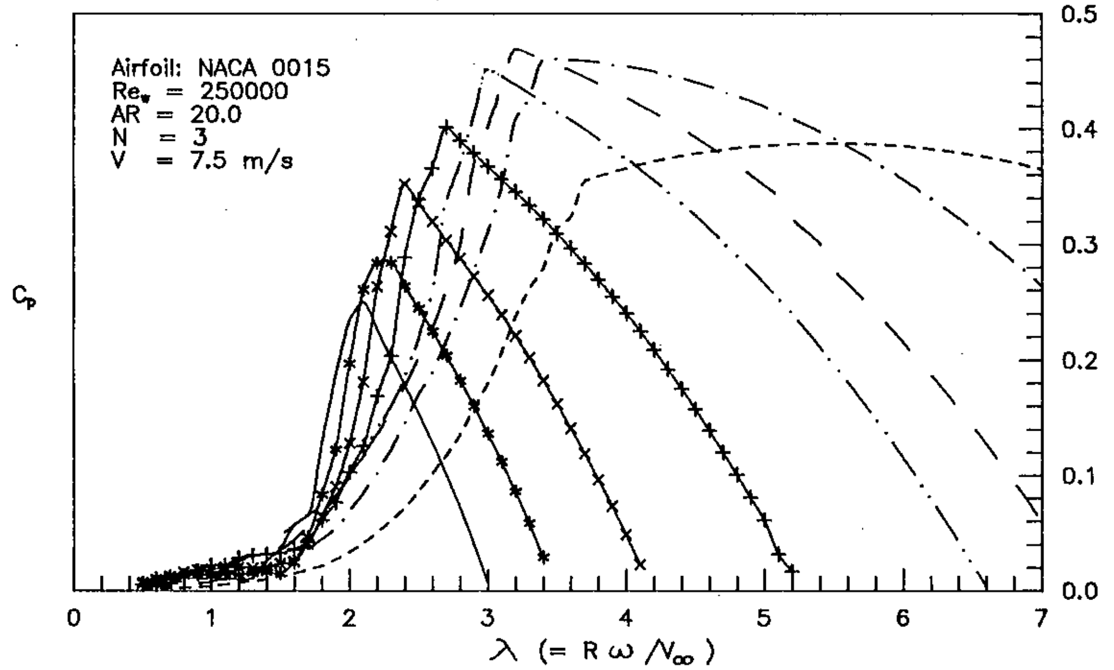

Figure 5.5: Overall Power coefficients vs. tip speed ratios at various solidities.

Symbol :	- - - -	–·–·–	— — —	–··–··–	+++	×××	✱✱✱	——
σ :	.10	.2	.3	.4	.6	.8	1.0	1.2

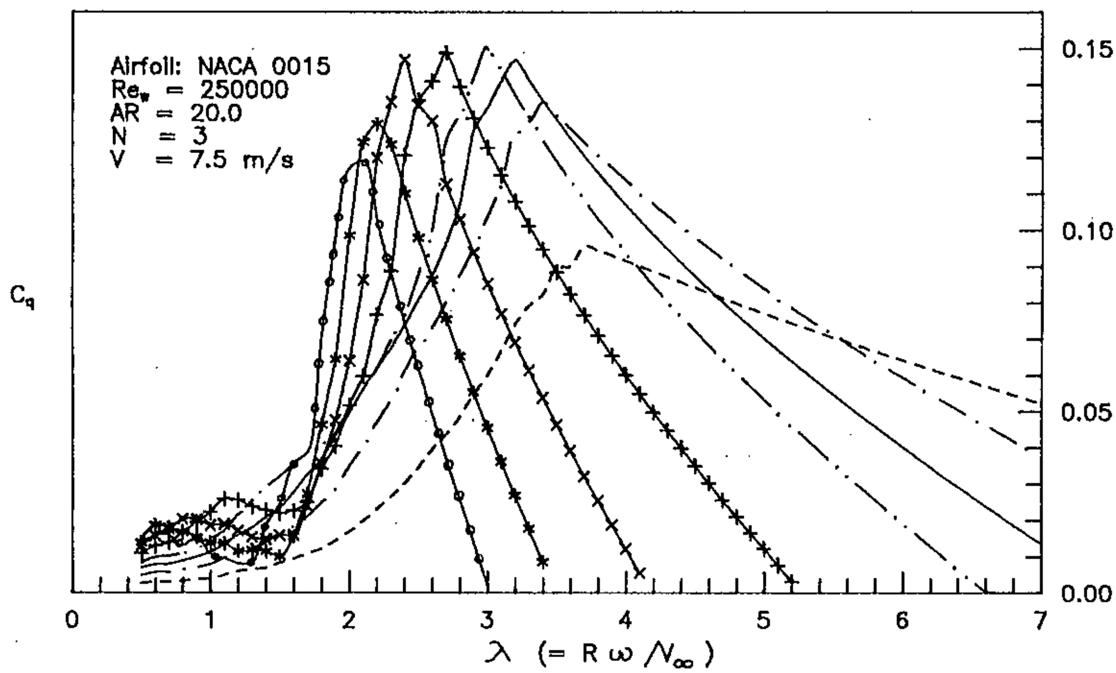

Figure 5.6: Overall Torque coefficients vs. tip speed ratios at various solidities.

Symbol :	- - - -	–·–·–	——	–··–··–	+++	×××	✱✱✱	-o-o-o-
σ :	.10	.2	.3	.4	.6	.8	1.0	1.2

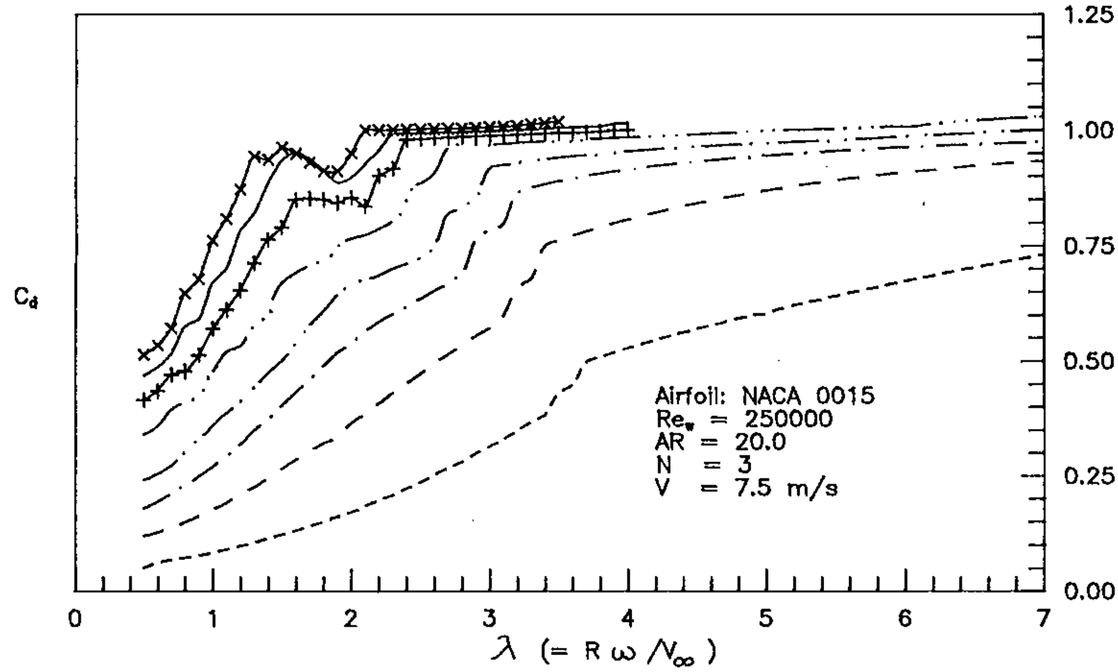

Figure 5.7 : Overall drag coefficients vs. tip speed ratios at various solidities.

Symbol :
σ : .10 .2 .3 .4 .6 .8 1.0 1.2

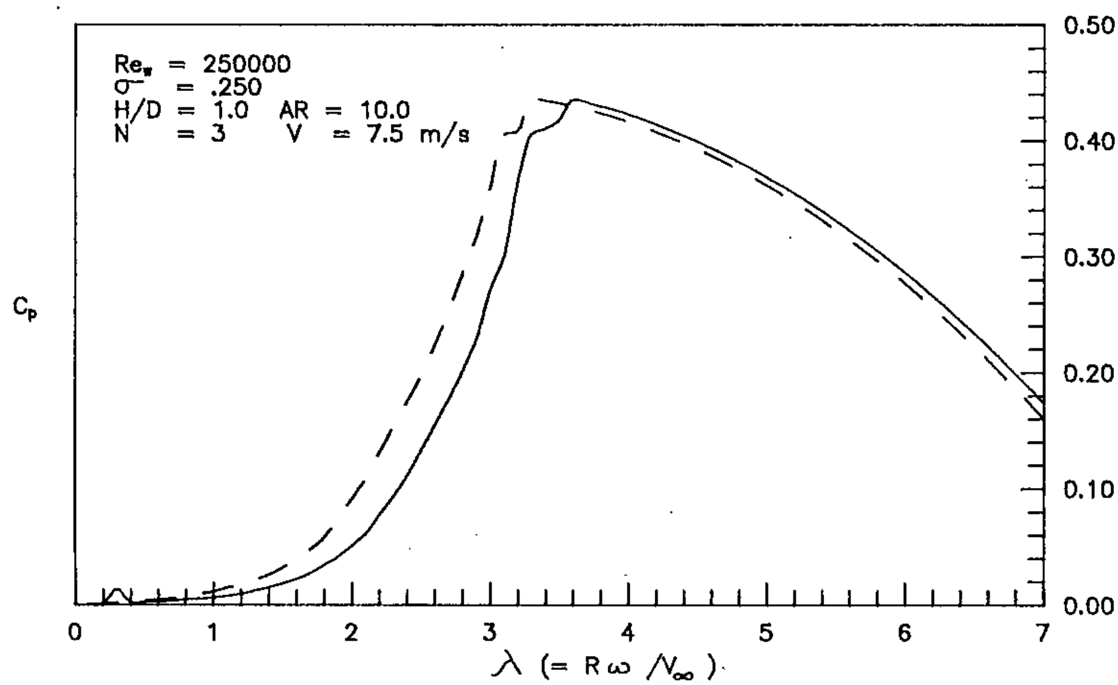

Figure 5.8: Comparisons of overall power coefficients for airfoils NACA 0012 and NACA 0015.

Symbol :
airfoil: NACA' 0012 NACA 0015

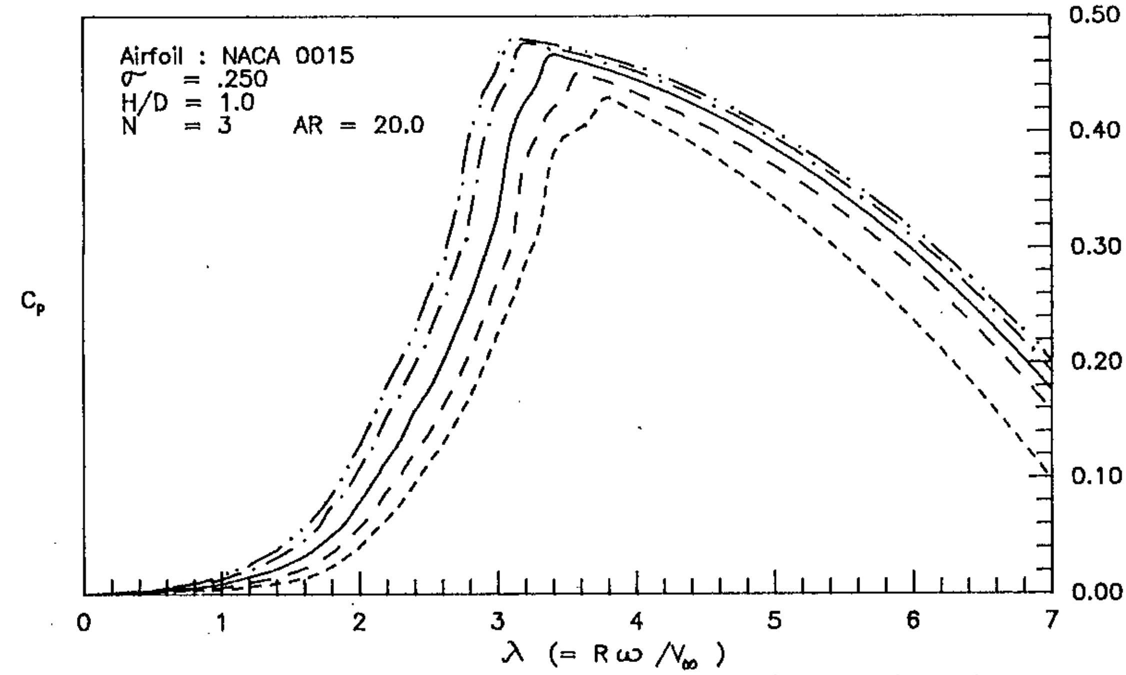

Figure 5.9 : Overall power coefficients vs. tip speed ratios at various wind speed Reynolds number.

Symbol : ----- — — — ——— —·—·· —··—··
Re_w : 50000 100000 200000 400000 600000

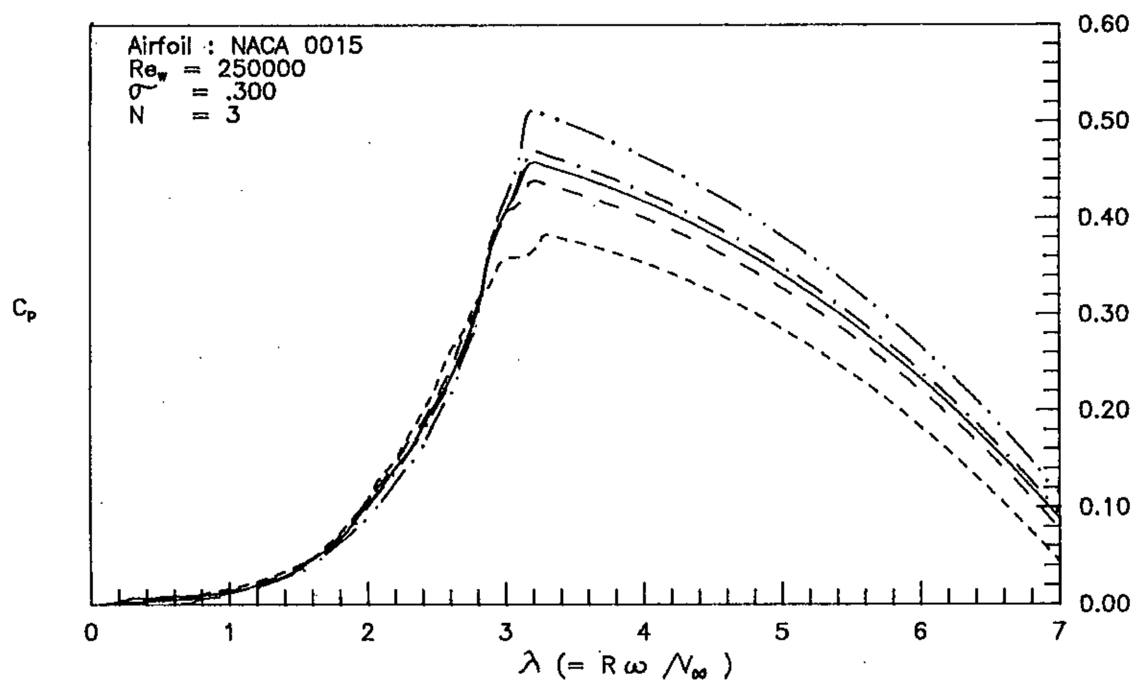

Figure 5.10 : Overall power coefficients vs. tip speed ratios at various aspect ratios.

Symbol : ----- — — — ——— —·—·— —··—··—
AR : 5 10 15 20 ∞

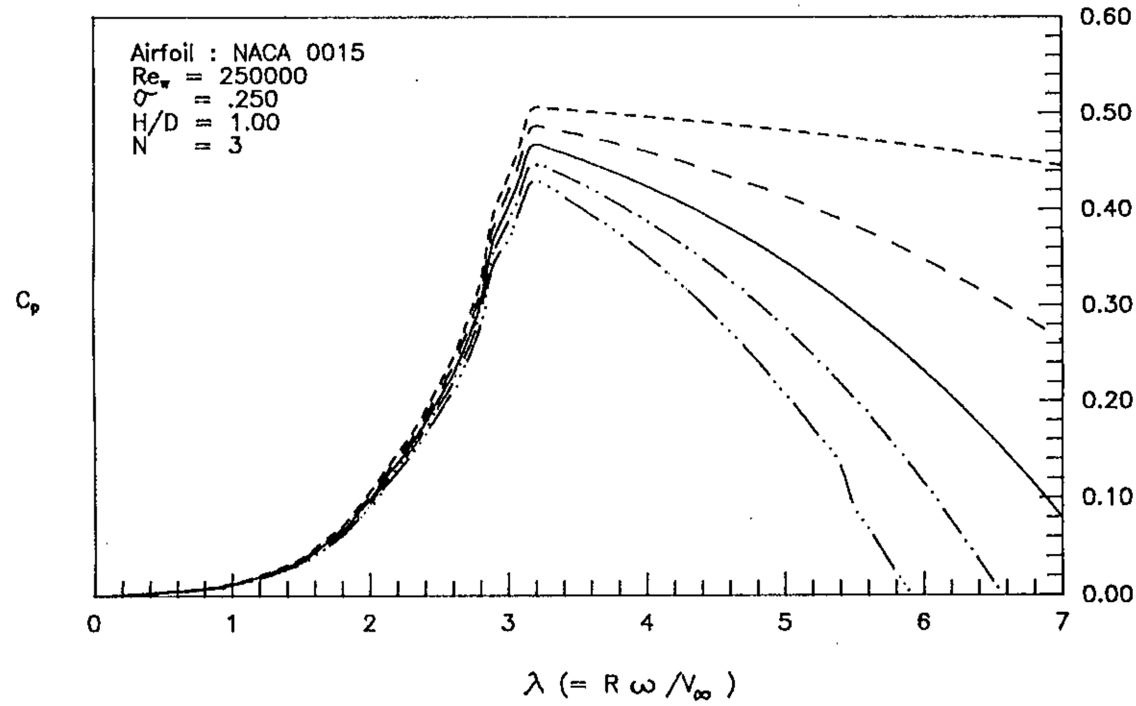

Figure 5.11 : Overall power coefficients vs. tip speed ratios at various zero-lift-drag coefficients.

Symbol : ---- — — — ——— —·— —··—
C_{do} : .000 .005 .010 .015 .020 (at Re = 250000)

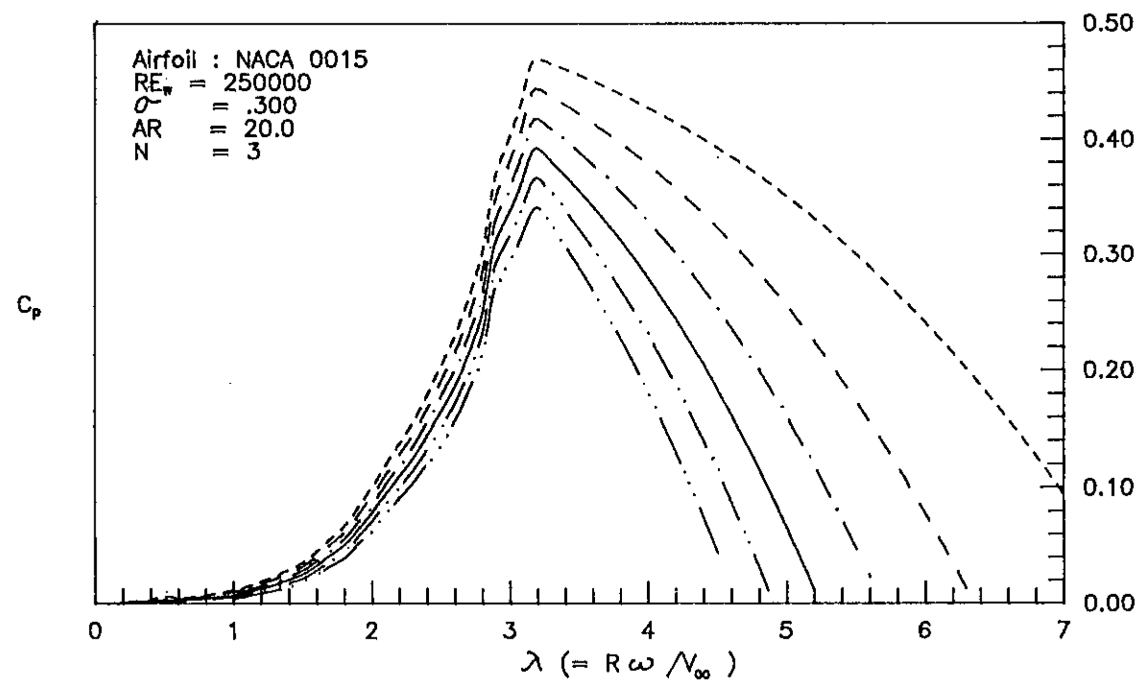

Figure 5.12 : Overall power coefficients vs. tip speed ratios at various strut drag coefficients.

Symbol : ---- — — — —·— ——— —··— —···—
C_{dst} : .00 .05 .10 .15 .20 .25

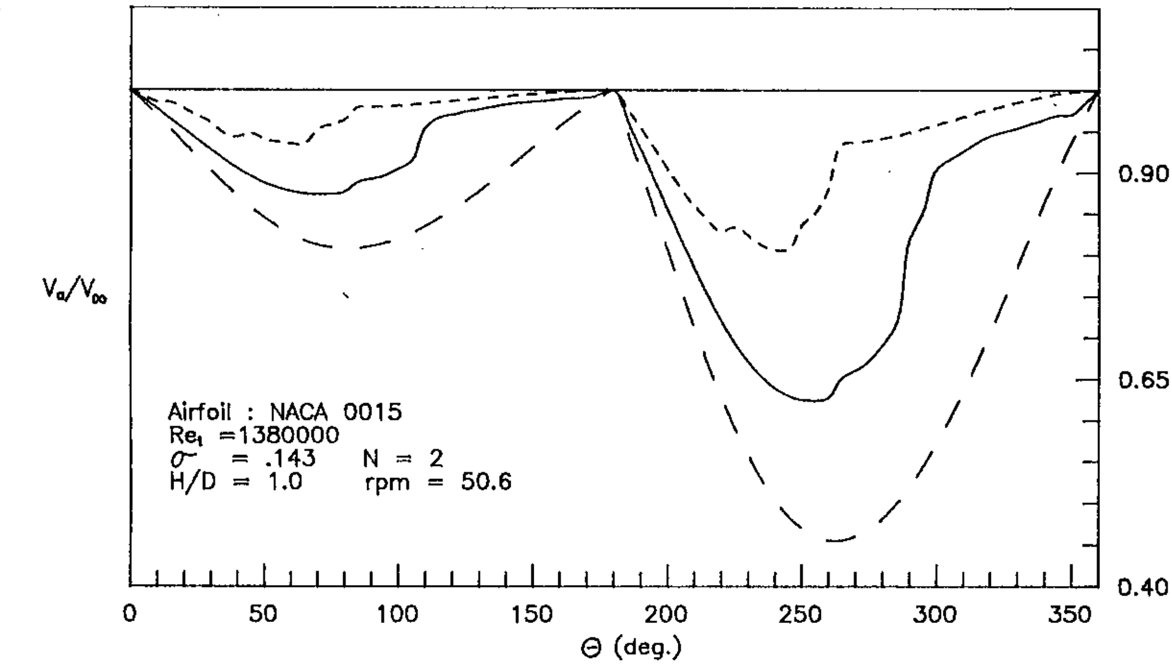

Figure 5.13 : Variations of induced veloocities with azimuth angle at different tip speed ratios.

Symbol :	----	——	— — —
λ :	1.50	3.00	4.50

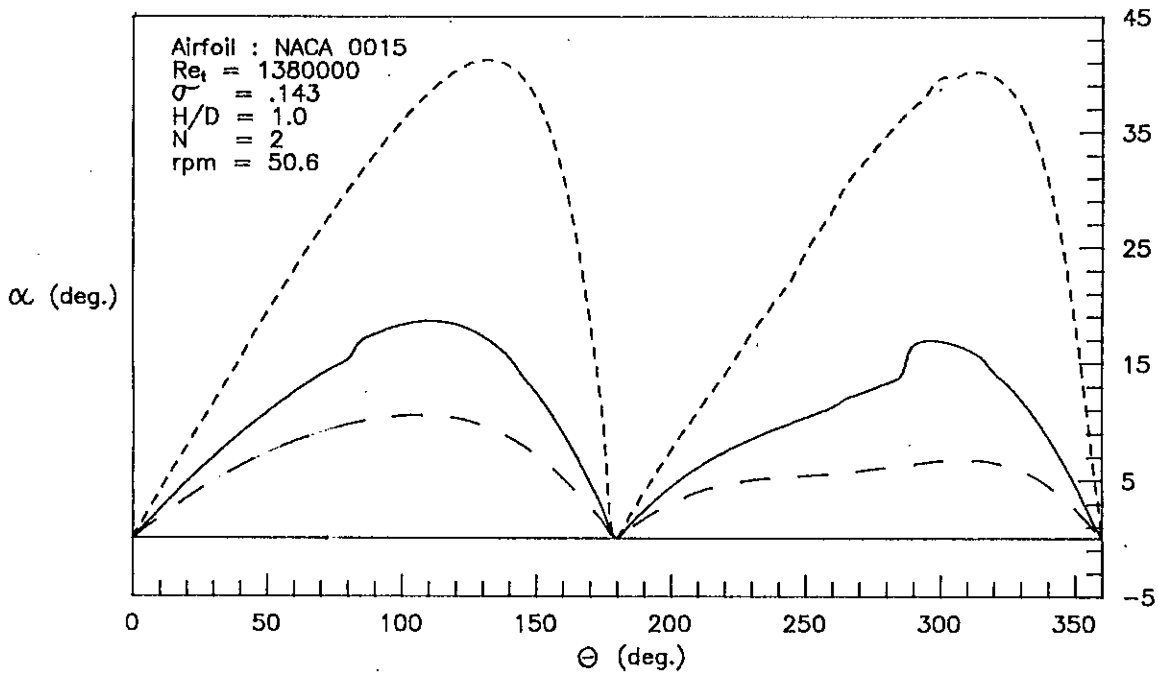

Figure 5.14 : Variations of loocal angles of attack with azimuth at different tip speed ratios.

Symbol :	----	——	— — —
λ :	1.50	3.00	4.50

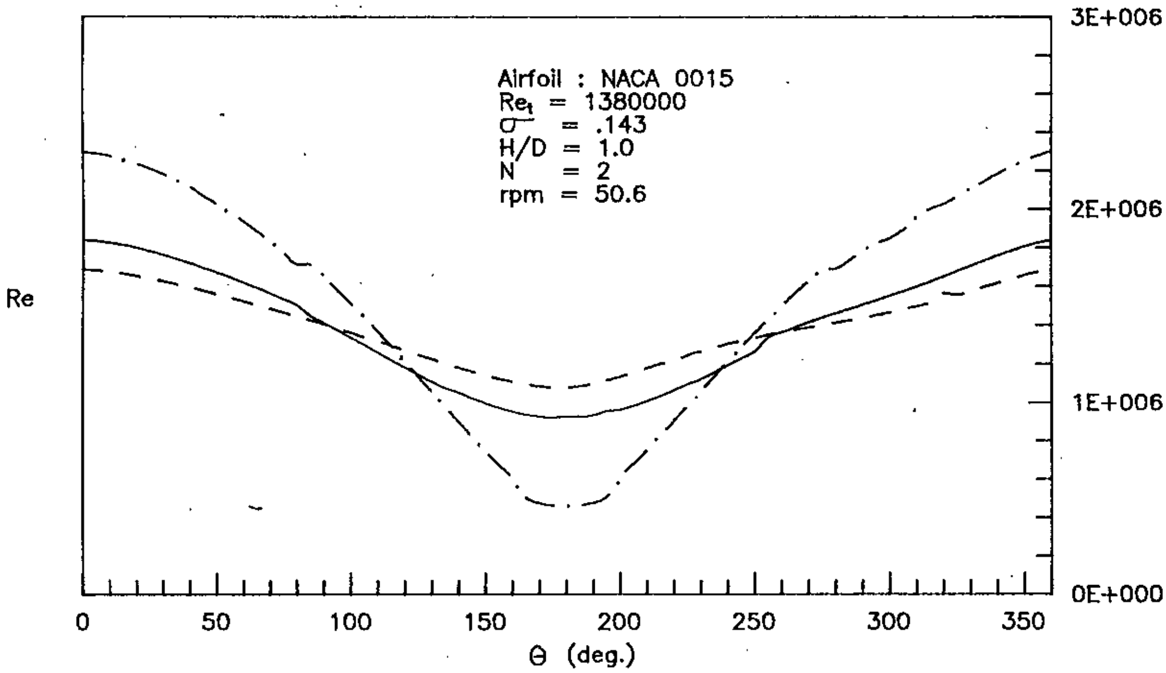

Figure 5.15 : Variations of local Reynolds number with azimuth at different tip speed ratios.

Symbol :	—·—·—	———	— — —
λ :	1.50	3.00	4.50

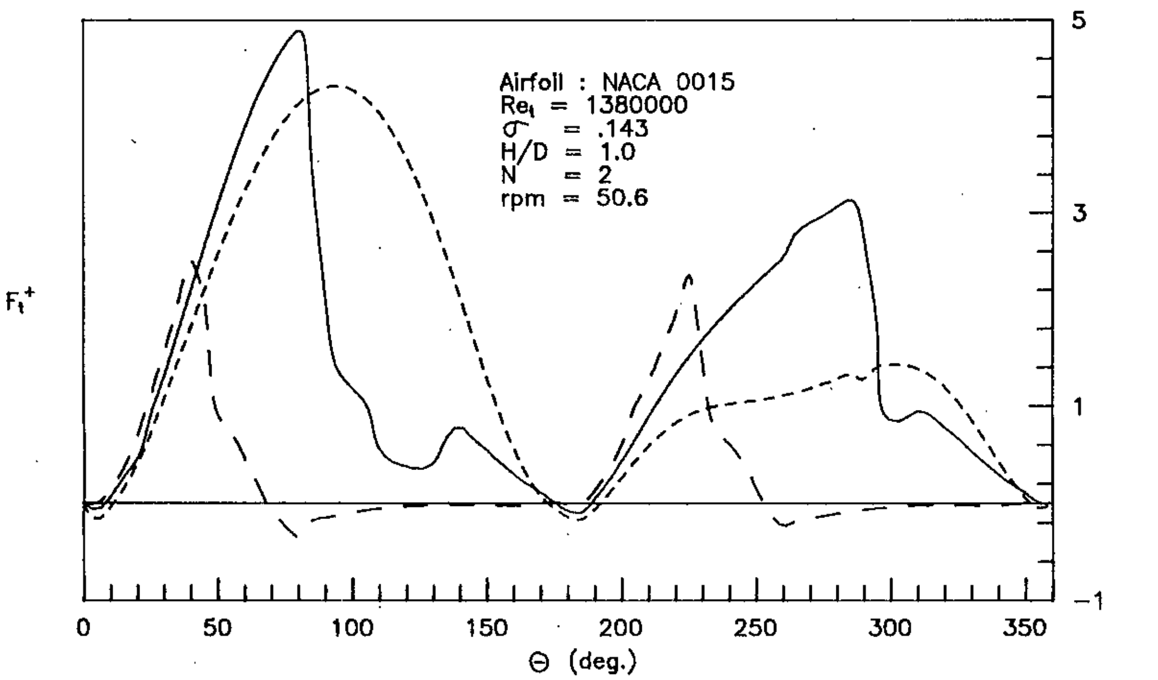

Figure 5.16 : Variations of local non–dimensional tangential forces with azimuth at different tip speed ratios.

Symbol :	— — —	———	- - - - -
λ :	1.50	3.00	4.50

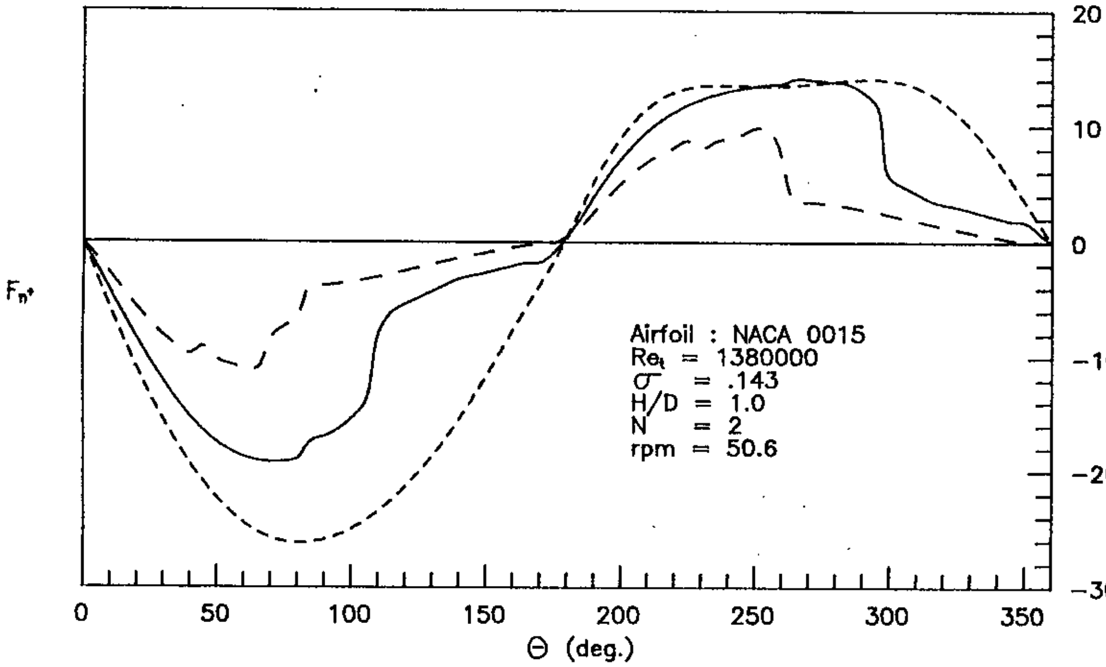

Figure 5.17: Variations of local non-dimensional normal forces with azimuth at different tip speed ratios.

Symbol : — — — ——— - - - - -
λ : 1.50 3.00 4.50

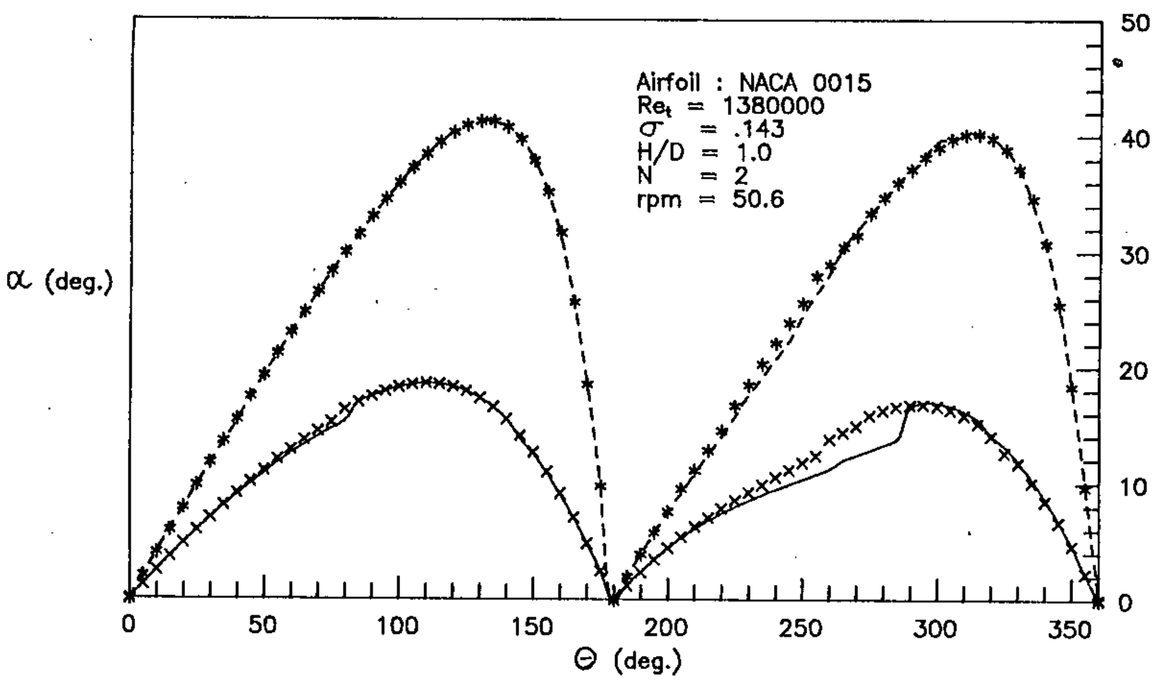

Figure 5.18: Comparisons of angle of attack calculated with and without dynamic stall.

* * * calc.(without dynamic stall at λ = 1.5)
× × × calc.(without dynamic stall at λ = 3.0)
- - - - calc.(with dynamic stall at λ = 1.5)
——— calc.(with dynamic stall at λ = 3.0)

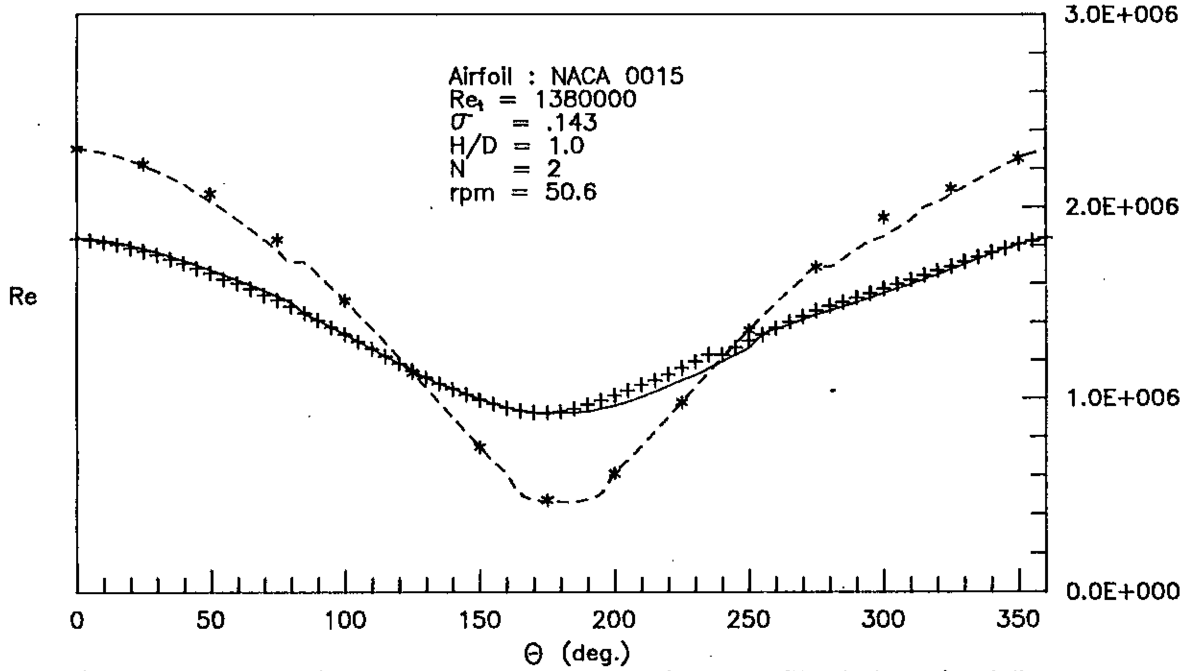

Figure 5.19: Comparisons of Reynolds number with and without dynamic stall.

* * * calc. (without dynamic stall at λ = 1.5)
+ + + calc. (without dynamic stall at λ = 3.0)
- - - - calc. (with dynamic stall at λ = 1.5)
——— calc. (with dynamic stall at λ = 3.0)

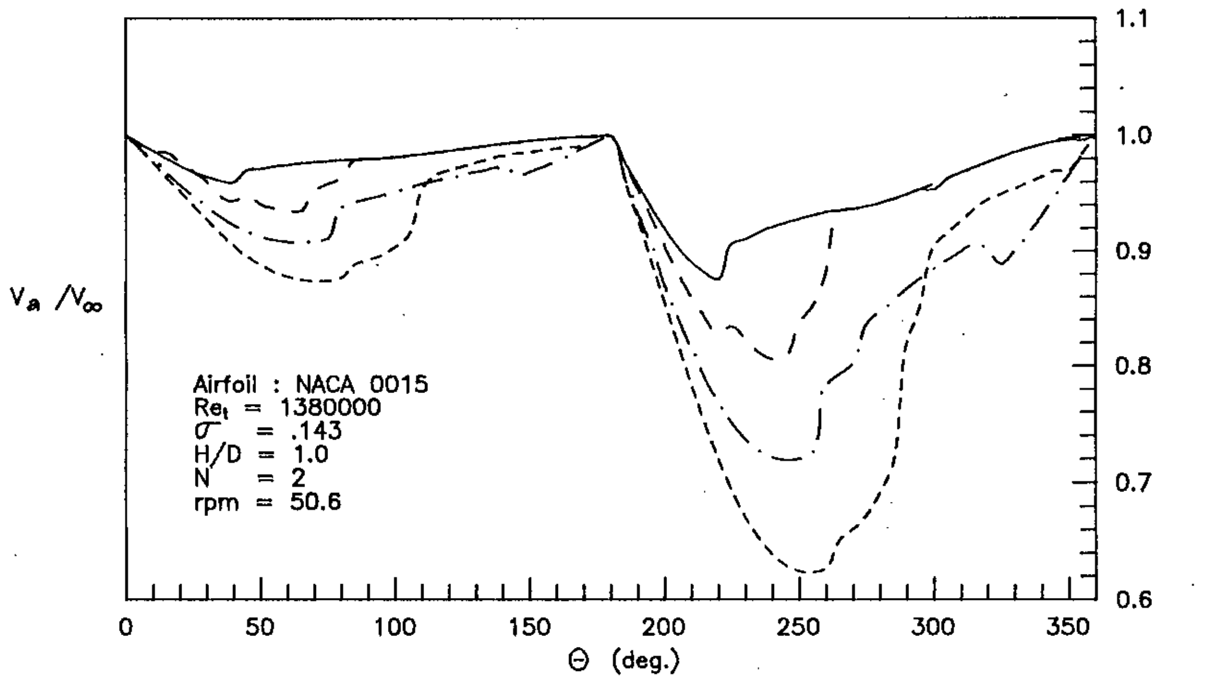

Figure 5.20 : Comparisons of induced velocity ratios with and without dynamic stall.

——— calc. (without dynamic stall at λ = 1.5)
—·— calc. (without dynamic stall at λ = 3.0)
— — — calc. (with dynamic stall at λ = 1.5)
- - - - - - calc. (with dynamic stall at λ = 3.0)

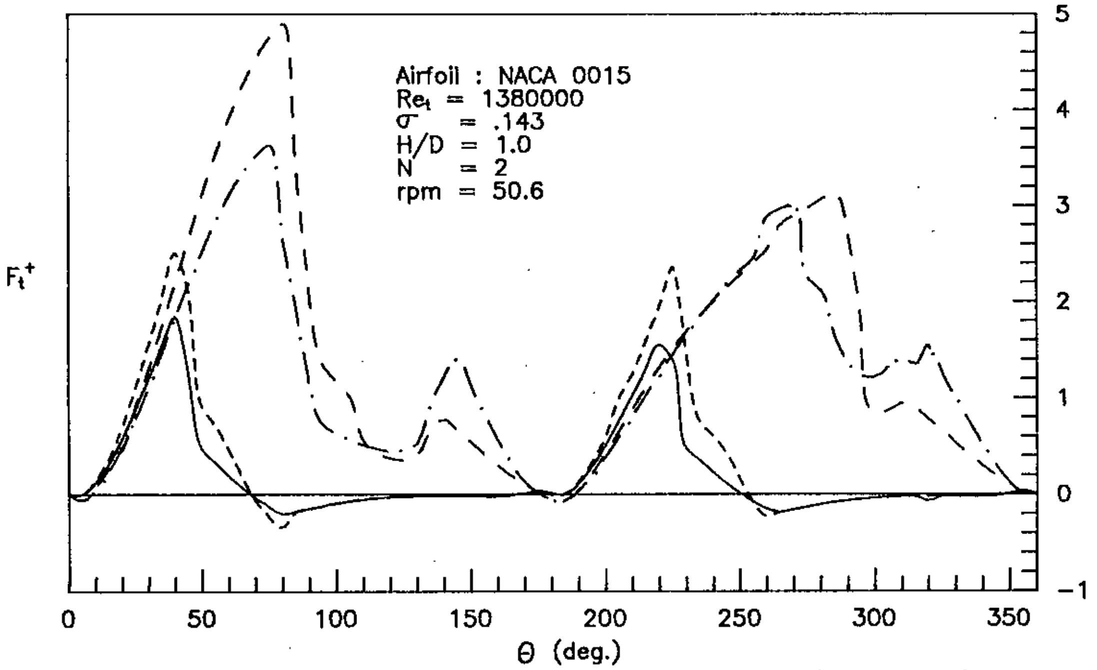

Figure 5.21 : Comparisons of local non−dimensional tangential forces with and without dynamic stall.

—— calc. (without dynamic stall at λ = 1.5)
—·— calc. (without dynamic stall at λ = 3.0)
---- calc. (with dynamic stall at λ = 1.5)
— — calc. (with dynamic stall at λ = 3.0)

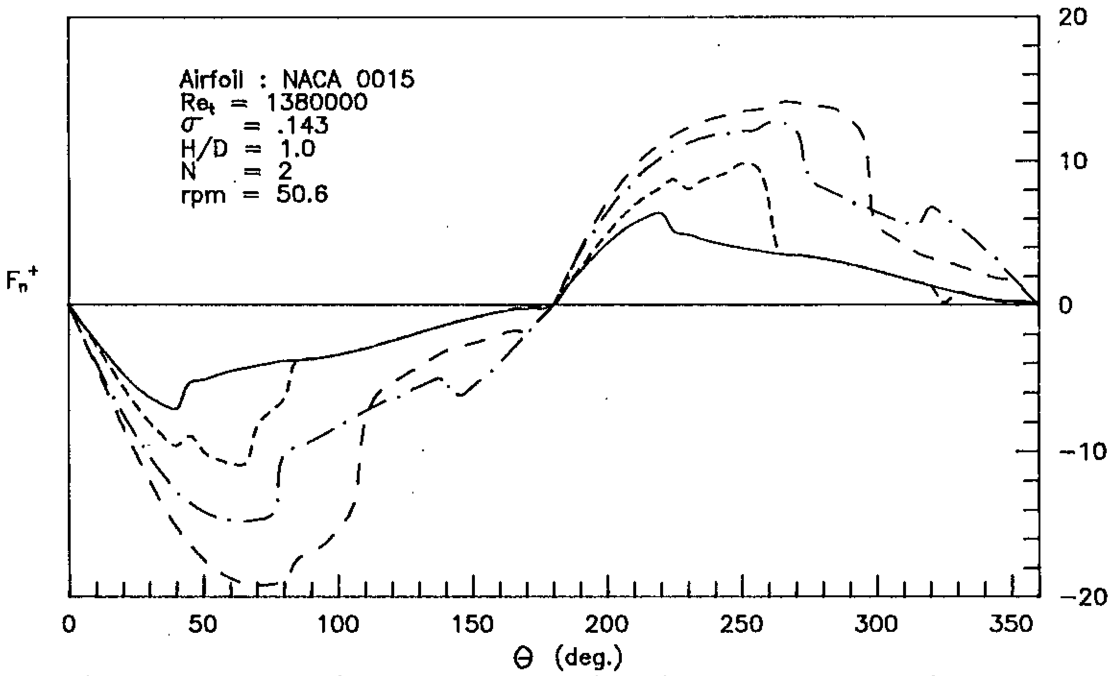

Figure 5.22 : Comparisons of local non−dimensional normal forces with and without dynamic stall.

—— calc. (without dynamic stall at λ = 1.5)
—·—· calc. (without dynamic stall at λ = 3.0)
----- calc. (with dynamic stall at λ = 1.5)
— — - calc. (with dynamic stall at λ = 3.0)

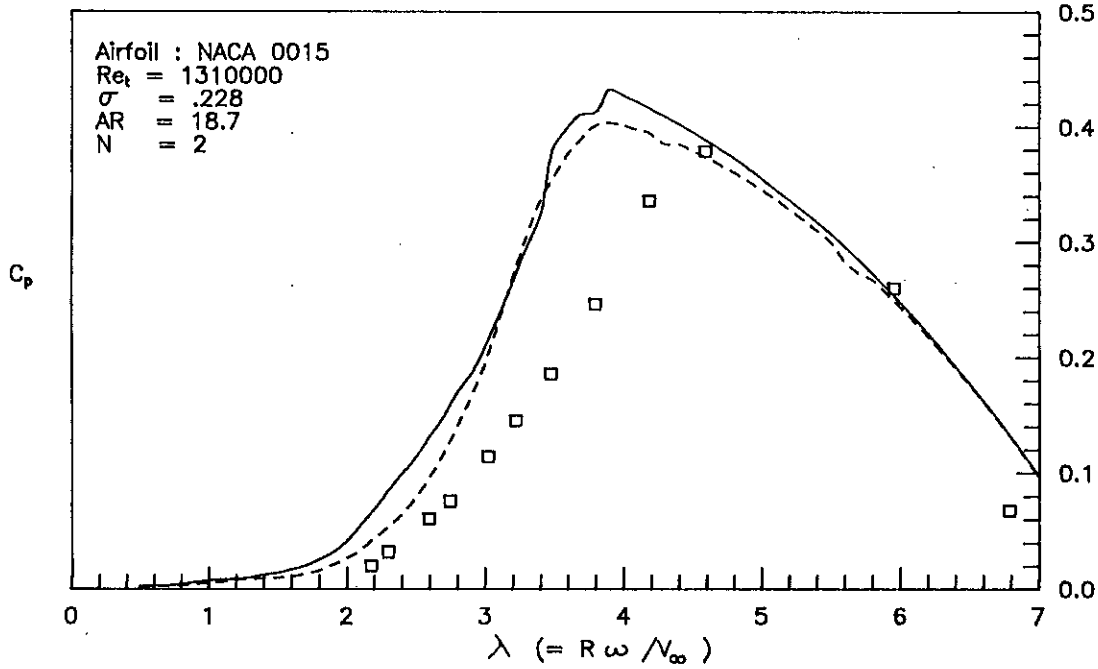

Figure 5.23 : Comparisons of experimental and calculated overall power coefficients.

---- calc. (without dynamic stall)
—— calc. (with dynamic stall)
□ □ □ expt. (3m-WVU)

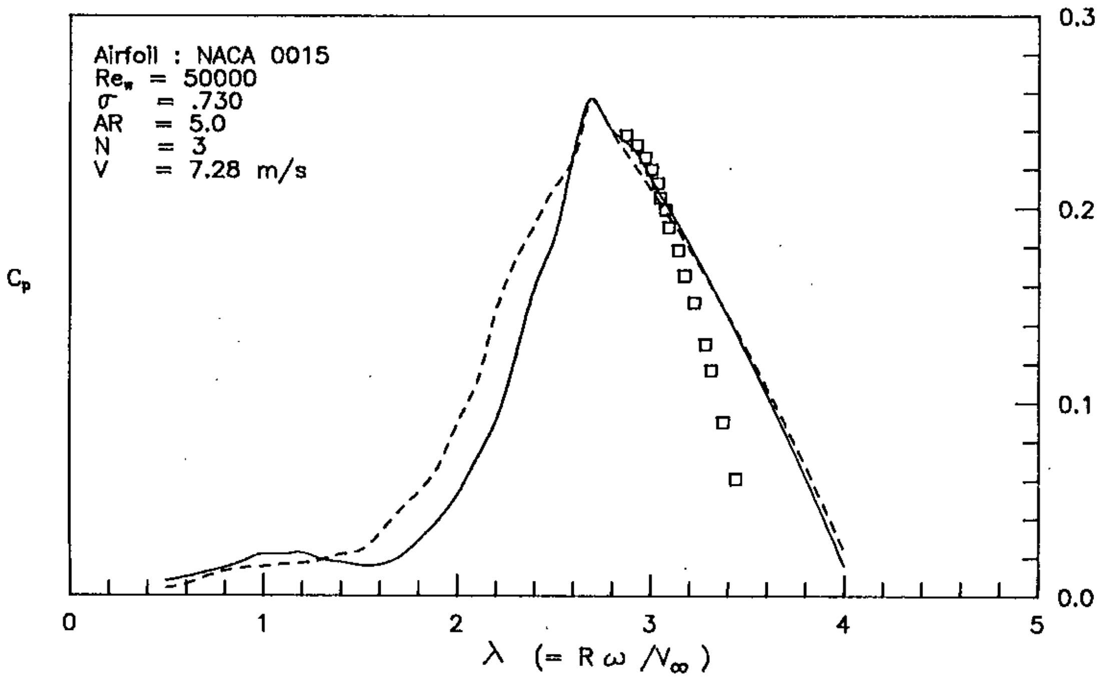

Figure 5.24 : Comparisons of experimental and calculated overall power coefficients.

---- calc. (without dynamic stall)
—— calc. (with dynamic stall)
□ □ □ expt. (VUB-model)

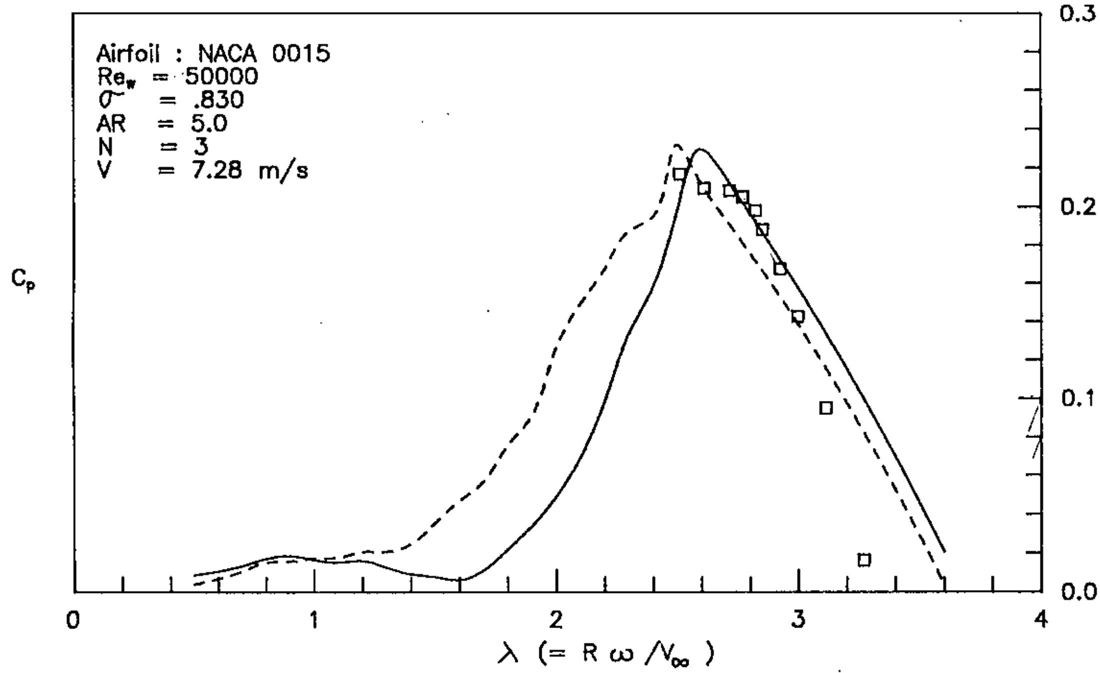

Figure 5.25 : Comparisons of experimental and calculated overall power coefficients.

- - - - calc. (without dynamic stall)
——— calc. (with dynamic stall)
□ □ □ expt. (VUB-model)

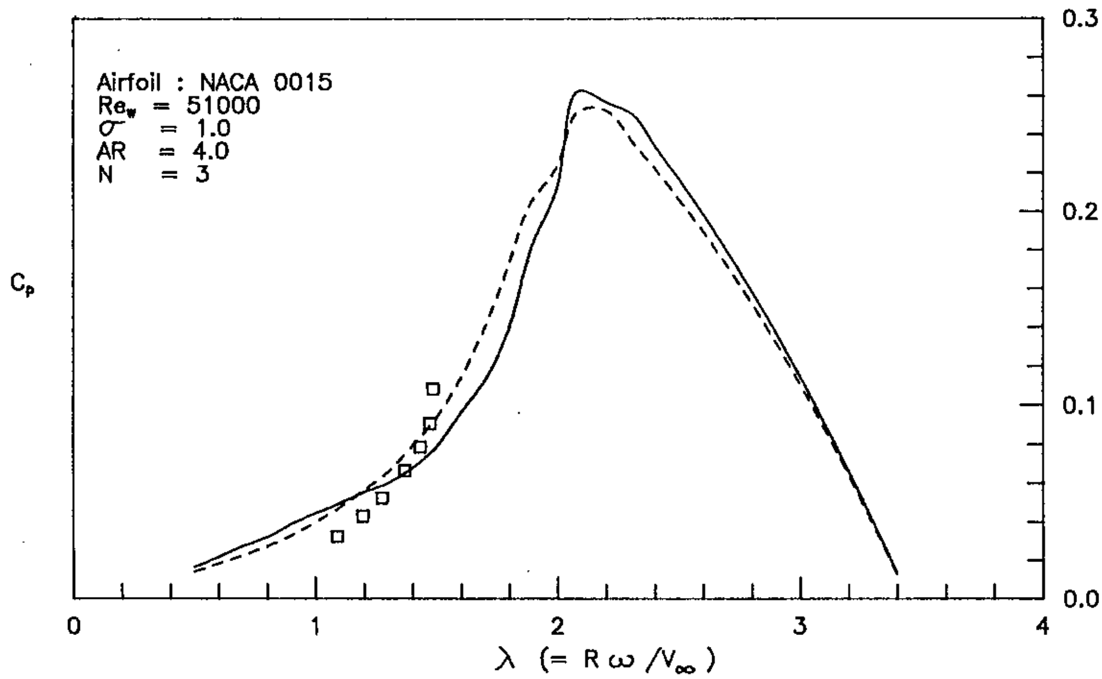

Figure 5.26 : Comparisons of experimental and calculated overall power coefficients.

- - - - calc. (without dynamic stall)
——— calc. (with dynamic stall)
□ □ □ expt. (VUB-prototype)

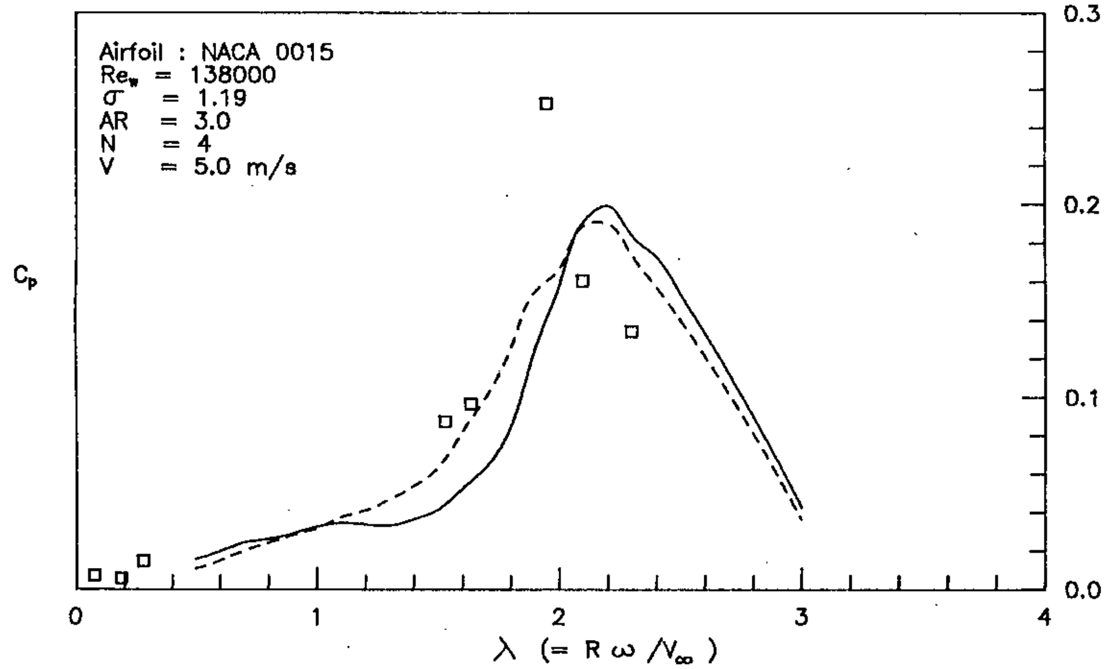

Figure 5.27 : Comparisons of experimental and calculated overall power coefficients.

- - - calc. (without dynamic stall)
—— calc. (with dynamic stall)
□ □ expt. (2.7m–Reading University)

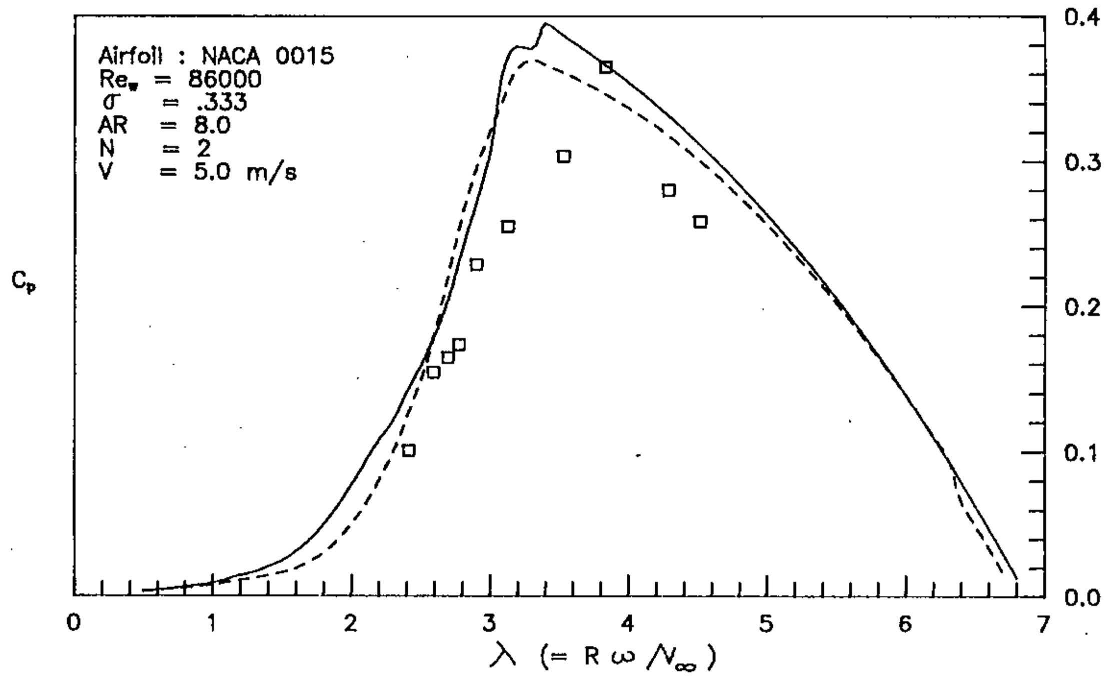

Figure 5.28 : Comparisons of experimental and calculated overall power coefficients.

- - - - calc. (without dynamic stall)
—— calc. (with dynamic stall)
□ □ □ expt. (3m–Reading University)

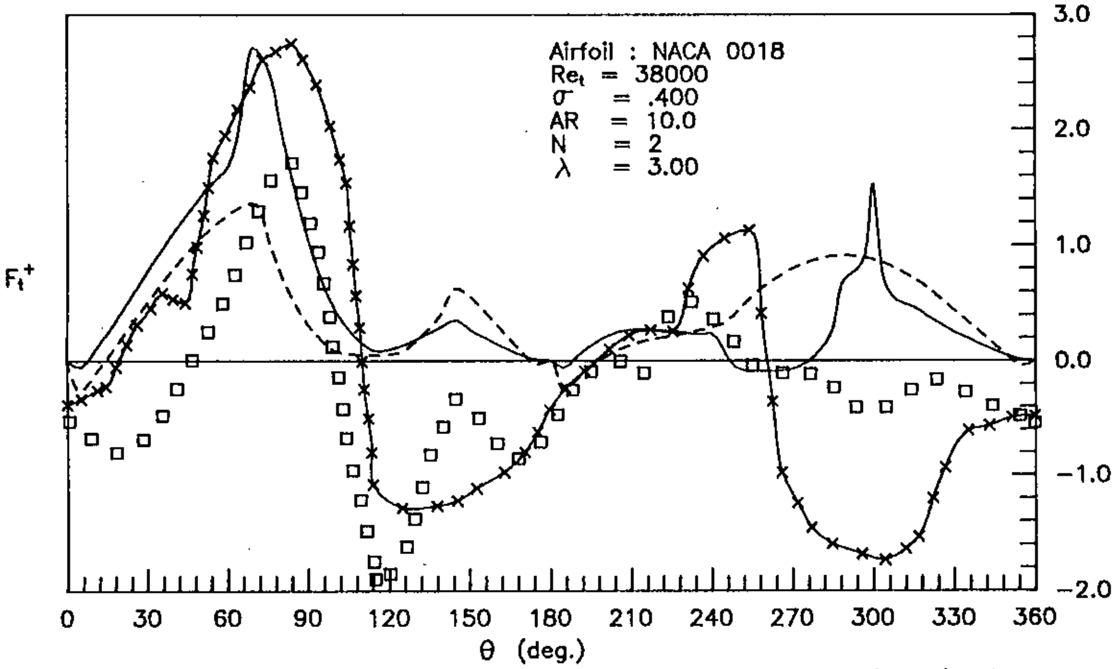

Figure 5.29 : Comparisons of experimental and calculated non-dimensional tangential forces.

---- calc. (without dynamic stall)
—— calc. (with dynamic stall)
-x-x- cacl. (double multiple streamtube with dynamic stall)
□ □ □ expt. (Sherbrooke)

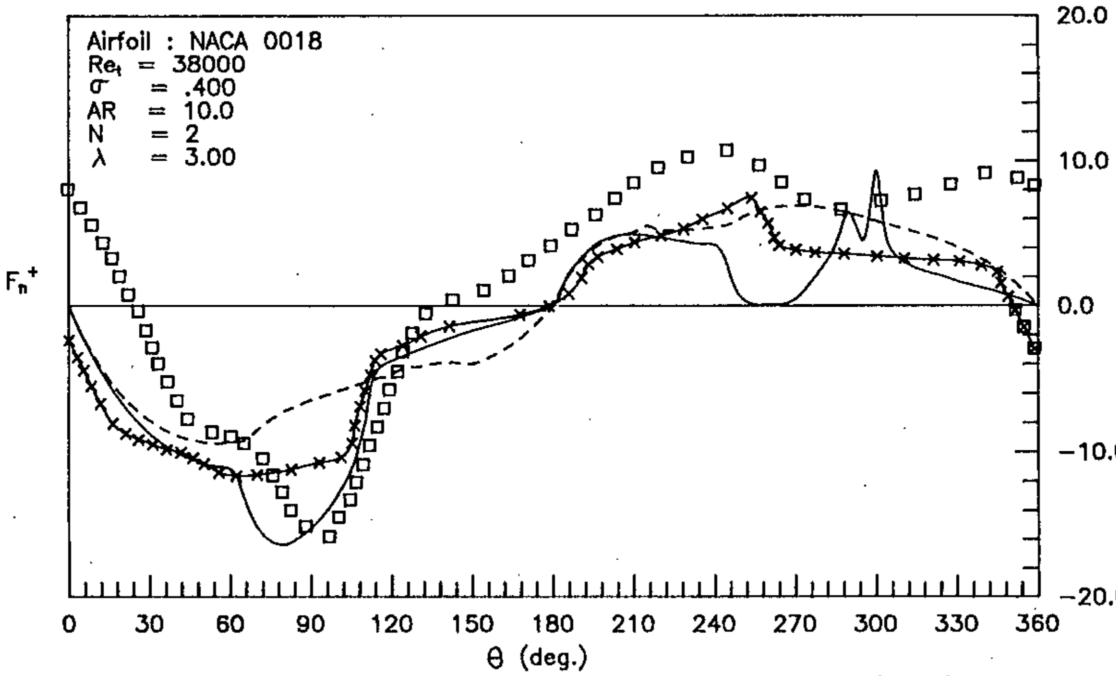

Figure 5.30 : Comparisons of experimental and calculated non-dimensional normal forces.

---- calc. (without dynamic stall)
—— calc. (with dynamic stall)
-x-x- cacl. (double multiple streamtube with dynamic stall)
□ □ □ expt. (Sherbrooke)

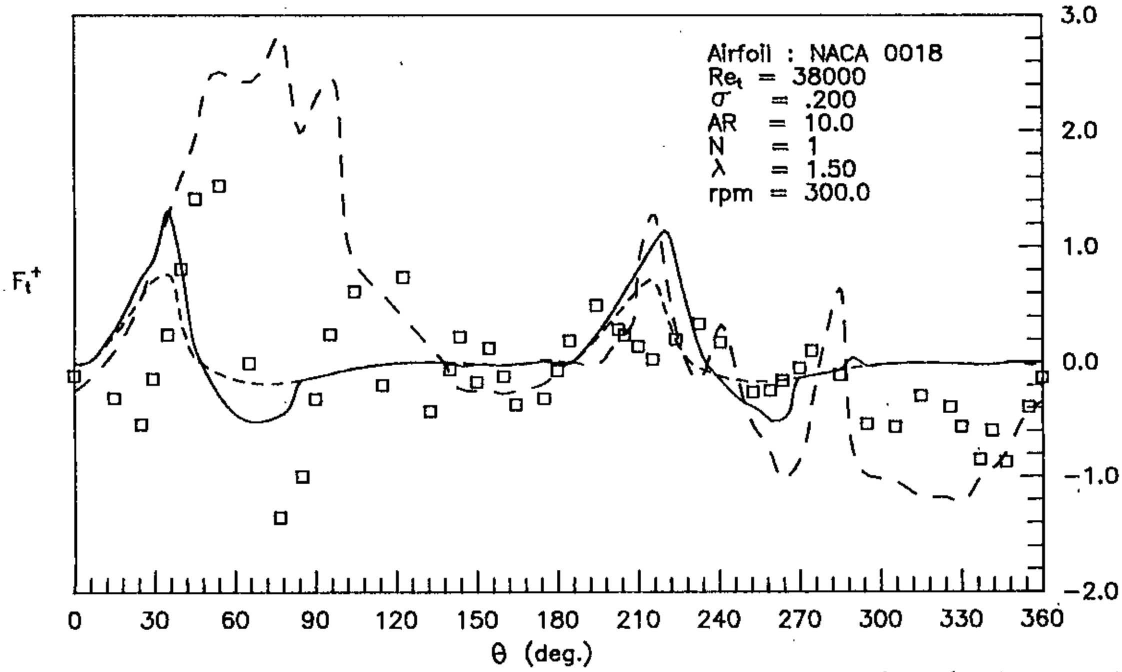

Figure 5.31 : Comparisons of experimental and calculated non-dimensional tangential forces.

---- calc. (without dynamic stall)
——— calc. (with dynamic stall)
— — — cacl. (double multiple streamtube with dynamic stall)
□ □ □ expt. (Sherbrooke)

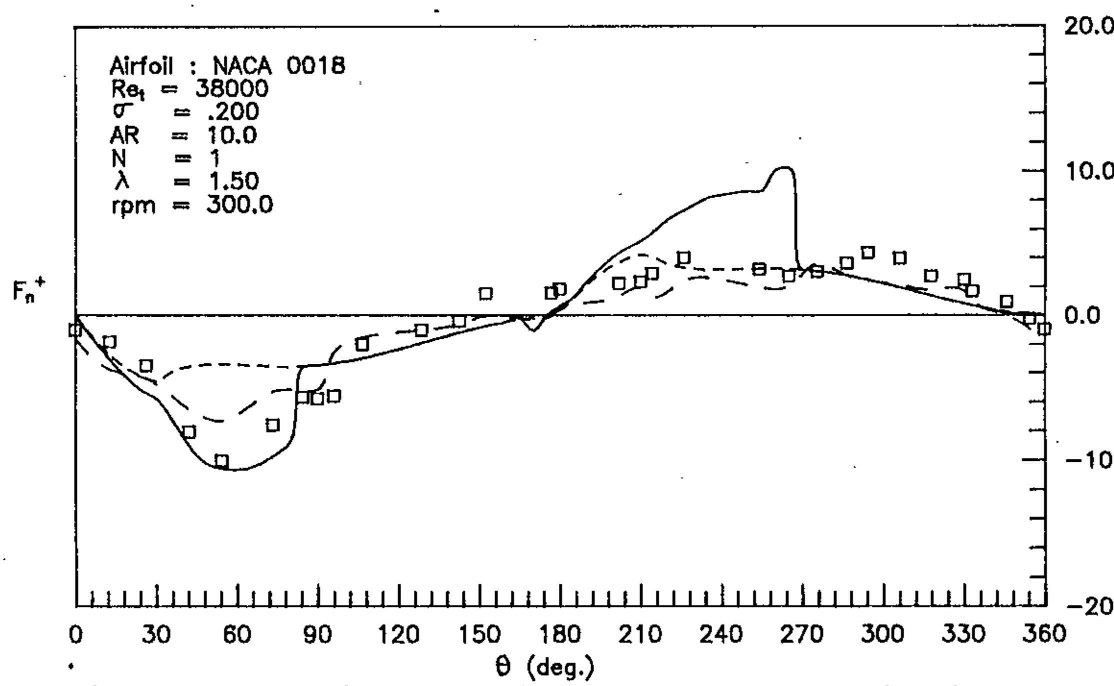

Figure 5.32 : Comparisons of experimental and calculated non-dimensional normal forces.

---- calc. (without dynamic stall)
——— calc. (with dynamic stall)
— — — cacl. (double multiple streamtube with dynamic stall)
□ □ □ expt. (Sherbrooke)

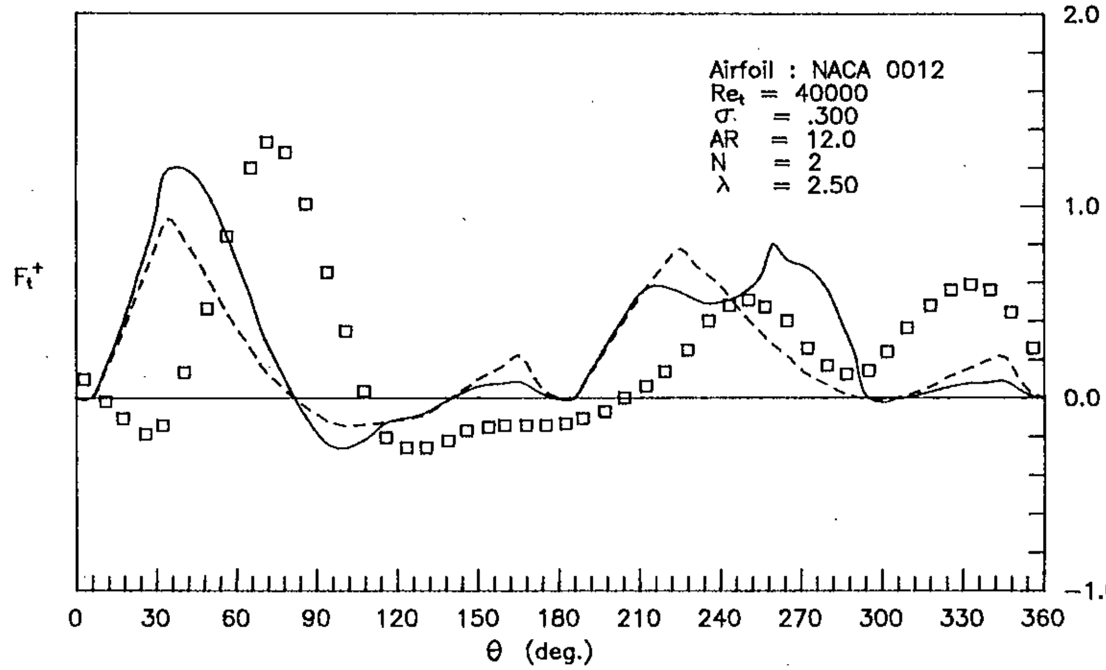

Figure 5.33 : Comparisons of experimental and calculated non–dimensional tangential forces.

- - - - calc. (without dynamic stall)
——— calc. (with dynamic stall)
□ □ □ expt. (Sandia)

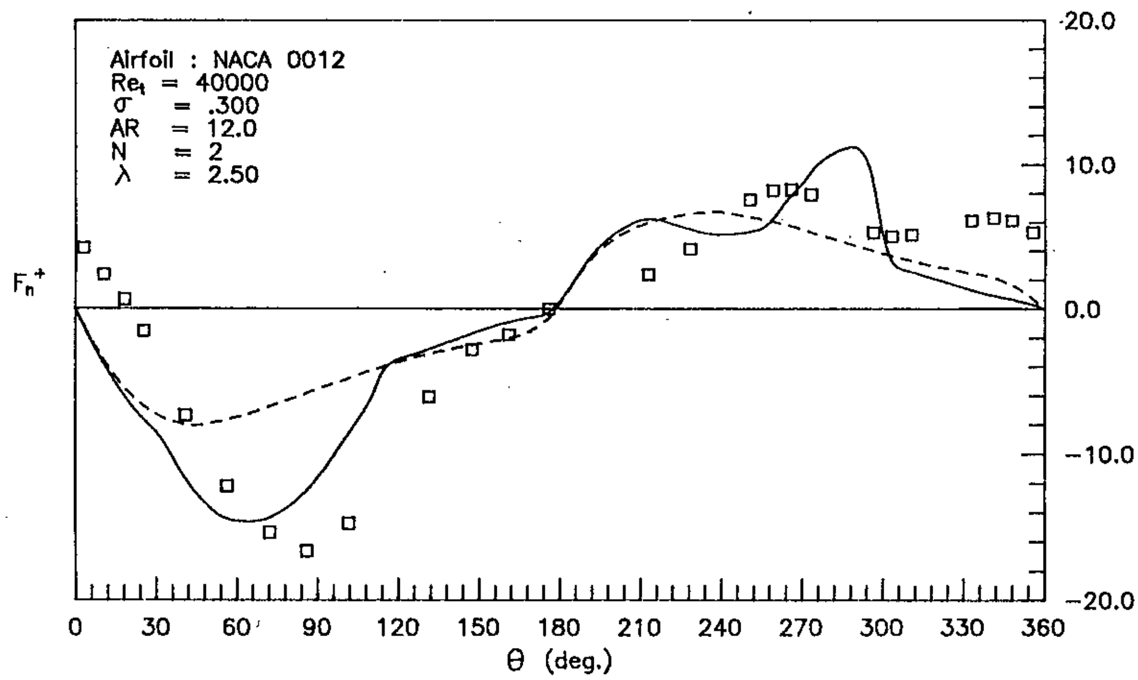

Figure 5.34 : Comparisons of experimental and calculated non–dimensional normal forces.

- - - - calc. (without dynamic stall)
——— calc. (with dynamic stall)
□ □ □ expt. (Sandia)

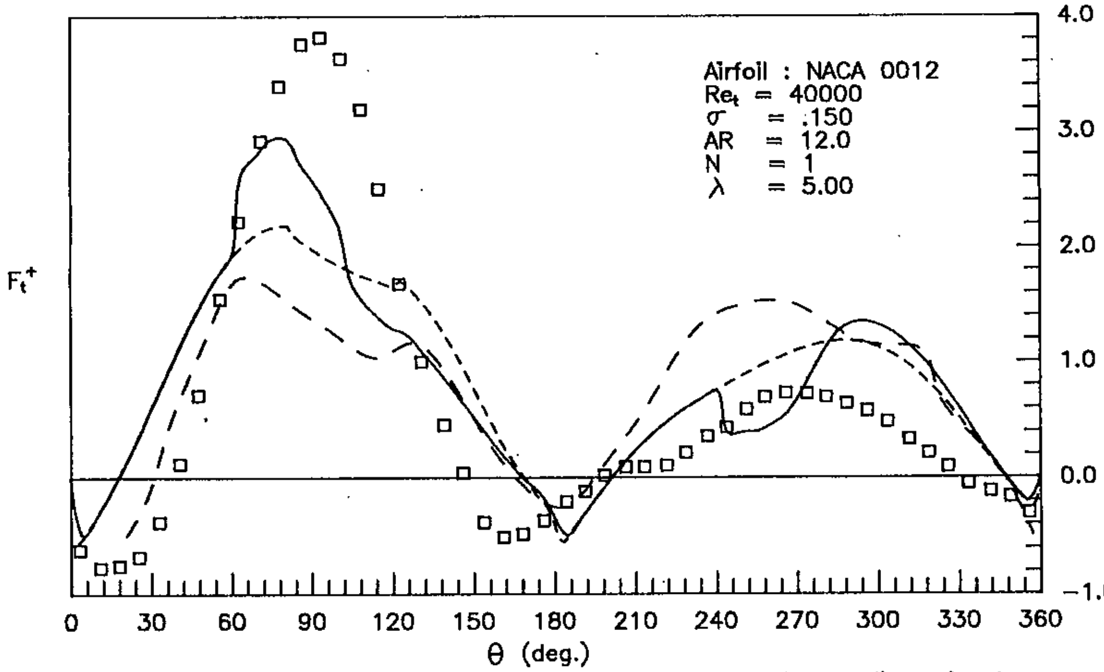

Figure 5.35 : Comparisons of experimental and calculated non-dimensional tangential forces.

- - - - calc. (without dynamic stall)
——— calc. (with dynamic stall)
— — calc. (quasi-steady vortex model)
□ □ □ expt. (Sandia)

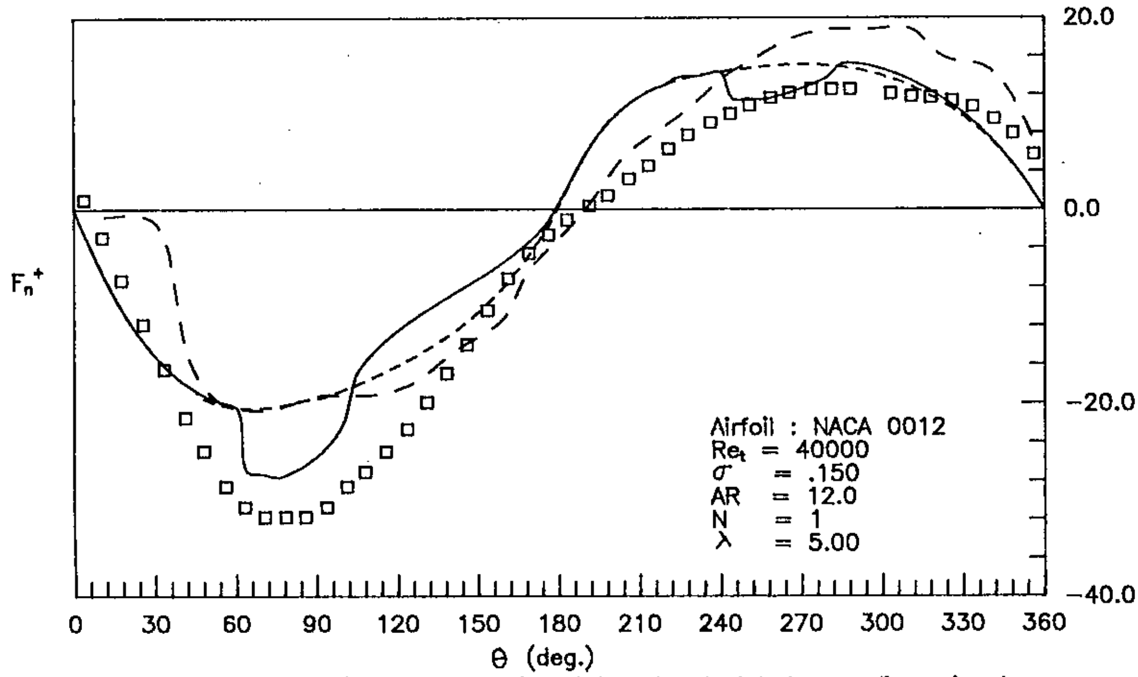

Figure 5.36 : Comparisons of experimental and calculated non-dimensional normal forces.

- - - - calc. (without dynamic stall)
——— calc. (with dynamic stall)
— — calc. (quasi-steady vortex model)
□ □ □ expt. (Sandia)

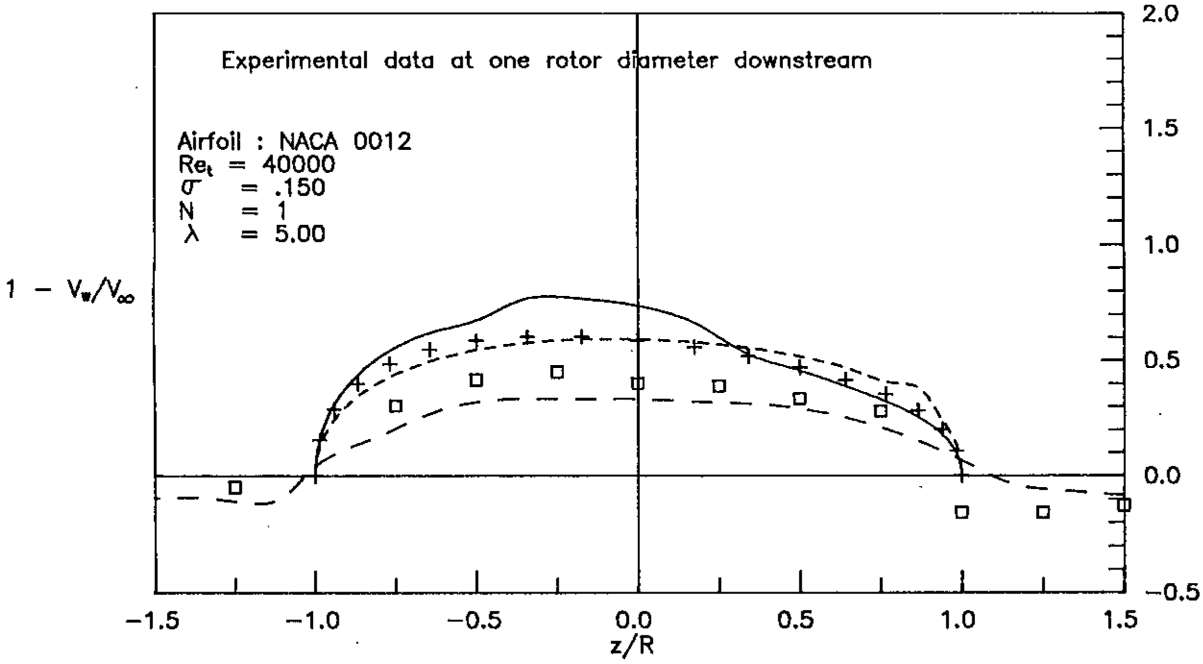

Figure 5.37 : Comparisons of experimental and calculated wake velocities.

+ + + calc. (without dynamic stall)
——— calc. (with dynamic stall)
— — calc. (dynamic vortex model)
- - - - calc. (multiple streamtube with flow curvature)
□ □ □ expt. (Sandia)

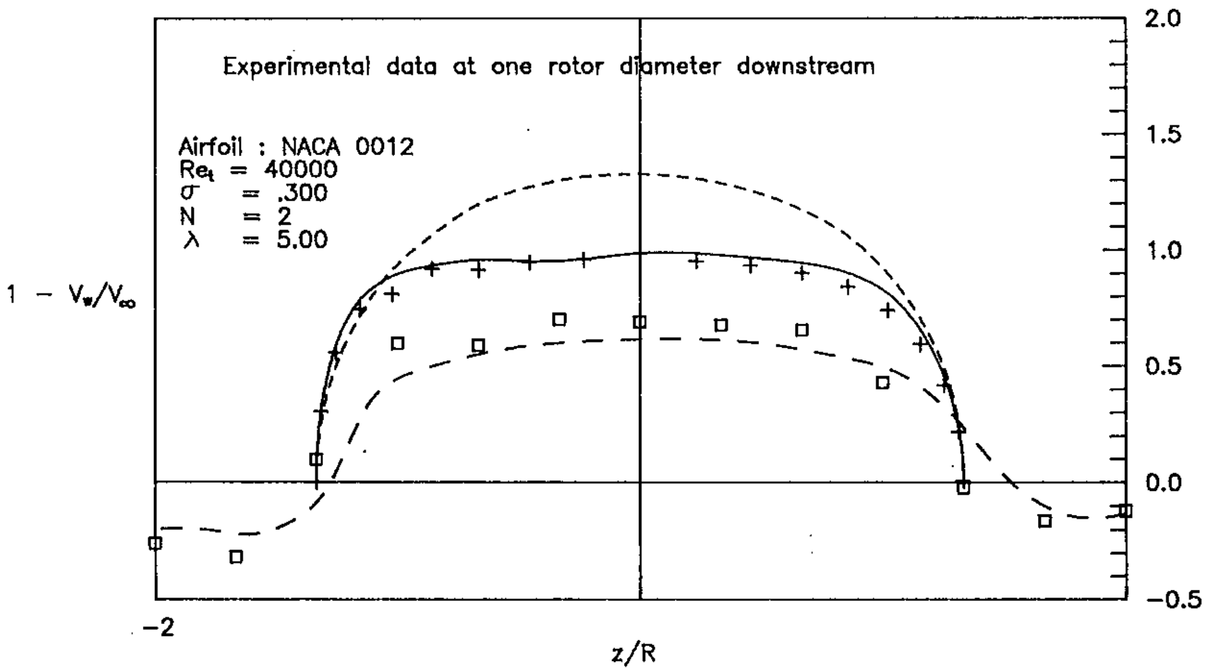

Figure 5.38 : Comparisons of experimental and calculated wake velocities.

+ + + calc. (without dynamic stall)
——— calc. (with dynamic stall)
— — calc. (dynamic vortex model)
- - - - calc. (multiple streamtube with flow curvature)
□ □ □ expt. (Sandia)

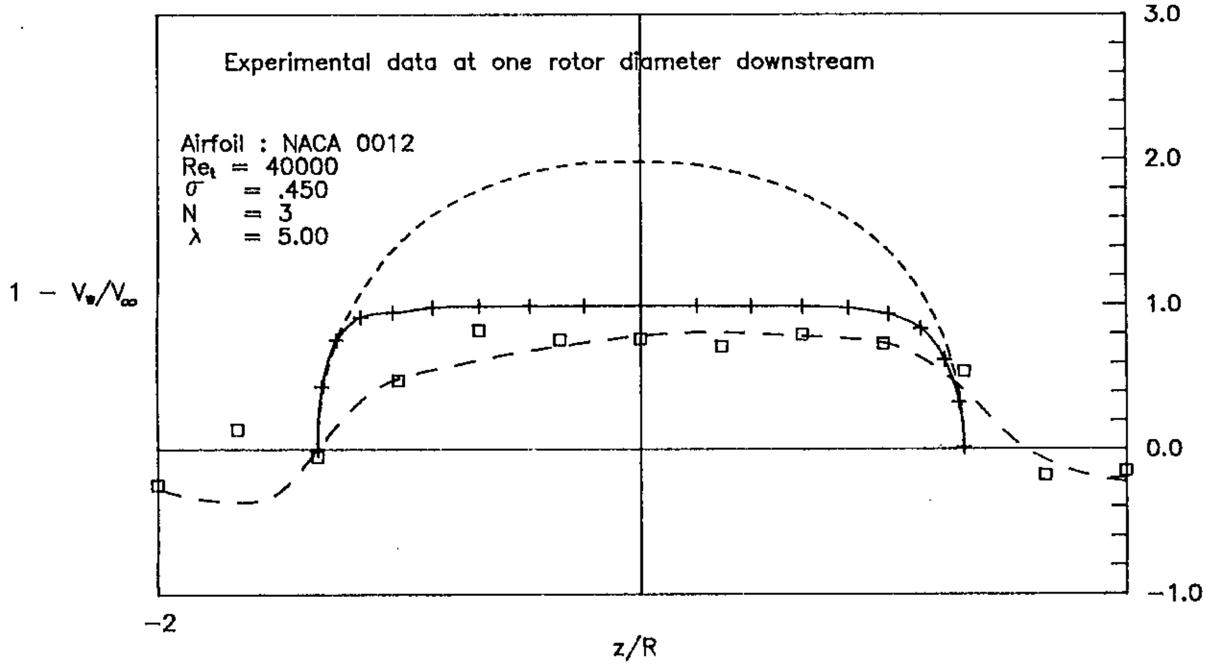

Figure 5.39 : Comparisons of experimental and calculated wake velocities.

+ + + calc. (without dynamic stall)
——— calc. (with dynamic stall)
— — calc. (dynamic vortex model)
- - - - calc. (multiple streamtube with flow curvature)
□ □ □ expt. (Sandia)

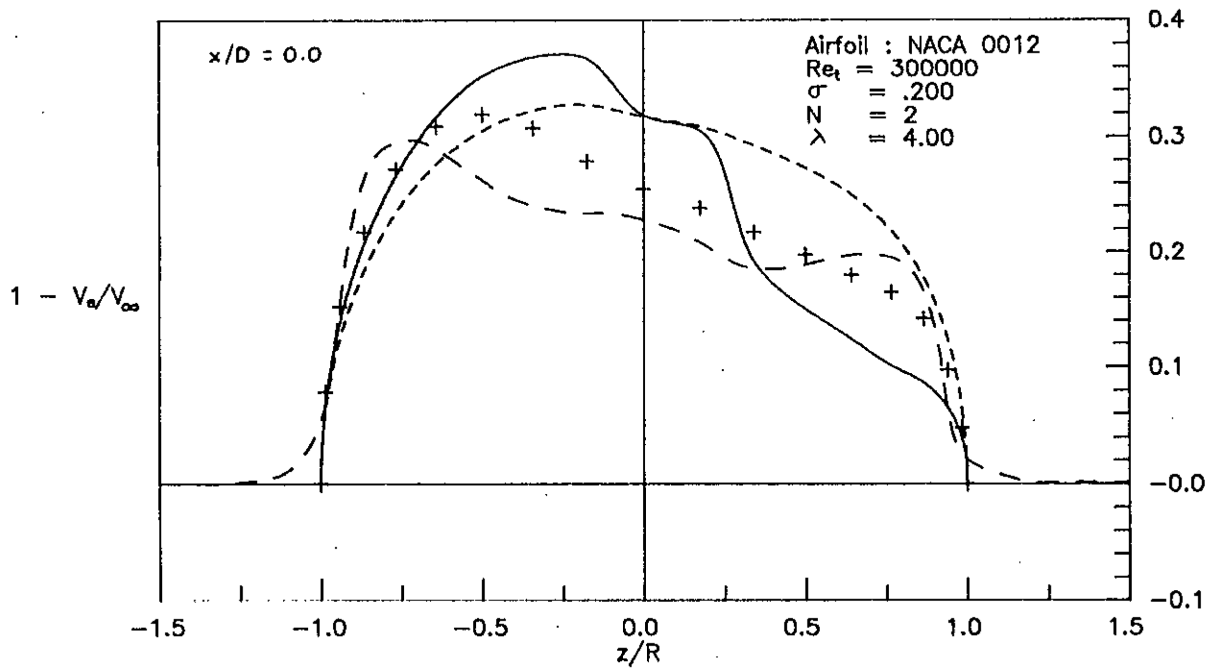

Figure 5.40 : Comparisons of calculated velocity distribution at the center of the rotor

+ + + calc. (without dynamic stall)
——— calc. (with dynamic stall)
— — calc. (dynamic vortex model)
- - - - calc. (multiple streamtube with flow curvature)

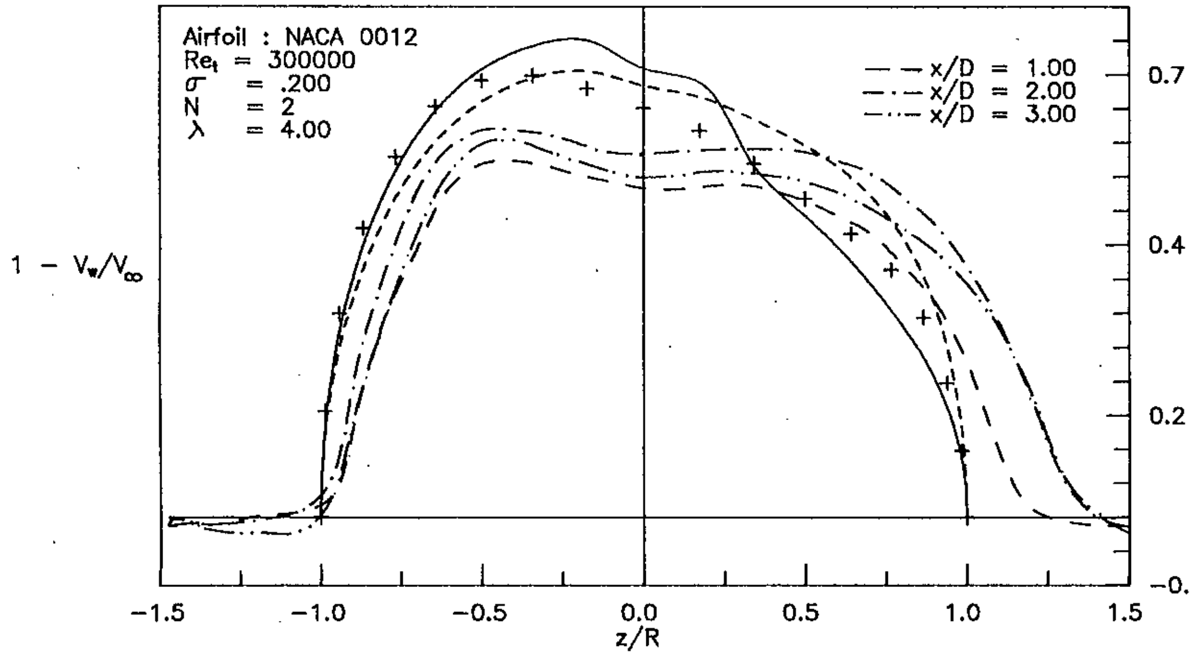

Figure 5.41 : Comparisons of calculated wake velocities.

+ + + calc. (without dynamic stall)
——— calc. (with dynamic stall)
— — —·— —··— calc. (dynamic vortex model)
- - - - calc. (multiple streamtube with flow curvature)

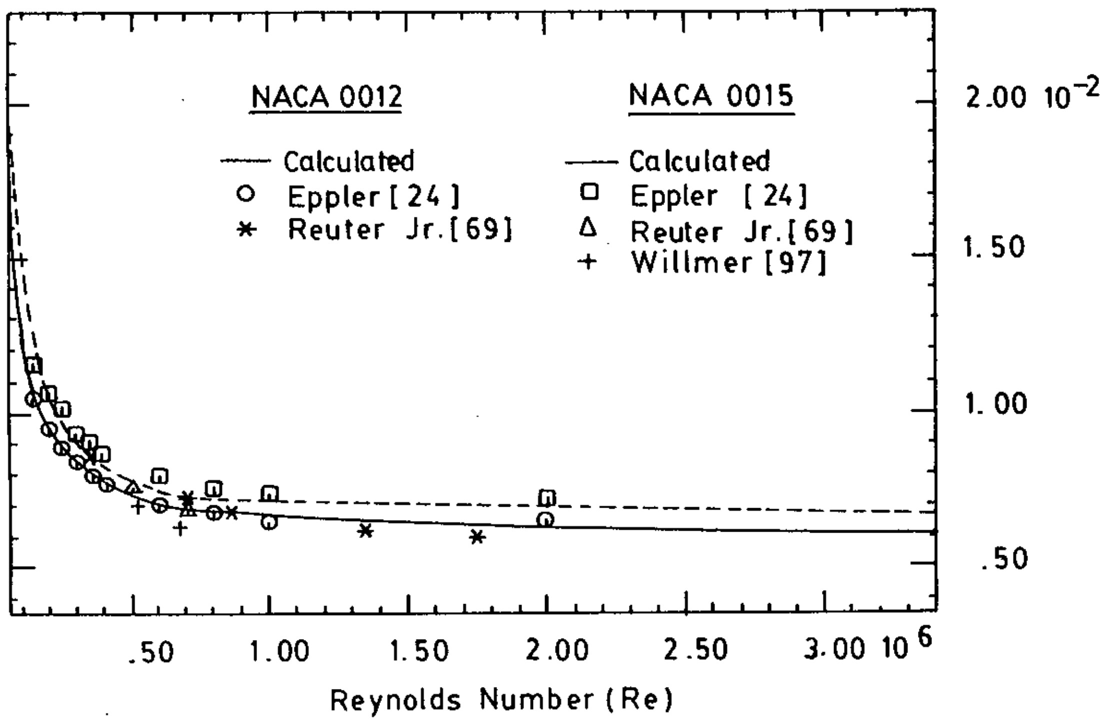

Figure B.1 : Comparisons of experimental and analytical zero-lift drag coefficients for the airfoils NACA 0015.

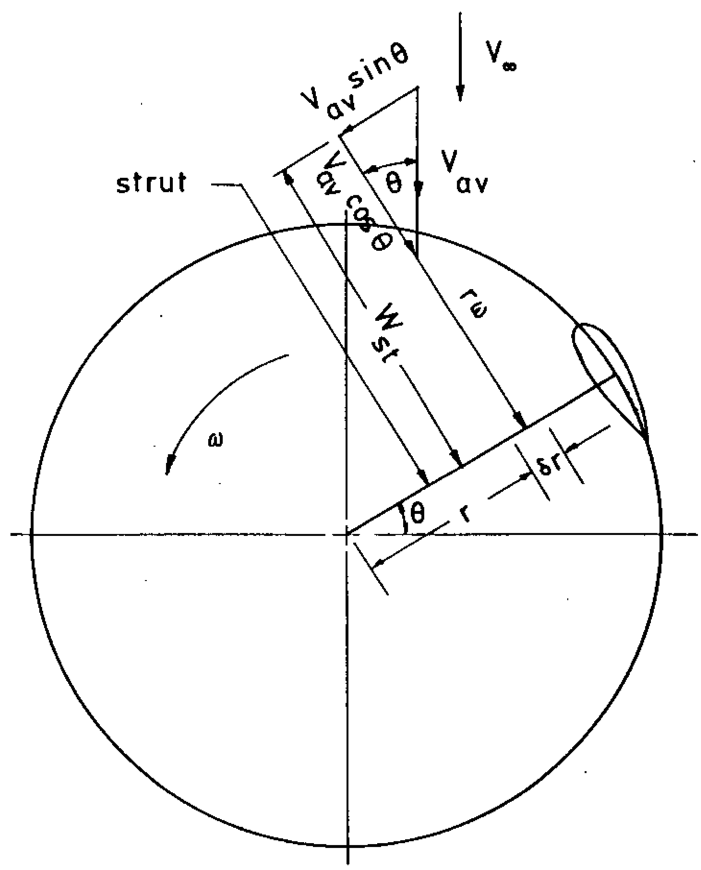

Figure D.1 : Flow velocities on the stut of a straight-bladed wind turbine

APPENDICES

APPENDIX-A : FLOW DIAGRAM OF COMUTATIONAL METHODS

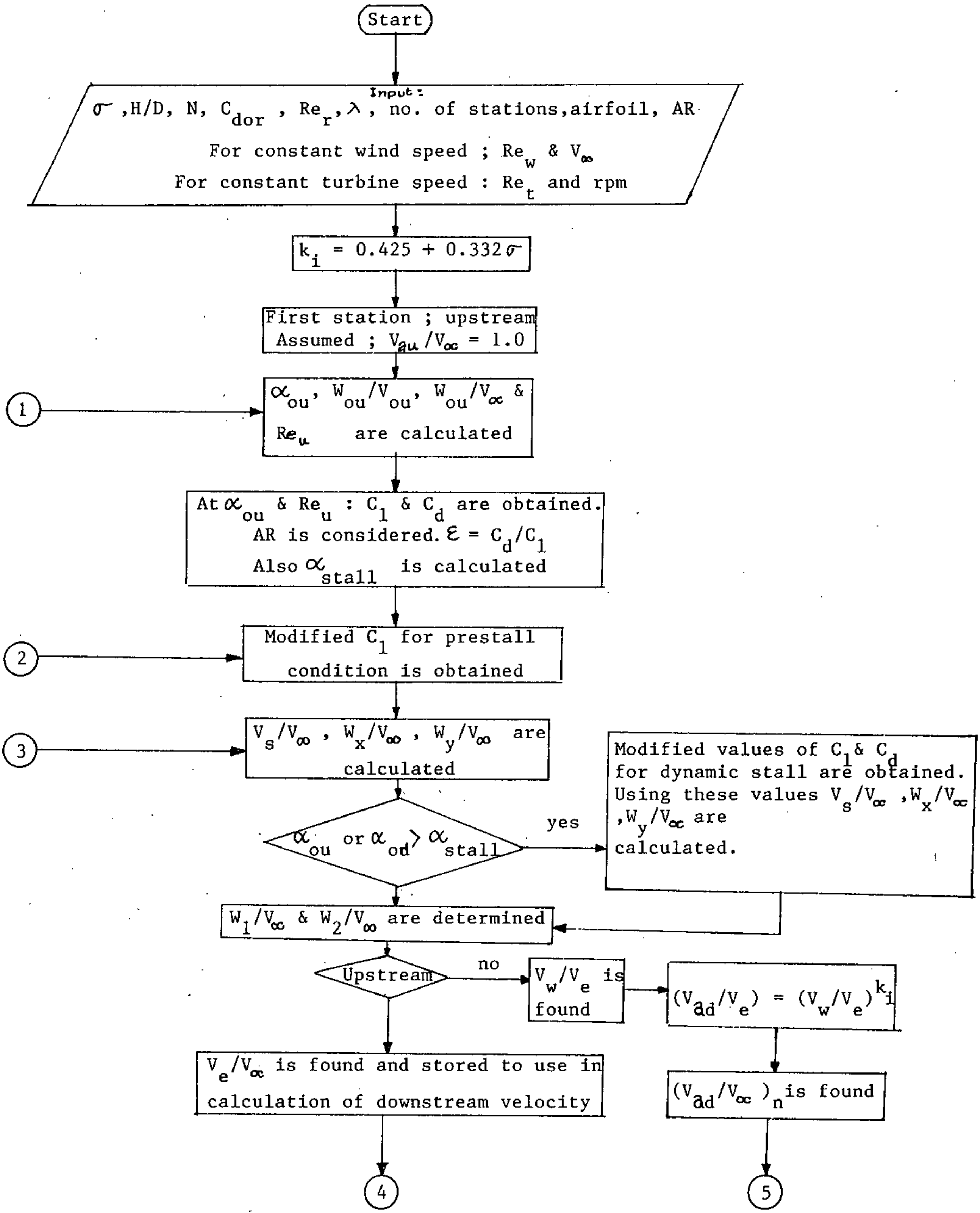

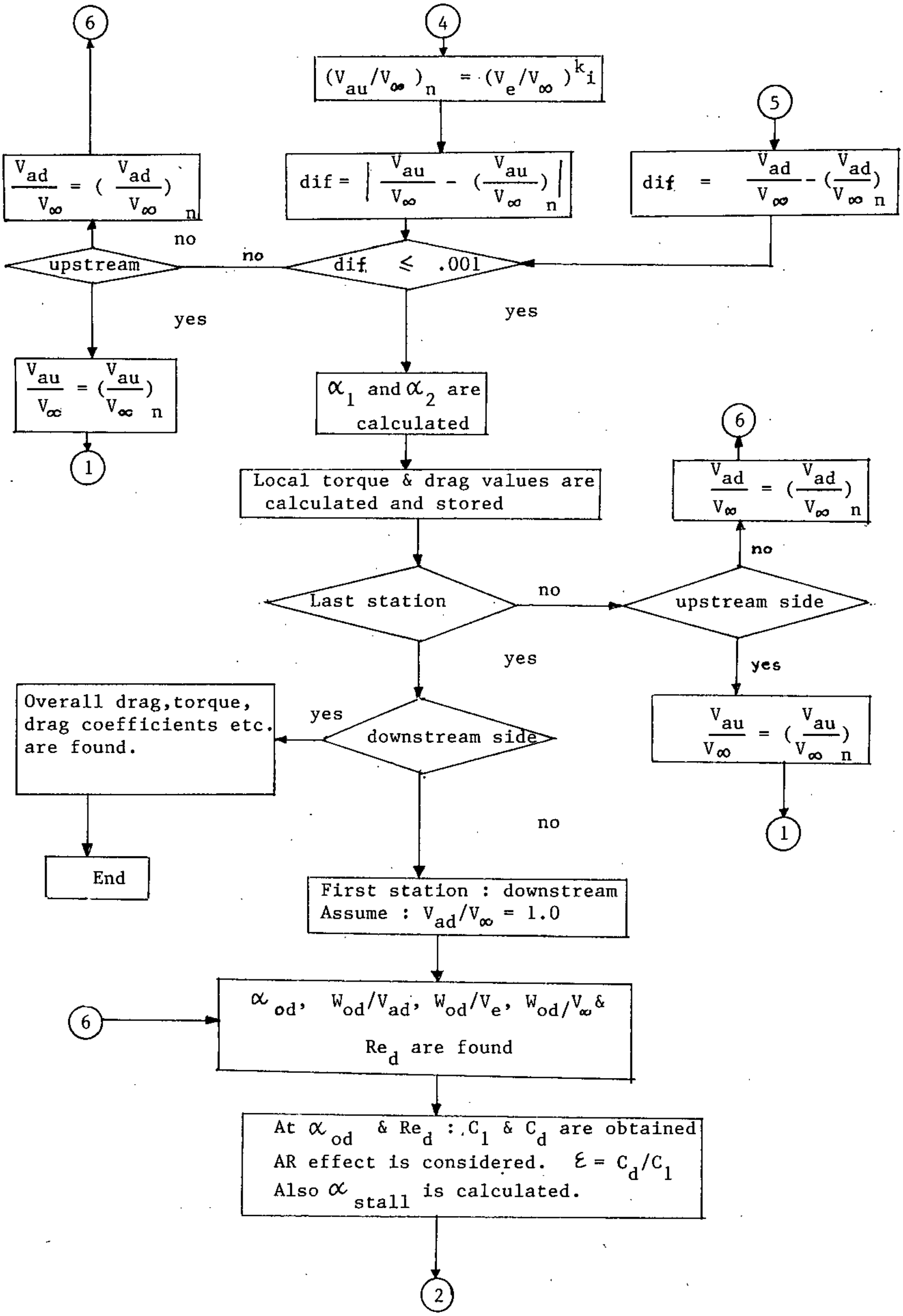
6
4
$(V_{au}/V_\infty)_n = (V_e/V_\infty)^{k_i}$
5
$\frac{V_{ad}}{V_\infty} = (\frac{V_{ad}}{V_\infty})_n$
$dif = \left| \frac{V_{au}}{V_\infty} - (\frac{V_{au}}{V_\infty})_n \right|$
$dif = \frac{V_{ad}}{V_\infty} - (\frac{V_{ad}}{V_\infty})_n$
no
upstream
no
dif $\leq$ .001
yes
yes
$\frac{V_{au}}{V_\infty} = (\frac{V_{au}}{V_\infty})_n$
1
α_1 and α_2 are calculated
6
Local torque & drag values are calculated and stored
$\frac{V_{ad}}{V_\infty} = (\frac{V_{ad}}{V_\infty})_n$
no
Last station
no
upstream side
yes
yes
Overall drag,torque, drag coefficients etc. are found.
yes
downstream side
$\frac{V_{au}}{V_\infty} = (\frac{V_{au}}{V_\infty})_n$
no
1
End
First station : downstream
Assume : $V_{ad}/V_\infty = 1.0$
6
α_{od}, W_{od}/V_{ad}, W_{od}/V_e, W_{od}/V_∞ &
Re_d are found
At α_{od} & Re_d : C_l & C_d are obtained
AR effect is considered. $\varepsilon = C_d/C_l$
Also α_{stall} is calculated.
2

APPENDIX-B

EFFECT OF ZERO-LIFT-DRAG COEFFICIENT

The aerodynamic efficiency of a vertical axis Darrieus wind turbine is strongly influenced by the value of the zero - lift - drag coefficient. To predict the performance characteristics properly it is necessary to consider a reasonable value of the zero - lift - drag coefficient. It is observed that the zero - lift - drag coefficient is function of the chord-radius ratio in addition to other factors.

Migliore et al [23] found experimentally that minimum value of the drag co-efficient depends on the chord-radius ratio. In the present method an analytical expression of the zero-lift -drag coefficient as function of the chord-radius ratio and Reynolds number is given. This expression is obtain from a fit of experimental results conducted in the laboratory of Virje Universiteit Brussel in a vertical axis straight-bladed Darrieus wind turbine. Similar expressions are also found for a vertical - axis curved - bladed Darrieus turbine.

The expression of the zero-lift-drag coefficient corrected for chord-radius ratio is introduced in the following form,

$$C_{doc} = C_{do} + b\left[\frac{C}{R} - \left(\frac{C}{R}\right)_o\right] \tag{B.1}$$

where the C_{do} is the zero-lift-drag coefficient. The expression of C_{do} is taken from the reference [19] and is given as,

$$C_{do} = C_{dor}\left(\frac{Re}{Re_r}\right) \tag{B.2}$$

where $(\frac{C}{R})$ is any chord-radius ratio. $(\frac{C}{R})_o$ indicate the chord-radius ration upto which value, the correction of the zero-lift-drag coefficient due to chord-radius ratio is not necessary. b is a constant. For a straight-bladed wind turbine $(\frac{C}{R})_o = .180$ and $b = .047$ at $Re_r = 500000$ and for a curved-bladed Darrieus turbine with height diameter ratio 1.00, $(\frac{C}{R})_o = 0.05$ and $b = 0.045$ at $Re_r = 500000$. Re is the local Reynolds number. C_{dor} and Re_r are respectively the reference the zero-lift-drag coefficient and reference Reynolds number. The value of the exponent n is given in the table B.1.

Airfoils	Exponent, n		
	Re < 200000	2000000 < Re <600000	Re > 600000
NACA 0012	-.450	-.250	-.100
NACA 0015	-.500	-.300	-.060

TABLE B.1 : Exponent n for zero-lift-drag coefficient.

The values of the zero-lift-drag coefficients C_{d_o} for the airfoils NACA 0012 and NACA 0015, which are used in the present calculation are given in the Figure B.1. These calculated values of the zero-lift-drag coefficients are based on $C_{d_o} = .0074$ at $Re_r = 500000$ for the airfoil NACA 0012 and $C_{dor} = .0078$ at $Re_r = 500000$ for the airfoil NACA 0015. Comparison of recent two dimensional experimental results of $C_{d_{or}}$ from Eppler[9]. Reuter Jr.[31] and Willmer[43] with the calculated values of Cdo in the Figure B.1, proves the validity of the present forms of semi - empirical equations.

APPENDIX - C

EFFECT OF ASPECT RATIO

For the performance prediction of a straight-bladed Darrieus wind turbine, the effect of finite aspect ratio on the airfoil characteristics are necessary. Since the finite wing and finite blade a straight-bladed wind turbine are of similar pattern, so wing theory may be applied for the finite aspect ratios effects on the airfoil characteristics before using them for the performance prediction of a straight-bladed wind turbine.

For the wing of finite span, there occurs always downwash and power required to induce downwash is expressed in terms of induced drag. The downwash velocity is created by the presence of tip vortices. The total drag coefficient of a finite wing is given by,

$$C_d = C_{d_o} + C_{d_i} \tag{C.1}$$

where C_{d_o} is the section drag coefficient for infinite aspect ratio while C_{d_i} is the induced drag coefficient, C_{d_i} is expressed as,

$$C_{d_i} = \frac{C_l^2}{2\pi AR} \tag{C.2}$$

where AR indicates the aspect ratio of the turbine blade.

Introducing the value of C_{d_i} in the equation (C.1),

$$C_d = C_{d_o} + \frac{C_l^2}{2\pi AR} \tag{C.3}$$

The angle of attack corrected for finite aspect ratio effect is obtained as,

$$\alpha = \alpha_o + \alpha_i \tag{C.4}$$

where α_o indicates the angle of attack for finite wing and α_i is the induced angle. The expression of the induced angle α_i is,

$$\alpha_i = \frac{C_l}{2\pi AR} \tag{C.5}$$

substituting equation (C.5) in the equation (C.4)

$$\alpha = \alpha_o + \frac{C_l}{2\pi AR} \tag{C.6}$$

The above two equations (C.5) and (C.6) are developed on the assumptions of uniform distribution of downwash and they are explicitly valid only for wings possessing an elliptical lift distribution. However other cases are dealt with considering appropriate correction factors. Letting τ is the correction factor for the induced angle and σ is the correction factor for the induced drag, the expressions of C_d and α become,

$$C_d = C_{do} + \frac{C_l^2}{2\pi AR}(1+\sigma) \tag{C.7}$$

$$\alpha = \alpha_o + \frac{C_l}{2\pi AR}(1+\tau) \tag{C.8}$$

For a rectangular wing there are also two limiting cases. When the chord is large compared with the span, aspect ratio AR approaches zero. In this case Betz finds an elliptical distribution of loading. As the aspect ratio increases to infinite the loading approaches rectangular distribution. The values of τ and σ are taken from the reference [25].

APPENDIX - D

EFFECT OF BLADE SUPPORTING STRUTS

There will be losses of power due to additional drag produced by the blade supporting struts. An expression of losses of power due to drag will be derived in this section with reasonable approximation.

Figure D.1 shows the flow velocities appearing on the strut. The elemental force due to drag on the strut with elemental length δr is expressed as,

$$\delta F_{st} = \frac{1}{2} C_{d,s} \rho W_{st}^2 \delta A_{st} \tag{D.1}$$

where $C_{d,s}$ is the drag coefficient in the strut profile. W_{st} is the relative flow velocity component perpendicular to the strut and acting in the horizontal plane as shown in the Figure D.1. The elemental strut area δA_{st} is (Figure D.1),

$$\delta A_{st} = b_{st} \delta r \tag{D.2}$$

where b_{st} is the width of the strut. From the equation (D.1) and (D.2), one obtains,

$$\delta F_{st} = \frac{1}{2} C_{d,s} \rho b_{st} W_{st}^2 \delta r \tag{D.3}$$

The relative flow velocity perpendicular to the strut and in the horizontal plane of the turbine is written as,

$$W_{st} = (V_{av} cos\theta + r\omega) \tag{D.4}$$

For the present calculation, the velocity component $V_{av} sin\theta$ (Figure D.1) is omitted. It is assumed that it will have the negligible effect in the result. V_{av} is the average induced velocity. The induced velocity varies with the azimuth angle. The average induced velocity V_{av} is obtained as,

$$V_{av} = \frac{1}{n} \sum_{n=1}^{n} \frac{(V_{au} + V_{ad})}{2} \tag{D.5}$$

For the multiple streamtube theory, induced velocity in the upstream side V_{au} equals the induced velocity in the downstream side V_{ad} . So $V_a = V_{au} = V_{ad}$. n is the number of stations for the half revolution of the turbine. Average induced velocity has been considered that made the analysis simple and it is assumed that it will effect the result negligibly. Now from the equations (D.3) and (D.4) , one obtains,

$$\delta F_{st} = \frac{1}{2} C_{d,,} \rho b_{st} \left(V_{av} cos\theta + r\omega\right)^2 \delta r \tag{D.6}$$

The elemental torque on the strut with strut length δr

$$\delta Q_{st} = \delta F_{st} r \tag{D.7}$$

From equations (D.6) and (D.7),

$$\delta Q_{st} = \frac{1}{2} C_{d,,} \rho b_{st} \left(V_{av} cos\theta + r\omega\right)^2 r \delta t \tag{D.8}$$

After integration,

$$Q_{st} = \frac{1}{2} C_{d,,} \rho b_{st} \int_0^R \left(V_{av} cos\theta + r\omega\right)^2 r dr \tag{D.9}$$

The above equation may be written as,

$$Q_{st} = \frac{1}{2} C_{d,,} \rho b_{st} \left(V_{av}^2 \frac{1}{2} R^2 cos^2\theta + \frac{2}{3} V_{av} \omega R^3 cos\theta + \omega^2 \frac{R^4}{4} \right) \tag{D.10}$$

The average torque on a single strut is

$$\bar{Q}_{st} = \frac{1}{2\pi}\int_0^{2\pi} Q_{st}\,d\theta \tag{D.11}$$

Now introducing the value of Q_{st} from the equation (D.10), one may obtain the following form,

$$\bar{Q}_{st} = \frac{1}{8} C_{d_{st}} \rho b_{st} \omega^2 R^4 \left[1 + \left(\frac{V_{av}}{R\omega}\right)^2\right] \tag{D.12}$$

The loss of power due to the drag on the strut,

$$P_o = N_{st} \bar{Q}_{st} \omega \tag{D.13}$$

where N_{st} is the number of the supporting arms (struts). ω is the angular velocity in rad/sec. From the equations(D.12) and (D.13),

$$P_o = \frac{1}{8} C_{d_{st}} N_{st} \rho b_{st} \omega^3 R^4 \left[1 + \left(\frac{V_{av}}{R\omega}\right)^2\right] \tag{D.14}$$

The strut power coefficient is defined as,

$$C_p = \frac{P_0}{\frac{1}{2}\rho A V_\infty^3} \tag{D.15}$$

Now from the above two equations (D.14) and (D.15), one may obtain (inserting tip speed ratio $\lambda = R\omega/V_\infty$ and $A = 2RH$),

$$C_p = \frac{1}{8} C_{d_{st}} N_{st} \frac{b_{st}}{H} \lambda^3 \left[1 + \frac{1}{\lambda^2} \cdot \frac{V_{av}^2}{V_\infty^2}\right] \tag{D.16}$$

which may be written as,

$$C_p = \frac{1}{8} C_{d_{st}} N_{st} \frac{b_{st}}{H} \lambda^3 f_m \tag{D.17}$$

where

$$f_m = 1 + \frac{1}{\lambda^2}\frac{V_{av}^2}{V_\infty^2} \qquad \text{(D.18)}$$

At low tip speed ratio V_{av}/V_∞ is nearly 1.0, as a result $f_m = 1 + 1/\lambda^2$, while at high tip speed ratio the average induced velocity $(V_{av}/V_\infty) < 1.0$ and the factor f_m approaches 1.0, so the expression of the strut power coefficient at high tip speed ratio can be written in the form,

$$C_{p_{st}} = \frac{1}{8} C_{d_{st}} N_{st} \frac{b_{st}}{H} \lambda^3 \qquad \text{(D.19)}$$

APPENDIX – E
AIRFOIL CHARACTERISTICS

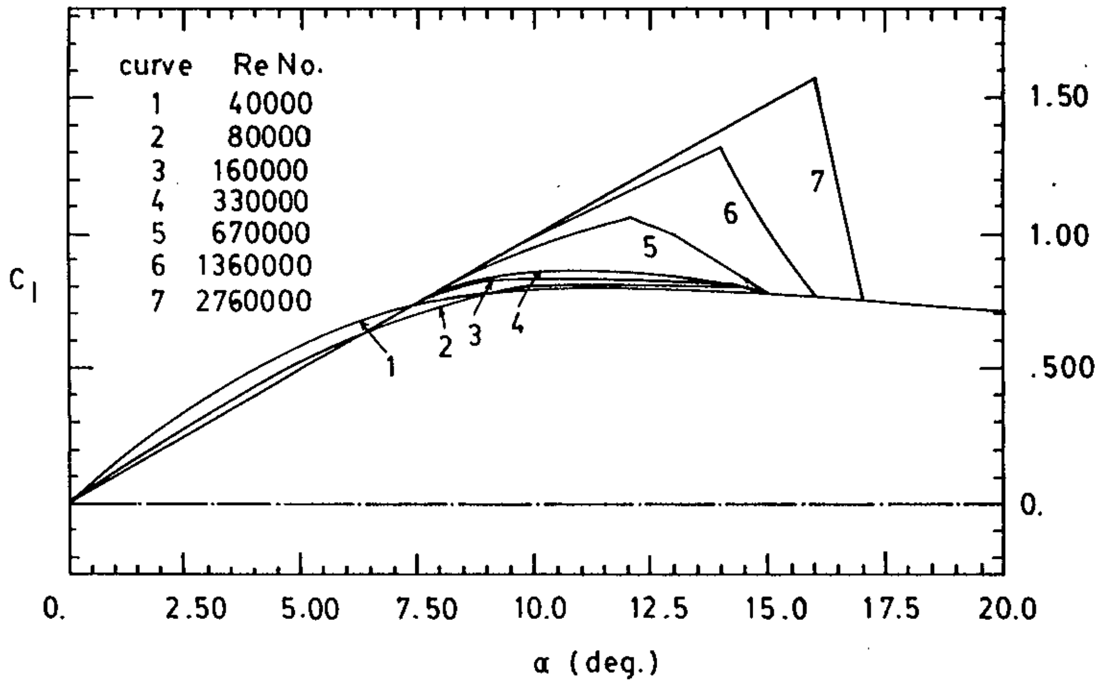

Figure E.1: Variation of lift coefficient with angle of attack at various Reynolds number for the airfoil NACA 0012.

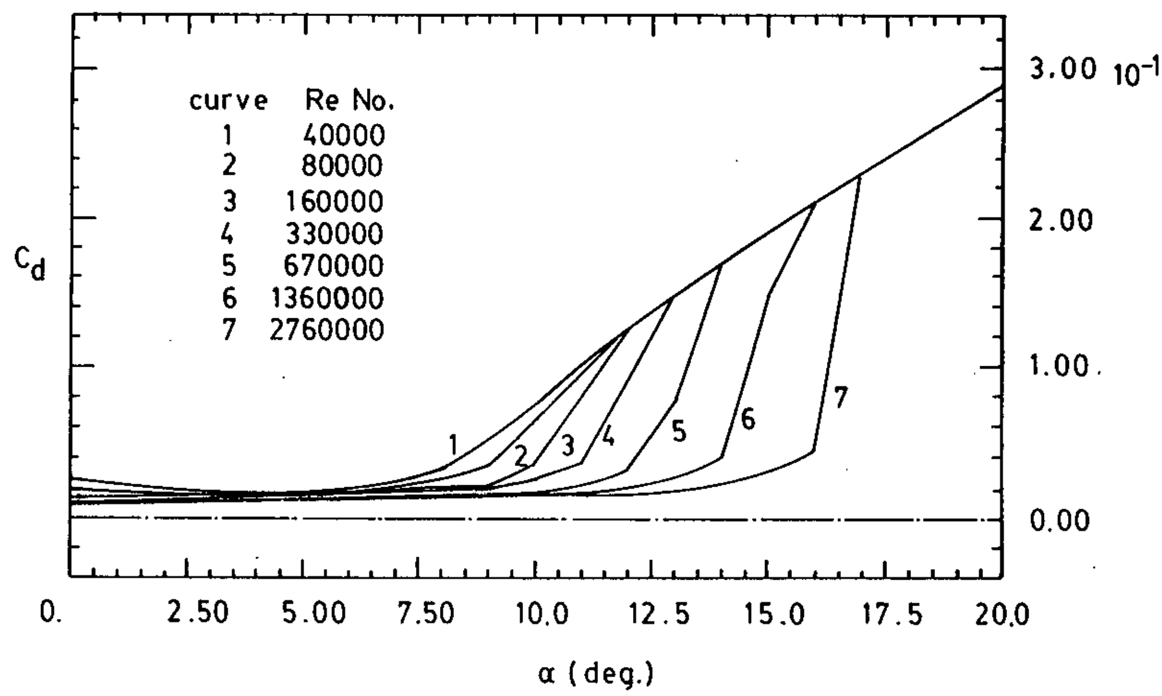

Figure E.2: Variation of drag coefficient with angle of attack at various Reynolds number for the airfoil NACA 0012.

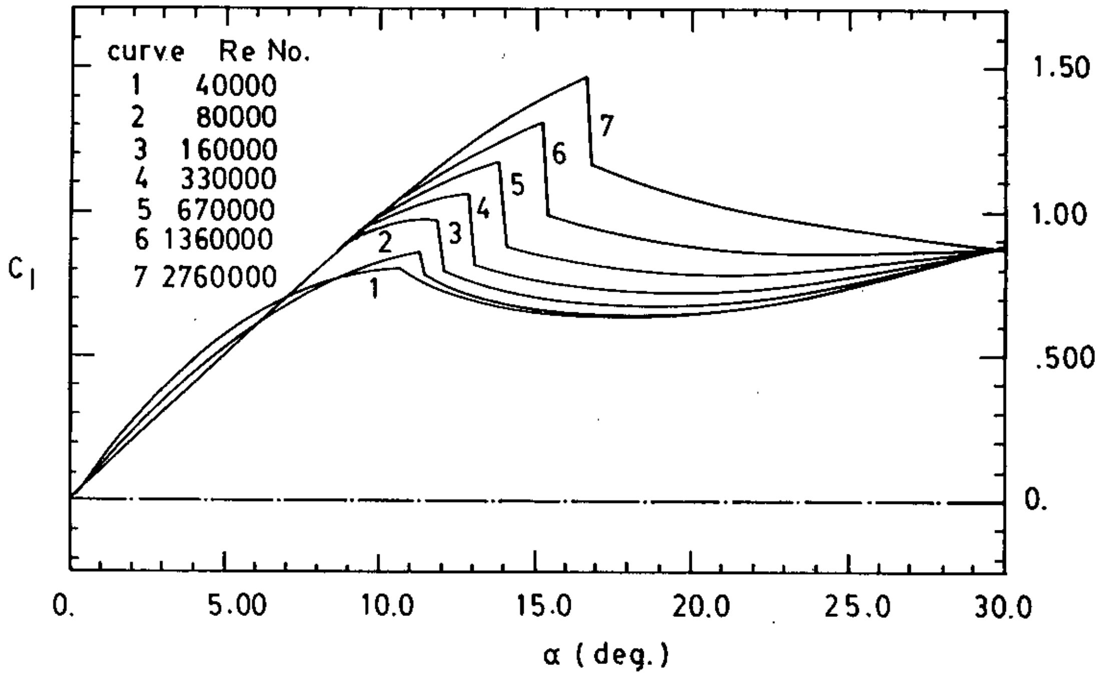

Figure E.5: Variation of lift coefficient withe angle of attack at various Reynolds number for the airfoil NACA 0015.

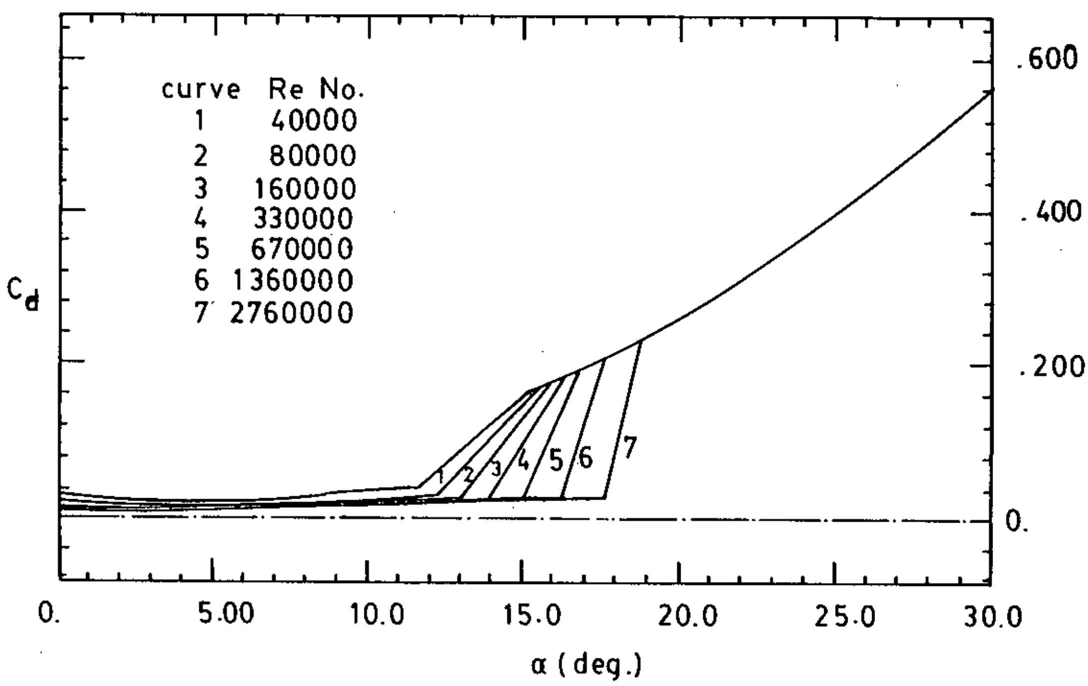

Figure E.6: Variation of drag coefficient with angle of attack at a Reynolds number for the airfoil NACA 0015.

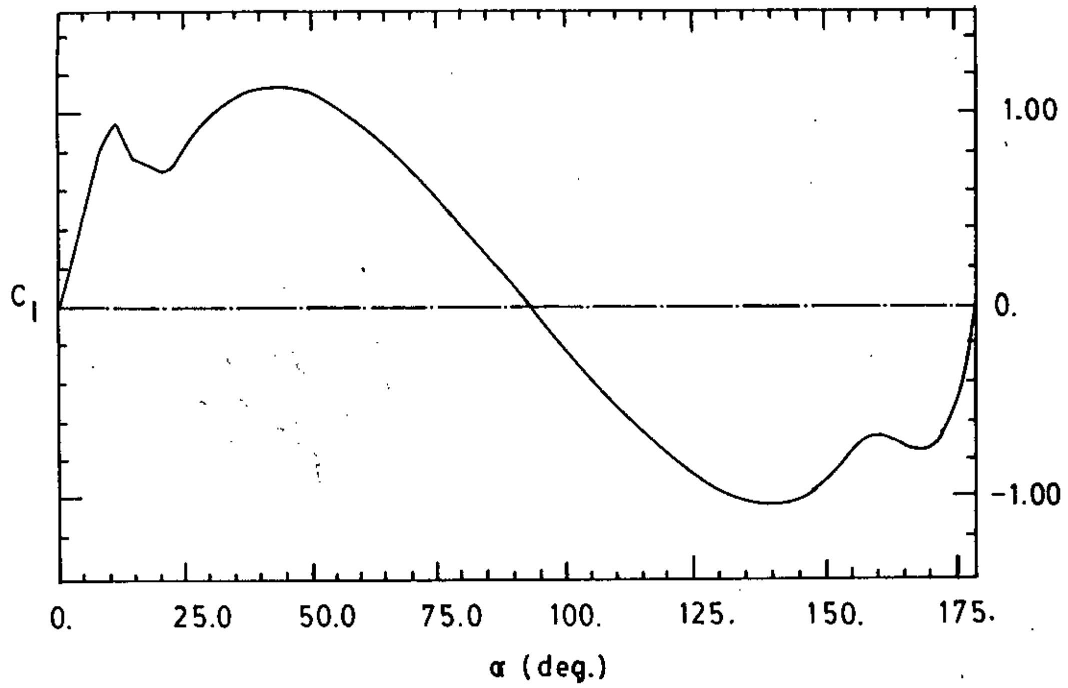

Figure E.3: Variation of lift coefficient with angle of attack at a fixed Reynolds number of 500000 for the airfoil NACA 0012.

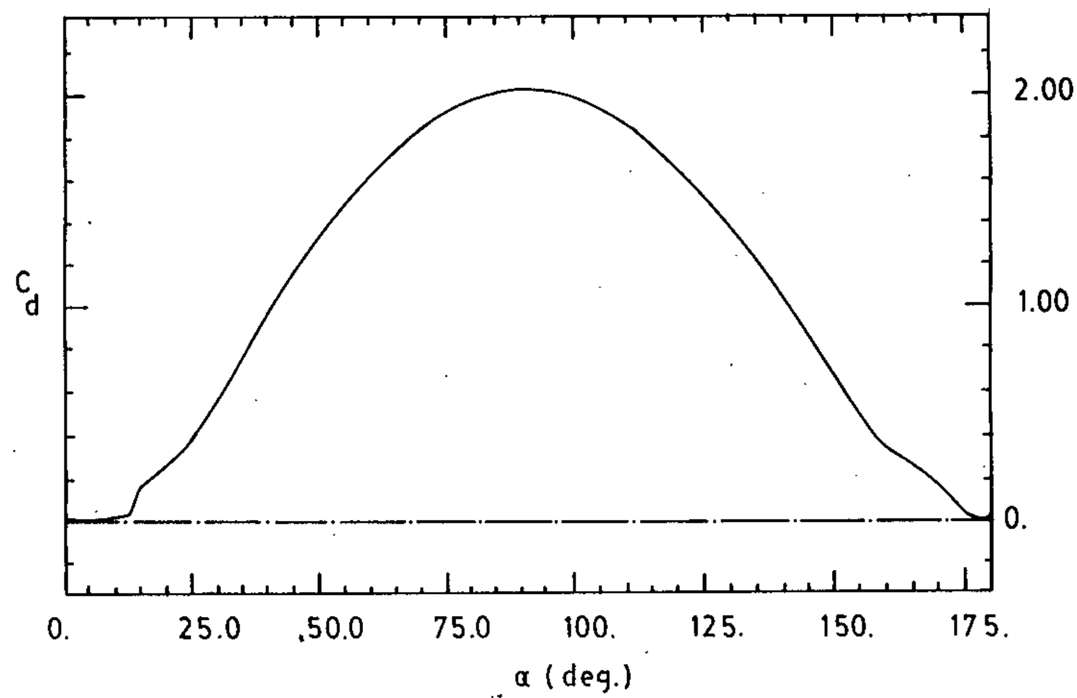

Figure E.4: Variation of darg coefficient with angle of attack at a fixed Reynolds number of 500000 for the airfoil NACA 0012.

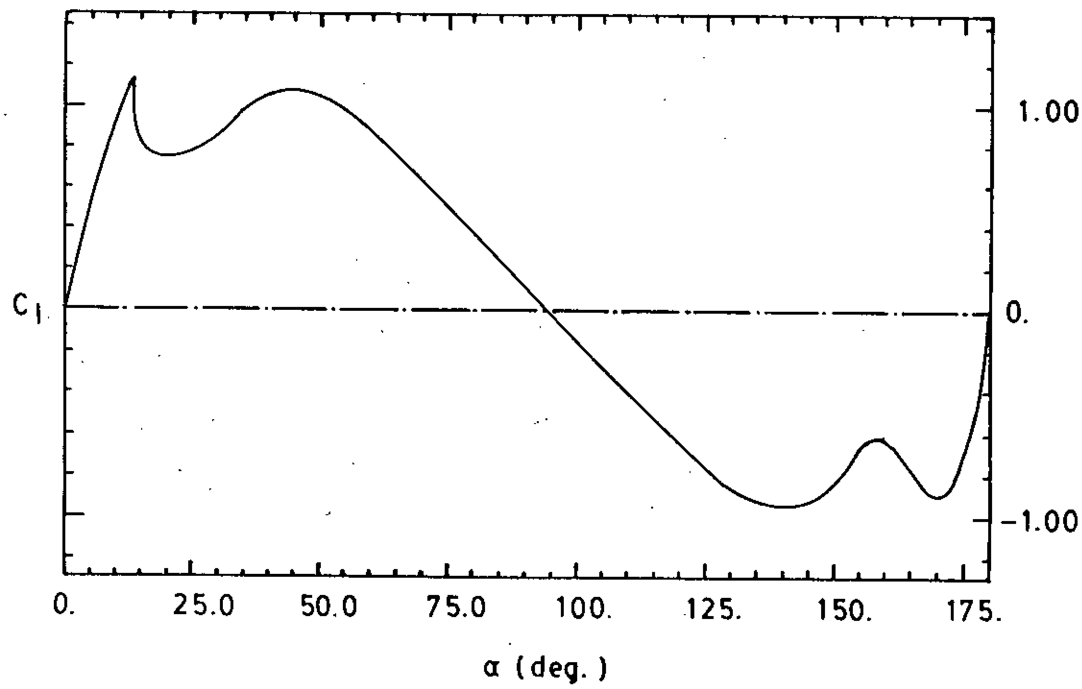

Figure E.7: Variation of lift coefficient with angle of attack at a fixed Reynolds number of 500000 for the airfoil NACA 0015.

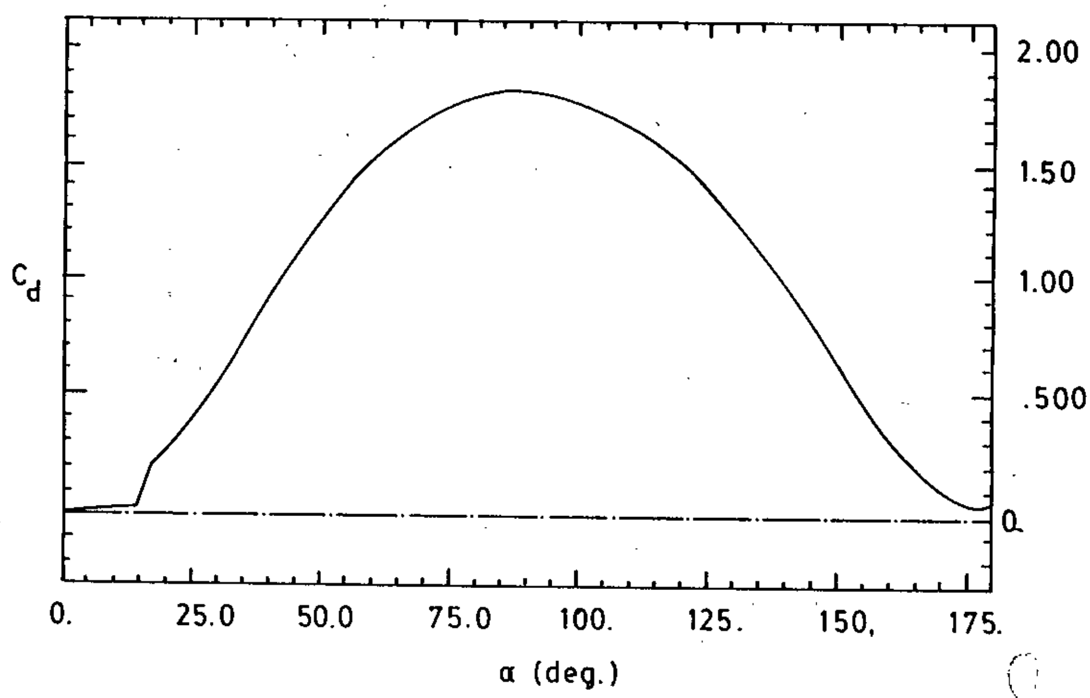

Figure E.8: Variation of drag coefficient with angle of attack at a fixed Reynolds number of 500000 for the airfoil NACA 0015.